ULTRAHIGH AND MICROWAVE FREQUENCY NANOMECHANICAL SYSTEMS

Thesis by

Xue Ming Henry Huang

In Partial Fulfillment of the Requirements

for the Degree of

Doctor of Philosophy

CALIFORNIA INSTITUTE OF TECHNOLOGY

Pasadena, California

2004

(Defended December 4, 2003)

ACKNOWLEDGEMENTS

First of all, I'd like to thank my advisor, Prof. Michael Roukes, who has always been a strong support through all these years of my graduate career, and beyond.

During my stay at Condensed Matter Physics at Caltech, I have been privileged to work with, and learn from, other members of the group. Special thanks goes to Kamil Ekinci, Darrell Harrington and Peter Burke, who have guided me into territories that used to be new to myself. I have collaborated on various projects with Jack Yang, Hong Tang, Ali Husain, Jim Hone, Henk Postma, Tylor Drake, Mladen Barbic, Keith Schwab, Deborah Santamore, Meher Prakash, Philip Feng, Inna Kozinsky, Steve Stryker, Nils Asplund, and many others, whose help has been invaluable for making my graduate research productive.

I'd also like to thank our external collaborators, Prof. Chris Zorman and Prof. Mehran Mehregany at Case Western Reserve University and Dr. Bernie Yurke at Bell-Labs, whose contributions have been crucial in making this work possible.

I'm greatly indebted to Prof. Mike Cross, Prof. Hideo Mabuchi and Prof. Rob Phillips for their serving on my defense committee, and Prof. Kip Thorne for providing guidance on QND measurements.

Administrative assistance from Exie Marie Leagons has also been extremely important for my achievements.

My graduate research has been funded by generous research grants from DARPA MTO and NSF.

Last but not least, my family members have always been with me through the ups and downs. My progress would never have been possible without their dedication.

Dedicated to

My Beloved Wife and Son

ABSTRACT

Nanodevices that operate with fundamental frequencies in the previously inaccessible microwave range (greater than 1 gigahertz) have been constructed. Two advances have been crucial to breaking the 1-GHz barrier in nanoelectromechanical systems (NEMS): the use of 3C- silicon carbide epilayers, and the development of balanced, high frequency displacement transducers. This achievement represents a significant advance in the quest for extremely high frequency nanoelectromechanical systems.

However, silicon carbide nanomechanical resonators with fundamental frequencies in the ultrahigh frequency and microwave range have exhibited deteriorating quality factors compared to devices at lower frequencies, which could significantly restrict the application of this developing technology. Our experiments have established a strong correlation between silicon carbide surface roughness and deteriorating quality factor. Also, dissipation in such devices increases as the aspect ratio of the doubly clamped beams is reduced. Based on such observations, we have then demonstrated that the SiC free-free beam nanomechanical resonators offer significant improvement in quality factor compared to doubly clamped beam design operating at similar frequencies.

Apart from 3C-SiC epilayers on silicon, polished 6H-SiC bulk material based NEMS are also made possible by our invention. A tilted Electron Cyclotron Resonance (ECR) etching technique has been developed to fabricate suspended nanomechanical structures from bulk 6H-SiC wafers. A suspended nanoscale, doubly clamped beam resonator has been made as an initial demonstration of this new fabrication method. Fundamental flexural mode mechanical resonance is detected at 171.2 MHz, with a quality factor of about 3000. The ability to fabricate 3-D suspended nanostructures from 6H-SiC is an important breakthrough

in NEMS not only because it enables electronic integration, but also because it provides a unique platform for exploring the effects of crystal and surface quality on resonator performance at microwave frequencies.

Magnetomotive transduction has been used extensively in the above achievements, where eddy current damping is usually negligible. However, it was realized that such damping phenomena may turn out to be crucial for doubly clamped beam nanotube mechanical resonators. This concept has been experimentally demonstrated. Silicon carbide material is used to create a *dummy nanotube*, and in turn being used to investigate the role of eddy current damping phenomena in the context of studying nanotube mechanical motion.

Another nanotube-based novel device structure, using a nanotube carrying a single domain nanomagnet paddle, forming a torsional mechanical resonator, has been designed and analyzed. This device design appears capable of force sensing in zeptoNewton/$Hz^{1/2}$ range at room temperature.

As we cool down GHz nanomechanical resonators to low temperatures, the devices approach their quantum regime of operation. A structure designed to enable observation of quantum jumps in nanomechanical devices is described. A prototype device demonstrating a frequency shift transduction scheme is fabricated and tested in the classical domain. The coupling mechanism involved is analogous to Kerr nonlinearity in quantum optics. This nanomechanical approach should allow quantum nondemolition (QND) measurements if the experimental technique is extended into the quantum regime. Based on quantum simulations and experimental analysis, we argue that single quanta sensitivity can be achieved in next-generation devices of this kind.

TABLE OF CONTENTS

OVERVIEW

Chapter 0

The Room at the Bottom

0.1 Motivations: From Nano to Quantum in Mechanics

The concept of *Nanotechnology*, namely, the ability to mass produce atomic-scale machines, was first publicly envisioned by Richard Feynman here in Pasadena, at a lecture more than 40 years ago. This famous talk[1] entitled *Plenty of room at the bottom*, given by Dr. Feynman in the 1959 APS meeting, has inspired generations of scientists and engineers to study the tiny machines at the nanometer scale[2]. The research work that culminates into this thesis is one more small piece of advancement added to this long-lasting pursuit and adventure.

Part of the intrigue of nanoscience is its promise for new devices offering functionality attainable from neither their macro- nor micro- scale counterparts[2]. This is especially true with small mechanical systems — inventions from previous centuries, ranging from clocks to computing machines, have largely been abandoned now that microelectronics can provide replacements that are cheap and robust. In fact, the electronic paradigm has become so firmly rooted in our collective psyche that it is now

difficult to fathom computation based upon anything other than the shuttling of minute packets of charge within microchip circuitry. Yet the first computers envisaged by Babbage in the early 1800's were indeed mechanical[3]. With the advent of ultrafast micro- and nanoelectromechanical systems (MEMS/NEMS), a complete re-evaluation of existing biases is now in order[4].

NEMS offers promise for a variety of novel applications. Sensitive mechanical charge detectors have recently been demonstrated[5], and mechanical devices for high frequency signal processing are engendering new, simplified configurations for communications systems[6]. Prospects for biological imaging based upon single-spin magnetic resonance spectroscopy now appear feasible via mechanical detectors[7]. And entirely new approaches to quantum measurement should be realizable with high-frequency nanomechanical systems cooled to low temperatures[8-11]. These are but a few of the potentialities of NEMS.

0.2 History of the Project and Us

A major thrust of research efforts in our group has been to develop nanoscale mechanical resonators for potential applications in highly integrated communications equipment. This has been supported by major DARPA grants for many years.

Since our resonator devices are extremely small, they are quite susceptible to perturbations from the environment. This has been something that needs to be overcome for making useful oscillators and transceivers. However, the same characteristics have made such devices great sensors for the events happening in its surroundings.

When I first came to this group, I started with one of these ultrasensitive sensor application projects, with Dr. Kamil Ekinci. The aim was to measure miniscule amount of mass added to the nanomechanical resonator surface, by watching the frequency shift of the device. Kamil designed and built a UHV cryostat for such purpose. I assisted in making the samples for the initial experiments. Later, after Kamil moved on to his professorship at Boston University, Jack Yang and Dr. Carlo Callegari made further efforts to optimize this measurement system, and have recently demonstrated mass sensitivity on the order of 10 zg.

A core effort of the DARPA-funded research program is to boost up the resonance frequency of our resonators, necessitated by the target applications in communications. The demonstration of the first microwave frequency nanomechanical resonators has been the most important engineering achievement during my graduate research. This success has relied on the use of silicon carbide material, and the development of a novel detection technique. The silicon carbide material (both 3C-SiC epi-layer on silicon and the 6H-SiC bulk substrate) was provided by our collaborators, Prof. Chris Zorman and Prof. Mehran Mehregany at Case Western Reserve University. This collaboration has turned out to be quite a success. We not only crossed the GHz barrier, but also got a simple and high yield process, which can provide test devices for various other experiments in the lab, such as those devices used for zeptogram mass sensing. Along the way, significant effort was spent in studying the properties of silicon carbide based resonators, from which we have obtained a lot of insights about dissipation mechanisms in nanomechanical devices.

Apart from its engineering importance, the GHz resonator also carries significant scientific interest as a test object to study quantum mechanics on mechanical entities. When such GHz resonator is cooled down to 50 mK, the thermomechanical noise floor matches the predicted Fock state level spacing under simple harmonic oscillator approximation. Namely, microwave nanoscale resonators may give us unique opportunities to access the quantum regime of device operation in nanomechanics.

For the purpose of doing quantum measurement in mechanics, Dr. Bernie Yurke has proposed, about ten years ago, a special mechanical structure that is compatible with performing quantum nondemolition (QND) measurement in mechanics. Due to technical difficulties, the scheme has been purely a theoretical toy until now. Utilizing the new developments in experimental capabilities, we have been able to build some prototype devices to study the proposed transduction scheme experimentally. All experiments performed on these prototype devices are in the classical regime. However, important insights can be achieved as a preparation for future experiments in the quantum regime.

For achieving microwave frequency while maintaining device responsivity, nanoscale feature size is a crucial parameter. Apart from what we can do with e-beam writing, self-assembled nanotubes and nanowires are clear alternatives for achieving ultra-nano sizes, such as the diameter of a single walled nanotube (SWNT), which is not really achievable by state-of-the-art e-beam lithography. The excellent properties of nanotube and nanowires have been attracting a lot of attention in the nanoscience community.

I have been involved in the nanotube/nanowire collaboration led by Dr. Jim Hone, who has now moved to Mechanical Engineering at Columbia University. The workgroup

did successfully measure a Pt-nanowire based VHF resonator. But in general, the device yield is very low. Successful operation of a single-walled nanotube (SWNT) mechanical resonator is still a project in progress. Also, we have found that eddy current damping would degrade quality of the resonance if we were to use magnetomotive detection scheme (which has been used so successfully for our top-down NEMS devices) without special precautions.

At the ASME meeting (June 2003) in Scottsdale, AZ, a talk by John Cummings about their work on multi-walled nanotube (MWNT) based actuators has led me to another possible direction based on nanotube devices. The idea is that the torsional spring constant of nanotubes is very low, and this may allow ultrahigh force sensitivity, similar to those low spring constant cantilevers that Dan Rugar's group used for sub-attonewton force sensing. Numerical analysis has shown that it's possible to have a SWNT-based device that supports $\mathrm{zN}/\sqrt{\mathrm{Hz}}$ regime effective force sensitivity. Experimental attempts are also in progress, but not included in this thesis, since the experimental part has been quite incomplete so far, even though significant progress has been made. Rather, the design and analysis of such devices is written up. It's clear that this should be a very promising direction to go for applications requiring ultrahigh force sensitivity, such as for magnetic resonance force microscopy (MRFM).

When I entered this group at Caltech about four years ago, we had about fifteen people, now the size of the group has more than doubled, and is still growing. There is an even more dramatic increase in research grants over the four-year span. The boost in laboratory capabilities has been obviously seen. Such improved facilities empower us for

the next generation of achievements, putting us into a benign cycle for a brighter future, and for having more fun with these tiny machines.

0.3 Our Approach and Achievements

Nanoelectromechanical Systems (NEMS) devices can be made by both top-down methods through e-beam lithography, and bottom-up strategies starting from self-assembled nanostructures, then connecting them to the outside world. As nanoscale size is reached, the prospects for the nanostructure to enter their quantum regime of operation are studied.

Part I of the thesis, Top-down NEMS: Silicon Carbide, is mainly about the design, fabrication and testing of silicon carbide NEMS resonator devices. Chapter 1 describes the construction of nanodevices that operate with fundamental frequencies in the previously inaccessible microwave range (greater than 1 gigahertz). Two advances have been crucial to breaking the 1-GHz barrier in NEMS: the use of silicon carbide epilayers, and the development of balanced, high frequency displacement transducers. This achievement represents a significant advance in the quest for extremely high-frequency nanoelectromechanical systems. However, silicon carbide nanomechanical resonators with fundamental frequencies in the UHF/microwave range have exhibited deteriorating quality factors compared to devices at lower frequencies, which could significantly restrict the application of this developing technology. Chapter 2 summarizes our initial attempt to address this important problem, as well as our efforts to improve the measurement techniques at these frequencies. Our experiments have established a strong correlation between silicon carbide surface roughness and deteriorating quality factor.

Also, dissipation in such devices increases as the aspect ratio of the doubly clamped beams is reduced. Thus clamping loss may be important in this regime of device operation. Based on such observations, we have then demonstrated that the SiC free-free beam nanomechanical resonators offer significant improvement in quality factor compared to doubly clamped beam design operating at similar frequencies. Apart from 3C-SiC epilayers on silicon, polished 6H-SiC bulk material based NEMS are also made possible by our invention. This work is presented in Chapter 3.

Part II of the thesis, Bottom-Up NEMS: Nanotubes, is about our efforts towards studying nanotube mechanical motion. For doubly clamped beam geometry, if we use magnetomotive transduction scheme (which has been quite successful in studying top-down NEMS resonators), it was noted that eddy current damping is usually negligible. However, it was realized that such damping phenomena may turn out to be crucial for nanotube doubly clamped beam resonators. The experimental demonstration of this concept is presented in Chapter 4. Silicon carbide material is used to create a *dummy nanotube* (experimentally simulating the key characteristics that nanotubes possess), and in turn being used to investigate the role of eddy current damping phenomena in the context of studying nanotube mechanical motion. In Chapter 5, the design and analysis of another novel bottom-up NEMS device structure is addressed, namely, a nanotube based torsional resonator. This device has a nanotube carrying a single domain nanomagnet paddle, to form a torsional resonator. It is found that such a device has the potential to attain force measurement sensitivity into the $zN/\sqrt{Hz}$ regime. This could be extremely useful for magnetic resonance force microscopy (MRFM) applications.

Part III of the thesis, Quantum Electro Mechanics, is about our pursuit for accessing the quantum regime in nanomechanics. Chapter 6 describes a nanomechanical device structure designed for quantum jump measurement in nanomechanics. A prototype device demonstrating a frequency shift transduction scheme is fabricated and tested in the classical domain. Based on quantum simulations and experimental analysis, we argue that single quanta sensitivity can be achieved in next-generation devices of this kind.

Appendix A describes a few additional projects that I was involved in, but as a secondary contributor. A.1 is our initial efforts to use silicon carbide material for NEMS. A.2 is about a novel detection scheme, utilizing balanced electronic detection, which has been proven very useful. The above two advances have been crucial for our achievement of microwave nanomechanical resonator described in the first part of the thesis. A.3 characterizes a nanomechanical resonator hosting a 2-D Electron Gas (2DEG). A.4 reports the fabrication and transduction of a platinum nanowire NEMS resonator device, the first of its kind. A.5 represents an important application of our NEMS devices for the purpose of ultrasensitive nanoelectromechanical mass detection.

Appendix B is a reprint of Caltech Media Relations press release, after the publication of Chapter 1 of this thesis in *Nature*.

Appendix C gives a brief overview of the major equipment that has been used extensively for my thesis research.

Finally, publications associated with this thesis are listed, including submitted papers and preprints about to be submitted.

0.4 Future Directions

It is still an open project to make and test mechanical resonators in the deep-nano regime with feature size of few nanometers. These can be fabricated by either top-down e-beam lithography with state-of-the-art facilities, or bottom-up schemes, such as nano-imprinting[12] and self-assembled synthesis[13-15]. At such size scale, we'll be able to make microwave mechanical resonators with lower spring constants, thus achieving greater responsivity. Such characteristics would make a spectrum of applications more plausible. Important examples of related application fields include (but are not limited to) ultrasensitive mass detection, bioNEMS sensing, MRFM and spintronics[4].

At even higher frequency, even smaller size scale, mechanical resonators may penetrate the barrier between classical and quantum regimes[4]. Ultimate realization of this will require parallel development of carefully engineered technology and deeper scientific understanding.

It is absolutely amazing to see Feynman's visionary predictions coming into reality piece by piece over the decades. In part, the efforts are for mental entertainment, as Feynman advocated in his lectures[16]. However, this emerging field is indeed finding practical applications. And these (potential) applications result in a flow of resources including manpower and research funding into what is now called *nanotechnology*.

References

1. Feynman, R. P. Plenty of room at the bottom. *http://www.its.caltech.edu/~feynman/plenty.html* (1959).

2. Roukes, M. L. Plenty of room indeed. *Sci. Am.* **285**, 48-57 (2001).

3. Swade, D. *The Difference Engine: Charles Babbage and the Quest to Build the First Computer* (Viking-Penguin, New York, 2001).

4. Roukes, M. L. Nanoelectromechanical systems face the future. *Phys. World* **14**, 25-31 (2001).

5. Cleland, A. N. & Roukes, M. L. A nanometre-scale mechanical electrometer. *Nature* **392**, 160-162 (1998).

6. Nguyen, C. T. C., Katehi, L. P. B. & Rebeiz, G. M. Micromachined devices for wireless communications. *Proc. IEEE* **86**, 1756-1768 (1998).

7. Sidles, J. A., Garbini, J. L., Bruland, K. J., Rugar, D., Zuger, O., Hoen, S. & Yannoni, C. S. Magnetic-resonance force microscopy. *Rev. Mod. Phys.* **67**, 249-265 (1995).

8. Caves, C. M., Thorne, K. S., Drever, R. W. P., Sandberg, V. D. & Zimmermann, M. On the measurement of a weak classical force coupled to a quantum-mechanical oscillator. 1. Issues of principle. *Rev. Mod. Phys.* **52**, 341-392 (1980).

9. Bocko, M. F. & Onofrio, R. On the measurement of a weak classical force coupled to a harmonic oscillator: Experimental progress. *Rev. Mod. Phys.* **68**, 755-799 (1996).

10. Armour, A. D., Blencowe, M. P. & Schwab, K. C. Entanglement and decoherence of a micromechanical resonator via coupling to a Cooper-pair box. *Phys. Rev. Lett.* **88**, 148301 (2002).

11. Cho, A. Physics - Researchers race to put the quantum into mechanics. *Science* **299**, 36-37 (2003).

12. Melosh, N. A. et al. Ultrahigh-density nanowire lattices and circuits. *Science* **300**, 112-115 (2003).

13. Iijima, S., Ichihashi, T. & Ando, Y. Pentagons, Heptagons and negative curvature in graphite microtubule growth. *Nature* **356**, 776-778 (1992).

14. Amelinckx, S. et al. A formation mechanism for catalytically grown helix-shaped graphite nanotubes. *Science* **265**, 635-639 (1994).

15. Saito, R., Dresselhaus, G. & Dresselhaus, M. S. *Physical Properties of Carbon Nanotubes* (Imperial College Press, Singapore, 2001).

16. Feynman, R. P. Tiny machines. *Feynman Lecture on Nanotechnology, video tape* (1984).

PART I

TOP-DOWN NEMS: SILICON CARBIDE

Chapter 1*

Nanodevice Motion at Microwave Frequencies

It has been almost forgotten that the first computers envisaged by Charles Babbage in the early 1800s were mechanical[1,2]and not electronic, but the development of high-frequency nanoelectromechanical systems is now promising a range of new applications[3], including sensitive mechanical charge detectors[4] and mechanical devices for high-frequency signal processing[5], biological imaging[6] and quantum measurement[7-9]. Here we describe the construction of nanodevices that will operate with fundamental frequencies in the previously inaccessible microwave range (greater than 1 gigahertz). This achievement represents a significant advance in the quest for extremely high-frequency nanoelectromechanical systems.

* Manuscript based on this chapter has been published as: Xue Ming Henry Huang, Christian A. Zorman, Mehran Mehregany & Michael L. Roukes, *Nature*, **421**, 496 (2003).

Until now, it has not been possible to create mechanical devices that operate at extremely high frequencies, owing to the dual challenge of detecting tiny displacements (on the scale of femtometres) at microwave frequencies[1,3]. The characteristic frequency of nanoelectromechanical systems (NEMS) scales upwards with decreasing size, but their displacement (when operating linearly) and their electromechanical impedance both simultaneously scale downwards.

Two advances have been crucial to breaking the 1-GHz barrier in NEMS: the use of silicon carbide epilayers[10], which are of comparable density but are significantly stiffer than the usual silicon[11,12], and which allow higher frequencies to be attained for structures of similar geometry; and the development of balanced, high-frequency displacement transducers, which enable the ubiquitous passive embedding impedances that arise from electrical connections to the macroworld to be nulled[13] (if uncontrolled, these parasitic impedances overwhelm the electromechanical impedance of interest — the 'signal' — in ultrasmall NEMS).

We used 3C-SiC films that were grown hetero-epitaxially at atmospheric pressure by chemical-vapour deposition in an induction-heated reactor on 100-mm-diameter (100) Si wafers[10]. Device nanofabrication involves both optical and electron-beam lithography to define, respectively, large-area contact pads and submicrometre-scale, thin metallic-film masks with the device geometry. Pattern transfer to the 3C-SiC layer is achieved by an electron cyclotron resonance (ECR) plasma-etch step involving an NF_3/O_2/Ar mixture. The patterned 3C-SiC beams are then suspended above the underlying silicon substrate by using an isotropic NF_3/Ar ECR etch. The metallic mask (30 nm of aluminium, followed by 5 nm of titanium), deposited by e-beam evaporation and patterned by lift-off,

remains on the beams and is used as the electrode for displacement transduction. The devices consist of two nominally identical, doubly clamped beams, roughly 1.1 μm long, 120 nm wide and 75 nm thick.

Each doubly clamped beam pair is positioned perpendicular to a strong magnetic field (3–8 tesla) *in vacuo* within a liquid-helium cryostat. Balanced magnetomotive detection is used[13]; when the driving frequency matches the fundamental frequency of the in-plane flexural mode for one of the beams, there is resonant enhancement of the induced electromotive force. This response is pre-amplified and characterized by a microwave-network analyser.

Fundamental mechanical resonances are detected at 1.014 GHz and 1.029 GHz for the two beams (Fig. 1.1). So far, quality factors attained above 1 GHz (about 500) are substantially lower than observed for NEMS in roughly the 100-MHz range (about 10^4). Having ruled out factors such as electrical damping, we are investigating whether this stems from roughness in the initial SiC epilayers, and how such sources of acoustic loss in microwave NEMS can be minimized. Nonetheless, this step into the previously inaccessible domain of microwave-frequency mechanical excitations constitutes a milestone along the path to the many new applications offered by nanomechanical systems.

Acknowledgements: *This work was generously supported by DARPA MTO/MEMS and NSF.*

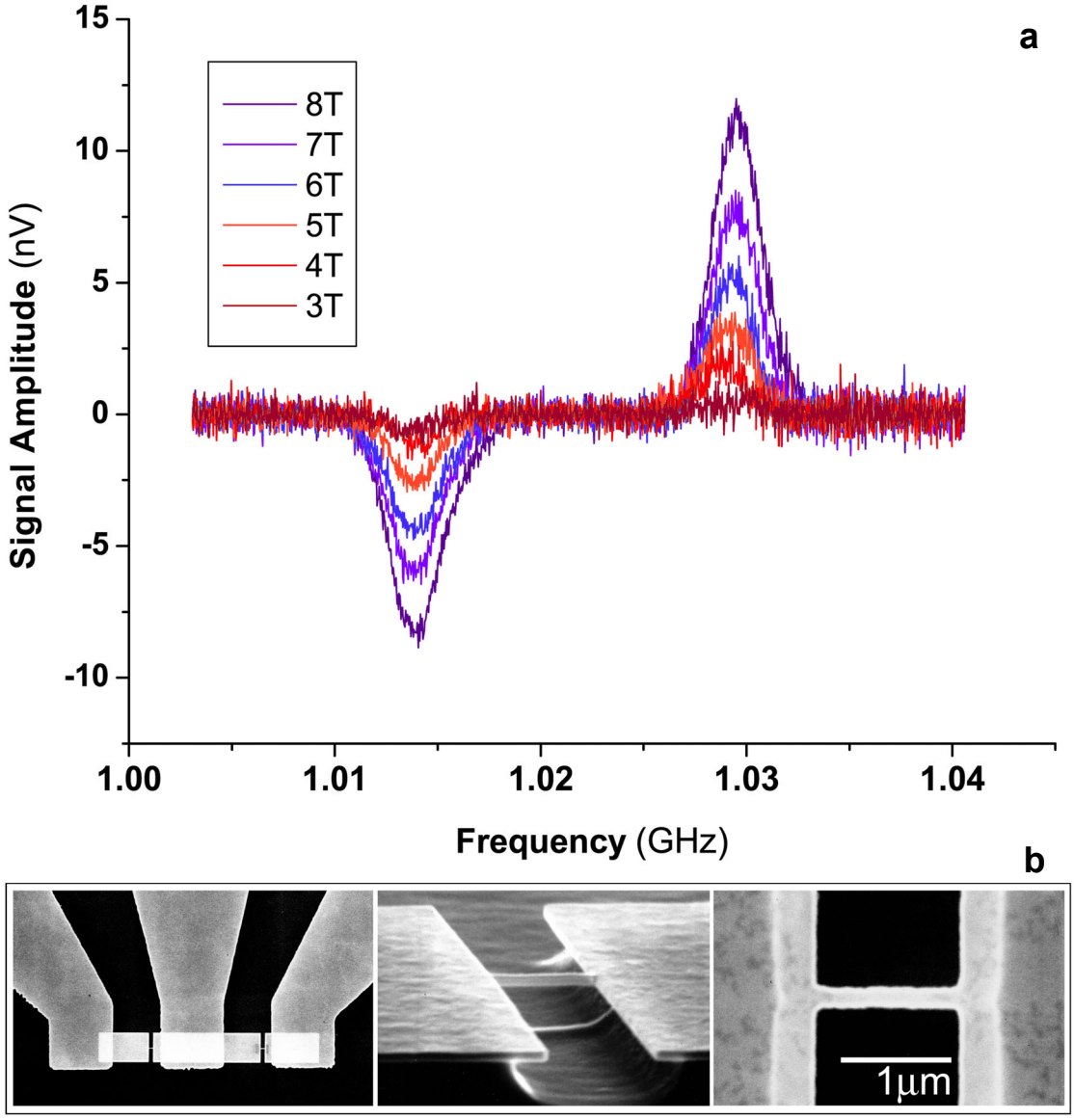

Figure 1.1 Microwave-frequency nanomechanical devices. **a,** Fundamental flexural-mode resonant mechanical response at 1.014 and 1.029 GHz, detected at about 4.2 K from a pair of doubly clamped silicon carbide beams as a function of applied magnetic field (3–8 tesla). These devices are electrically connected within a balanced magnetomotive detection scheme[13]; each distinct resonance corresponds to excitation of one of the beams within the device. **b,** Scanning electron micrographs of a similar (slightly larger) pair of devices, with magnified views of a single resonant element. Scale bar, bottom right, 1 μm.

References

1. Roukes, M. L. Plenty of room indeed. *Sci. Am.* **285**, 48-57 (2001).

2. Swade, D. *The Difference Engine: Charles Babbage and the Quest to Build the First Computer* (Viking-Penguin, New York, 2001).

3. Roukes, M. L. Nanoelectromechanical systems face the future. *Phys. World* **14**, 25-31 (2001).

4. Cleland, A. N. & Roukes, M. L. A nanometre-scale mechanical electrometer. *Nature* **392**, 160-162 (1998).

5. Nguyen, C. T.-C., Katehi, L. P. B. & Rebeiz, G. M. Micromachined devices for wireless communications. *Proc. IEEE* **86**, 1756-1768 (1998).

6. Sidles, J. A., Garbini, J. L., Bruland, K. J., Rugar, D., Zuger, O., Hoen, S. & Yannoni, C. S. Magnetic-resonance force microscopy. *Rev. Mod. Phys.* **67**, 249-265 (1995).

7. Cho, A. Researchers race to put quantum into mechanics. *Science* **299**, 36-37 (2003).

8. Armour, A. D., Blencowe, M. P. & Schwab, K. C. Entanglement and decoherence of a micromechanical resonator via coupling to a Cooper-pair box. *Phys. Rev. Lett.* **88**, 148301 (2002).

9. Bocko, M. F. & Onofrio, R. On the measurement of a weak classical force coupled to a harmonic oscillator: experimental progress. *Rev. Mod. Phys.* **68**, 755-799 (1996).

10. Yang, Y. T., Ekinci, K. L., Huang, X. M. H., Schiavone, L. M., Roukes, M. L., Zorman, C. A. & Mehregany, M. Monocrystalline silicon carbide nanoelectromechanical systems. *Appl. Phys. Lett.* **78**, 162-164 (2001).

11. Carr, D. W., Evoy, S., Sekaric, L., Craighead, H.G. & Parpia, J.M. Measurement of mechanical resonance and losses in nanometer scale silicon wires. *Appl. Phys. Lett.* **75**, 920-922 (1999).

12. Clark, J. R., Hsu, W.-T. & Nguyen, C. T.-C. High-Q VHF micromechanical contour-mode disk resonators. in *Technical Digest, IEEE Int. Electron Devices Meeting, San Francisco, California, 11-13 December 2000*, (ISBN: 0780364384), 493-496 (2001).

13. Ekinci, K. L., Yang, Y. T., Huang, X. M. H. & Roukes, M. L. Balanced electronic detection of displacement in nanoelectromechanical systems. *Appl. Phys. Lett.* **81**, 2253-2255 (2002).

Chapter 2*

Mechanical Resonance Measurement and Quality Factor Optimization in Silicon Carbide Nanomechanical Resonators

Nanomechanical resonators with fundamental mode resonance frequencies in the very high frequency (VHF), ultrahigh frequency (UHF) and microwave L-band ranges are fabricated from monocystalline silicon carbide thin film material, and measured by magnetomotive transduction, combined with a balanced bridge readout circuit. For resonators made from the same film, we measured the frequency (i.e., geometry) dependence of the quality factor. We have seen a steady decrease of quality factor as the frequency goes up. This indicates the importance of

* These results have been presented at the Transducers'03 conference and published as two conference papers:

X. M. H. Huang, M. K. Prakash, C. A. Zorman, M. Mehregany & M. L. Roukes, "Free-free Beam Silicon Carbide Nanomechanical Resonators", Digest of Technical Papers, volume 1, Transducers'03, The 12th International Conference on Solid-State Sensors, Actuators and Microsystems, Boston, MA, USA, June 8-12, 2003 (*Late News),* ISBN: 0-7803-7732-X, pp. 342-343 (2003).

X. M. H. Huang, C. A. Zorman, M. Mehregany & M. L. Roukes, "Quality Factor Issues in Silicon Carbide Nanomechanical Resonators", Digest of Technical Papers, volume 1, Transducers'03, The 12th International Conference on Solid-State Sensors, Actuators and Microsystems, Boston, MA, June 8-12, 2003, ISBN: 0-7803-7732-X, pp. 722-725 (2003).

clamping loss in this regime. To study this source of dissipation, a free-free beam silicon carbide nanomechanical resonator has been co-fabricated on the same chip with a doubly clamped beam resonator operating at similar frequencies. Device testing has been performed to directly compare their properties. A significant improvement in quality factor is observed for the free-free beam design. In addition, from studies of resonators made from different chips with varying surface roughness, we found a strong correlation between surface roughness of the silicon carbide thin film material and the quality factor of the resonators made from it. Understanding the dissipation mechanisms, and thus improving the quality factor of these resonators, is important for implementing applications promised by these devices.

2.1 Introduction

Doubly clamped beam nanomechanical resonators with operating frequencies within the microwave L-band have recently been achieved[1], owing to both the development of better materials[2] and novel detection techniques[3]. This new breakthrough promises a broad range of applications, including next generation high resolution sensors and actuators, and high speed signal processing components[4-8]. These devices also offer the potential advantage of much greater integratability over what is currently available. However, these first microwave NEMS resonators have exhibited deteriorating quality factors as the device frequency increases. This could significantly restrict the application of this developing technology. This chapter summarizes our initial attempt to address

this important problem, as well as our efforts to improve the measurement techniques at these frequencies.

One of the possible reasons for the decrease of quality factor in these devices is the clamping loss intrinsic to the doubly clamped boundary condition[9,10]. Nguyen and collaborators have previously demonstrated the use of a free-free boundary condition to reduce this source of acoustic loss for micro-scale resonators[11,12]. Here we explore the application of the free-free beam design for nanoscale resonators, where the feature size is at least an order of magnitude smaller than similar microscale structures.

2.2 Nanofabrication

3C-SiC nanomechanical resonators were fabricated using epitaxial growth and e-beam lithography techniques detailed elsewhere[2]. Here, we discuss the recipe optimized for devices designed to operate at frequencies above 100 MHz.

Briefly, the 3C-SiC films used in this work are heteroepitaxially grown on 100-mm diameter (100) Si wafers in a rf-induction-heated, atmospheric pressure chemical vapor deposition reactor[2]. SiH_4 and C_3H_8 are used as precursors, and H_2 is used as a carrier gas. The epitaxial process is a two-step, high-temperature (1280°C) procedure, involving the carbonization of the Si surface in a C_3H_8/H_2 ambient followed by epitaxial growth using SiH_4, C_3H_8, and H_2. The epitaxial growth recipe is optimized for micron-thick films yet produces 50 nm to 250 nm thick films of sufficient surface quality for e-beam lithography.

Device fabrication utilizes a combination of optical and electron beam lithography techniques. The process begins by using standard photoresist and optical lithography to define the large-area contact pads comprising a 4 nm thick Cr adhesion layer and a 80 nm thick Au film. The substrates are then coated with a PMMA thin film, which is then patterned by electron beam lithography into a metallic lift-off mold to define the submicron mechanical components of the SiC devices. The patterned metal mask (~30 nm Al, followed by ~5 nm Ti) is transferred to the 3C-SiC layer by electron cyclotron resonance (ECR) etching using a NF_3/O_2/Ar anisotropic etch. The newly patterned 3C-SiC beams are then released by simply etching the underlying Si substrate using an isotropic NF_3/Ar ECR etch. The metal etch mask remains on the SiC beams to be used as a conducting layer for device testing.

The etch rate for silicon carbide anisotropic etch is on the order of 100 nm/min (which depends on the exact location of the sample in the plasma), while the etch rate for the metallic mask is on the order of 1 nm/min. Such contrast in etch rate enables us to use very thin layer of metals, which is important in the fabrication of ultrasmall devices.

Here, we employ 30 nm of Al, followed by 5 nm of Ti as the choice for device metallization, even though other metals such as Au and Ni are also capable of surviving the ECR etching process and can provide the electrical conductivity required by the detection scheme discussed later in this paper. The low mass density of Al helps in reducing mass loading, thus resulting in a higher frequency for the same device geometry as compared with a denser metal. The thin Ti top layer helps reduce oxidation of Al in the first ECR etching step, where oxygen is used as a gas component.

A typical suspended nanostructure is shown in the insert of Fig. 2.1. Two nearly-identical suspended beams form a device structure for testing. Typical devices are about 75 nm thick, with beam widths of 100 to 150 nm and lengths of 1.0 to 3.0 μm. A typical metallized beam has a measured resistance of about 100 Ohm at room temperature, with the resistance mismatch between the two beams in the same device to be within a few percent.

2.3 Measurement of Mechanical Resonance

Device testing is performed in ultrahigh vacuum (provided by liquid helium cooling of a sealed and evacuated dipper) and involves the use of magnetomotive transduction[13,14] in conjunction with a variation of the balancing technique[3] tailored for VHF/UHF/Microwave applications.

The schematic circuit diagram is shown in Fig. 2.1. The sample is positioned in a magnetic field with the beams perpendicular to the field lines. The potential of the center pad is initially held at virtual ground by using a 180 degree power splitter to provide out-of-phase driving of the two device branches and by making the two branches of the circuitry as close to identical as possible. The two beams are also nearly (but not exactly) identical to each other. As a result, they have slightly different resonance frequencies. When the drive frequency is swept to match the fundamental resonance frequency of one of the beams, resonant motion is induced to cut the field lines resulting in an emf voltage that can be detected. Nonidealities in the system produce a high residual background, which can be reduced using the balancing technique (Fig. 2.2). The improvement here is limited by the resistance mismatch (of a few percent) in between the two beams, which

was sufficient for this experiment. Further improvement can be made by using variable attenuators and adjustable phase shifters to further match the two branches of the driving circuit. Use of a low-noise cryogenic amplifier (Fig. 2.3) enables the detection of displacements on the order of femtometers. Resonance curves at different B fields for a typical UHF resonator pair are shown in Fig. 2.4. The peak and the dip represent the resonance of each of the two doubly clamped beams in the device structure. The observed noise temperature (referred back to the input of the amplifier) is about 7.6 K. The noise comes from a combination of amplifier noise and the Johnson noise due to beam resistance sitting at 4.2 K. The noise temperature implies that the displacement detection sensitivity on the order of $\mathrm{fm}/\sqrt{\mathrm{Hz}}$ has been achieved in our experiments. The maximum signal amplitude depends linearly on B^2, as expected. The peaks are fitted to a Lorentzian curve in order to extract the quality factor, Q. Here, we adopt the definition most popularly used in the field, namely, $Q = \omega_0 / \Delta\omega$, where ω_0 is the resonance frequency, $\Delta\omega$ is peak width in power spectrum (i.e., width at half maximum signal power, or equivalently, $1/\sqrt{2}$ maximum signal amplitude), though another convention, which uses full-width at half amplitude as peak width, also appears in the literature (such as Ref. [2]). The two definitions differ only by a numerical constant, with the Q value following the latter definition being smaller by a factor of $\sqrt{3}$.

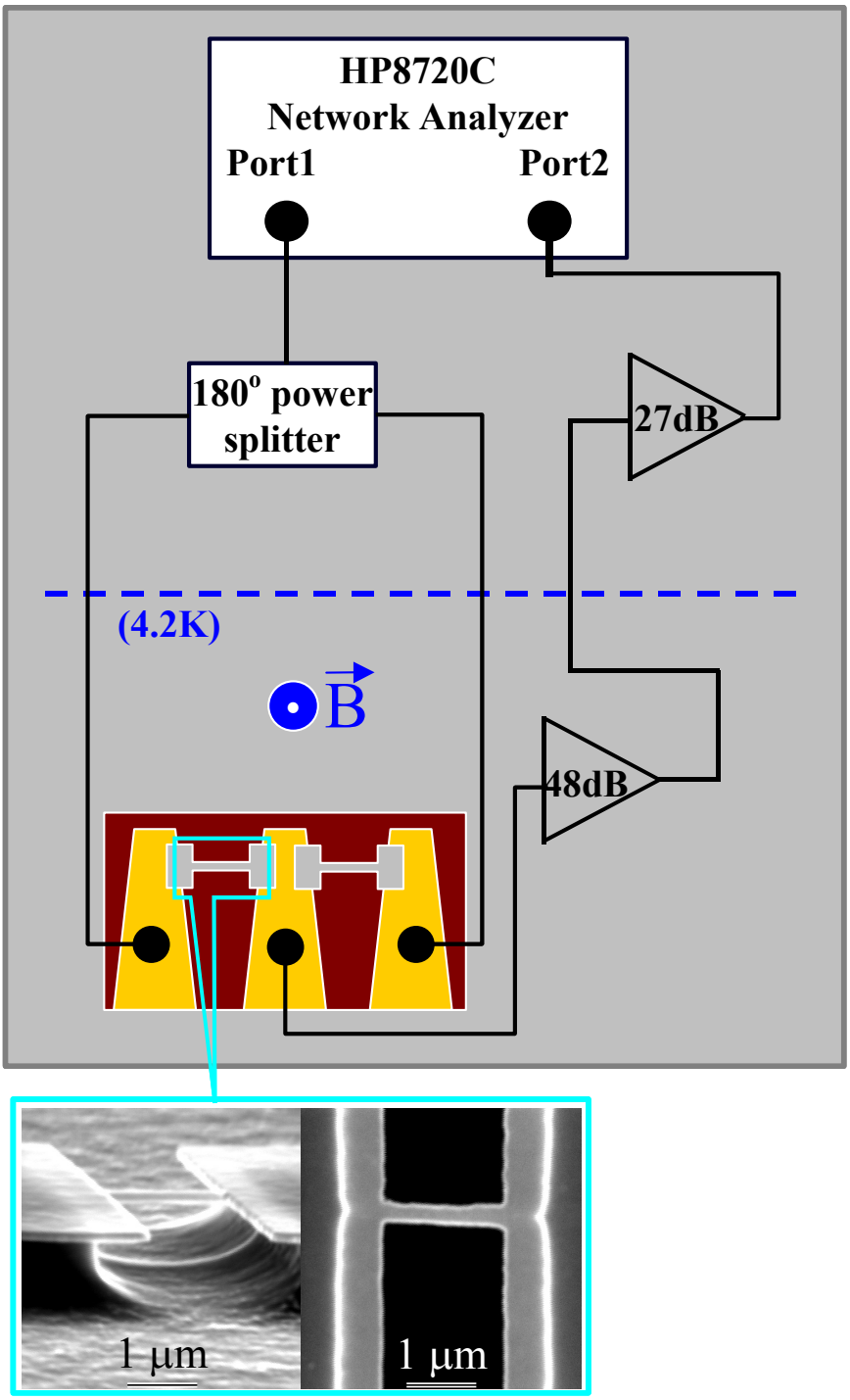

Figure 2.1 Schematic circuit diagram for balanced electronic detection. (inset) Side and top zoom-in view of one of the two doubly clamped beams in the device structure.

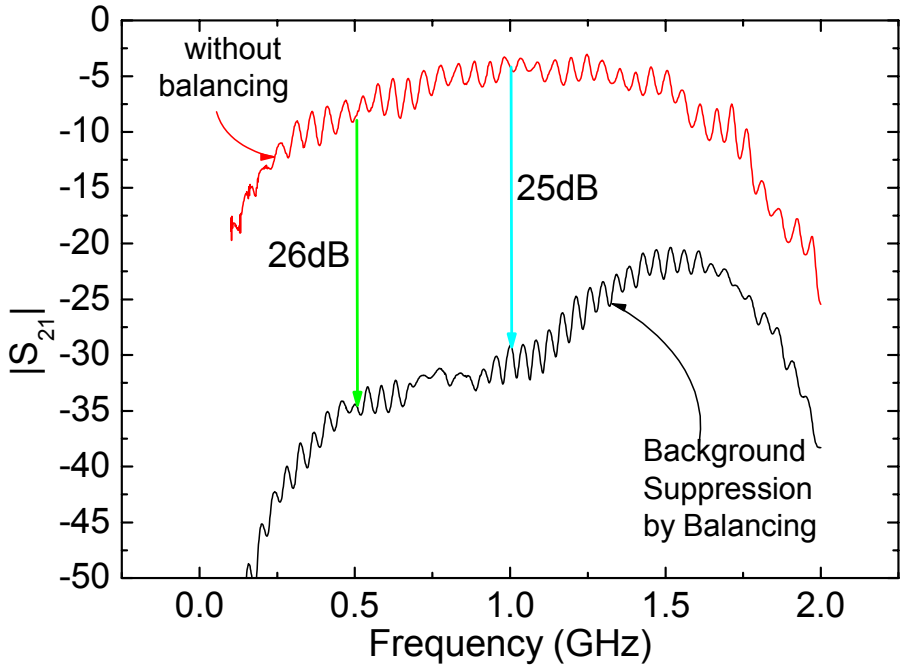

Figure 2.2 Suppression of detection background by the balancing technique.

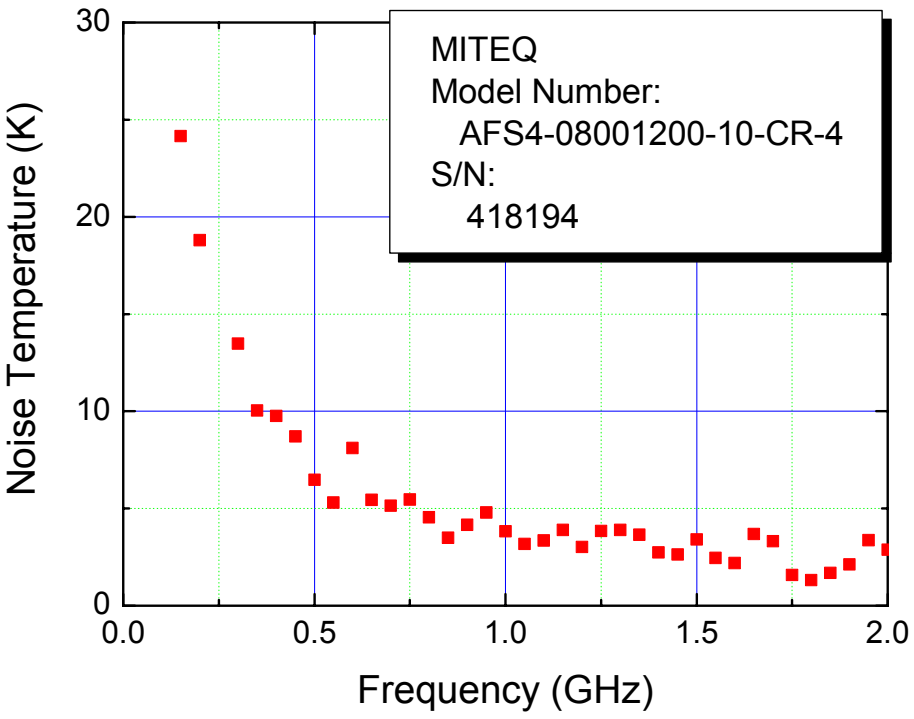

Figure 2.3 Measured noise temperature of the cryogenic-amplifier when it is immersed in liquid helium.

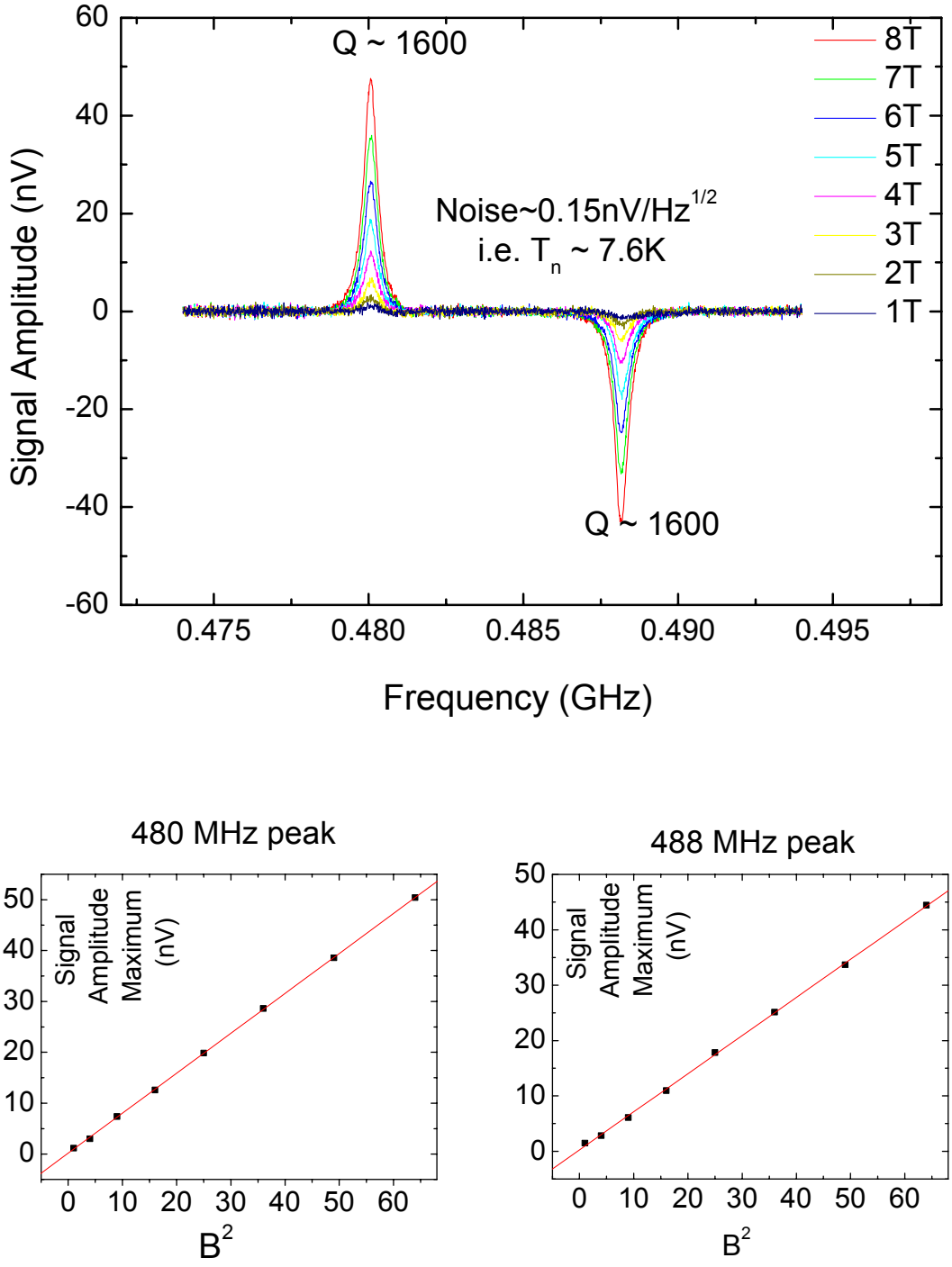

Figure 2.4 (upper) Typical UHF resonance curves at different magnetic fields measured using the circuit shown in Fig. 2.1. (lower) The two figures below show that the signal amplitude is proportional to B^2, as expected.

2.4 Clamping Loss

The frequency dependence of Q for a family of devices fabricated from the same 3C-SiC film is plotted in Fig. 2.5. The beams were identical in nearly every parameter except length, with the shortest beams (1.1 μm) yielding the highest resonant frequencies. The steady decline in Q with increasing frequency for beams made from the same film suggests that a clamping loss mechanism may influence Q at VHF/UHF/microwave frequencies.

At least two approaches (or their combination) may be used to alleviate clamping loss at such frequencies. One is to further shrink the width of the devices. For the same operating frequency, a smaller width along the direction of motion would allow larger aspect ratio to be used, thus reducing clamping loss and improving Q, according to the results shown here. The other is the application of a free-free beam design[11,12], to clamp the beams at the motional nodal points of fundamental resonance, and strategically design the support structure to minimize energy transfer from the resonance mode to the environment.

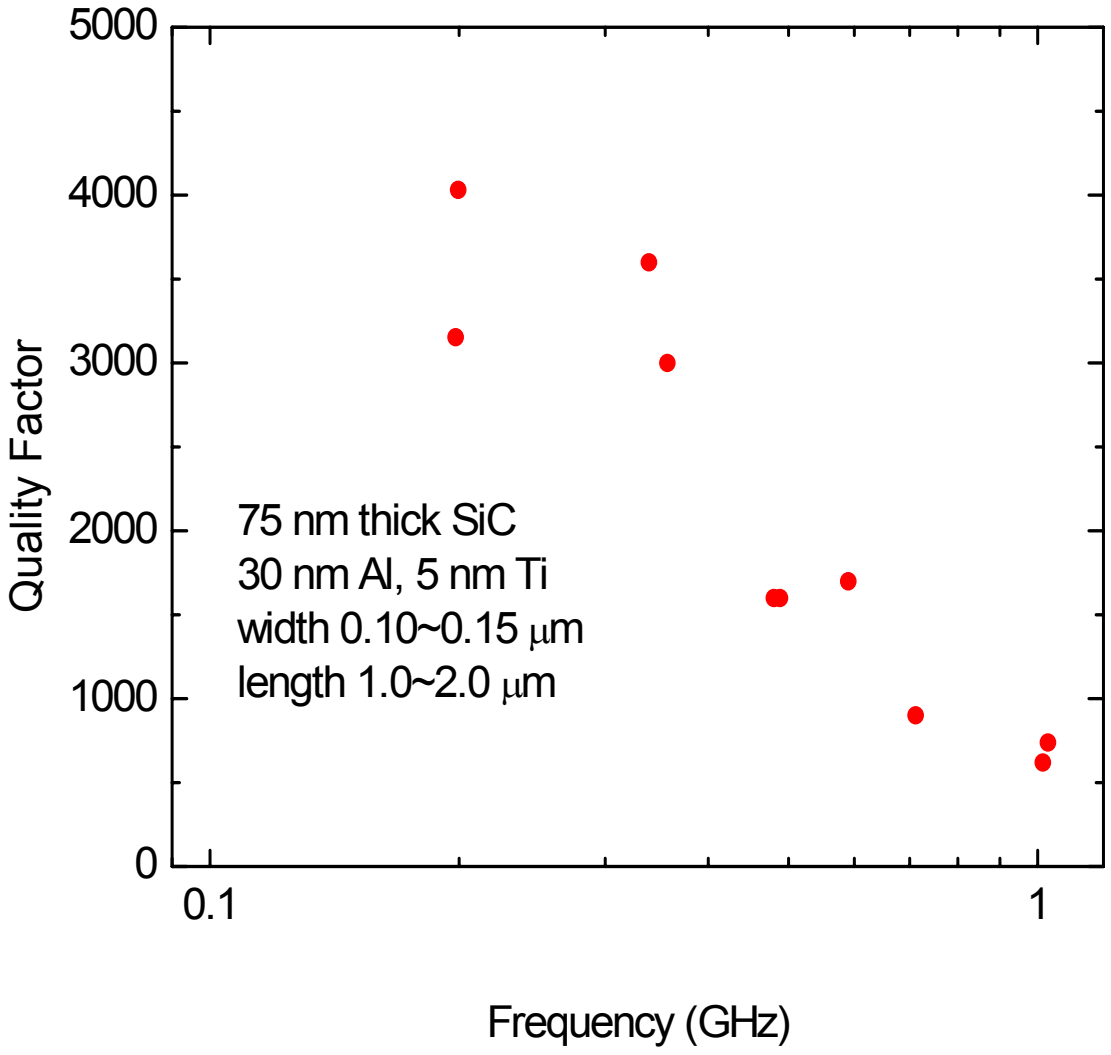

Figure 2.5 Quality factor vs. frequency plot for doubly clamped beam devices made out of the center area of Wafer B (see Fig. 2.6). These devices differ only in e-beam writing pattern geometry. The plot shows a gradual decrease in Q when the device size becomes smaller, i.e., frequency becomes higher.

2.5 Free-Free Beam Nanomechanical Resonators

Here, we focus on the latter approach. We have used the lateral free-free beam design pioneered by Dr. Clark Nguyen and his group at the University of Michigan, to try to improve the quality factor of our nanodevices. The device structures consist of doubly clamped and lateral free-free designs[12]. SEM micrographs of some typical suspended resonator structures are shown in Fig. 2.6.

The test setup is shown in Fig. 2.7. Each resonator beam pair is positioned perpendicular to a strong magnetic field (1 to 8T) in vacuum at cryogenic temperatures. An rf current is passed through the conductor. For rf frequencies away from the mechanical resonance, the induced mechanical motion is minimal and the output at the central terminal can be approximately nulled to ground potential, through proper adjustment of the variable attenuators to balance the two electrical branches in the circuit. When the driving frequency matches the resonant frequency of one of the beams, resonant motion will occur in that beam, which, in turn, induces an emf at the output terminal. After proper amplification, this emf is measured by a network analyzer.

The beam pair under test has length of ~3.0 μm, the width of resonator beams and support beams (in the free-free design) are both ~0.15 μm. In-plane resonances are observed at 170.01 MHz and 174.59 MHz, respectively, as shown in Fig. 2.8. By changing the variable attenuators and observing the amplitude change of both resonance peaks, we are able to determine that the 170.01 MHz peak is from the doubly clamped beam, while the 174.59 MHz peak is from the free-free beam resonator. Lorentzian fits to these peaks after de-embedding from the electrical background gives us quality factors for these resonators. The quality factor of the doubly clamped beam is ~ 4,500, whereby

that of the free-free beam resonator is ~11,000. The quality factor for the doubly clamped case is consistent with what we had observed with previously measured resonators of similar geometry and similar surface roughness. The free-free beam measured in this experiment has a quality factor significantly higher than the best value from its doubly clamped counterpart.

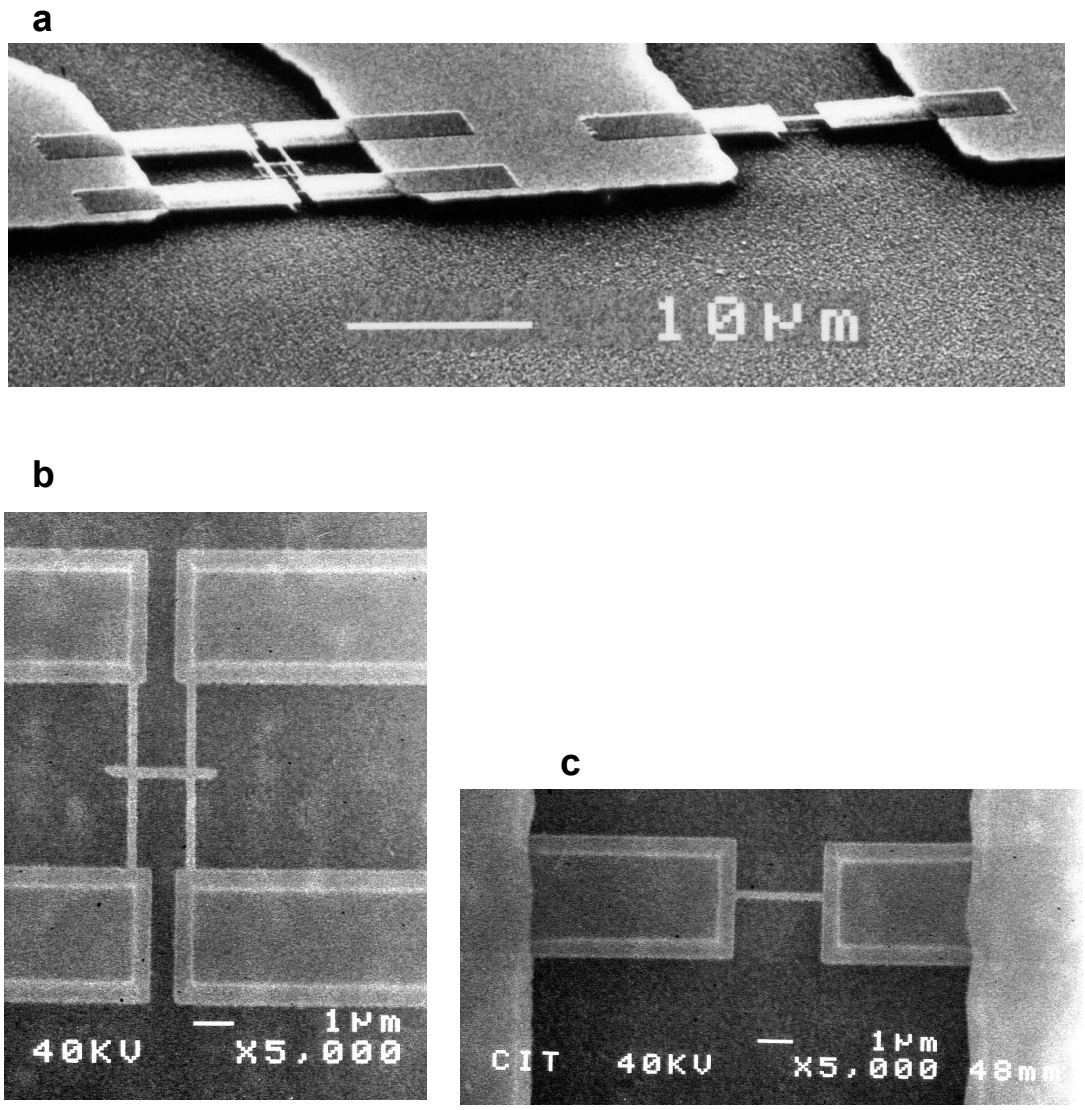

Figure 2.6 SEM micrographs of typical devices. **a,** Side view. **b,** Top-view zoom-in of a lateral free-free beam resonator. **c,** Top-view zoom-in of a doubly clamped beam resonator.

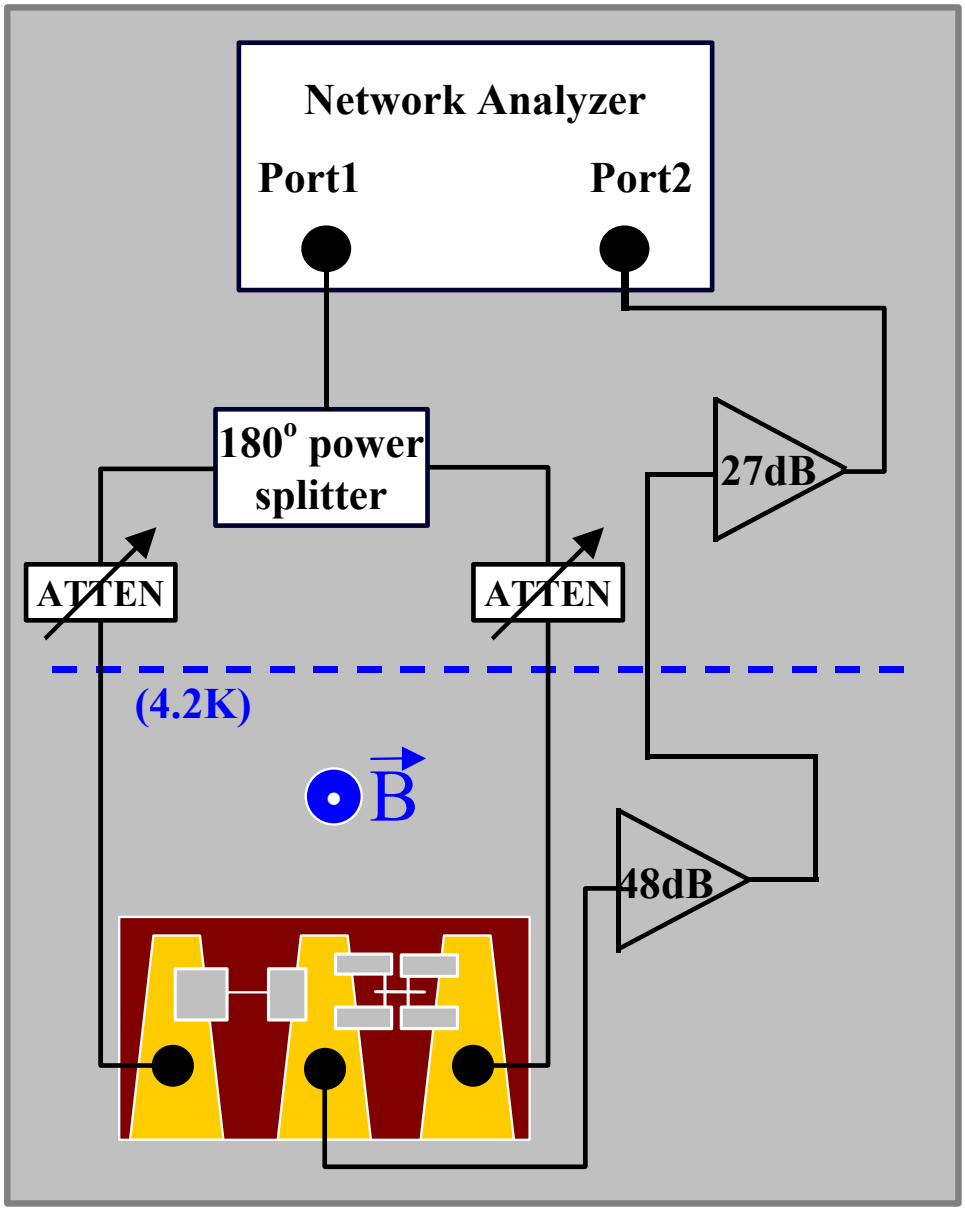

Figure 2.7 Measurement setup. A doubly clamped beam and a lateral free-free beam are fabricated within the same device structure for testing and comparison.

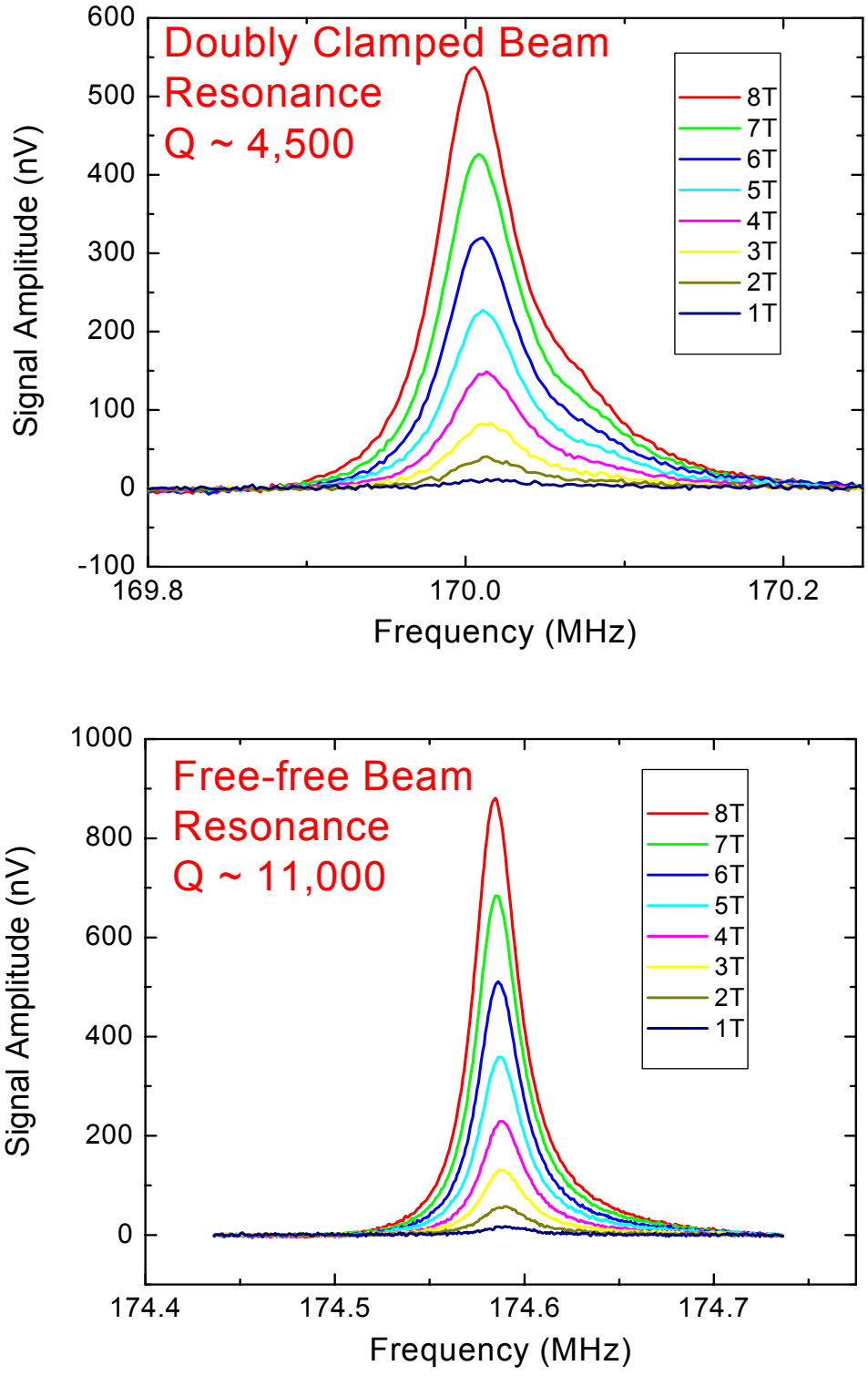

Figure 2.8 Resonance traces for different B fields. The quality factor from the free-free beam resonance is about 2.4 times that from the doubly clamped resonance.

2.6 Effects from Surface Roughness

To investigate the effect of film quality on performance, devices were fabricated from films that differed significantly in surface roughness (see Fig. 2.9). In all cases, devices operational in the UHF/microwave regime were made from films that had a low surface roughness (~ 2.1 nm). In contrast, devices made from rougher films (up to ~ 7.1 nm) were operational into the VHF range, but not higher. For our setup, failure to detect any signal indicates an upper limit in the quality factor of the non-operational structures to be well below ~100. These results suggest a strong correlation between quality factor and surface roughness.

The epitaxial growth recipe used to prepare the 3C-SiC films was initially designed for MEMS applications and thus was optimized for micron-thick films yet can produce 50 nm to 250 nm thick films of sufficient surface quality for e-beam lithography. Our results indicate that while the surfaces might be sufficient for fabrication purposes, it is critically important that the growth processes be optimized to produce ultrasmooth SiC thin films if these films are to be used for nanomechanical resonators having reasonably high Q values. The issue of surface roughness is only now coming to the forefront, since up to recently, nanomechanical beams have only been fabricated from Si wafers (bulk and SOI) and epitaxial III-V films (i.e., GaAs) that have ultrasmooth surfaces by virtue of a long history in microelectronics. And this issue will continue to be important as new materials are added to the NEMS toolbox in response to the widening array of applications. Recipes for growing ultrathin SiC films optimized for surface smoothness, and techniques for SiC thin film surface polishing are currently under development.

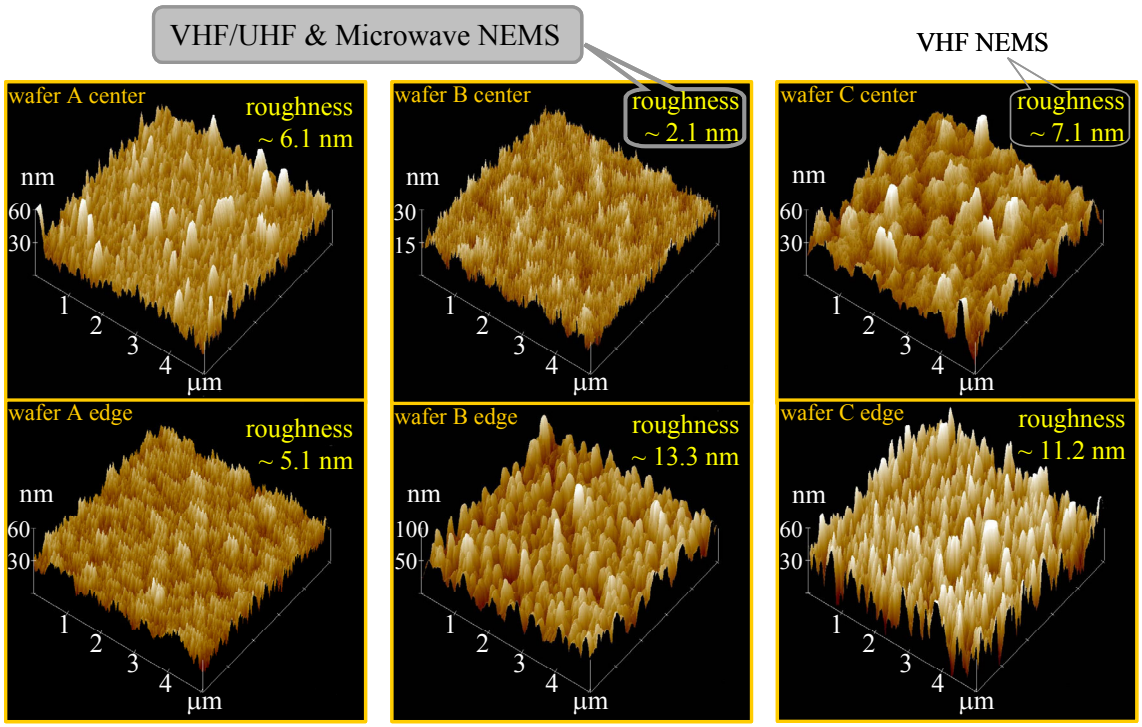

Figure 2.9 AFM images of surface morphology of three SiC films, labeled A, B & C. It is observed that all successfully measured UHF/Microwave devices are fabricated from the center area of wafer B. Center area of wafer C has produced some good devices in VHF frequency range, but fails to work in the UHF and microwave frequency range.

2.7 Conclusions

In conclusion, we have demonstrated that the resonant frequency of silicon carbide nanomechanical resonators designed to operate in the UHF to low microwave L-band range can be measured using magnetomotive transduction techniques. Dissipation in such devices increases as the aspect ratio of the doubly clamped beams is reduced. We have demonstrated the SiC free-free beam nanomechanical resonators offer significant improvement in quality factor compared to doubly clamped beam design operating at similar frequencies. A strong correlation between surface roughness and deteriorating quality factor is established from our experiments. Technological developments such as these are proven crucial for realizing high-Q nanoscale mechanical resonators. Understanding the dissipation mechanisms and achieving the ability to improve the quality factor of such resonators is crucial for future NEMS applications.

Acknowledgements: *This work was generously supported by DARPA MTO/MEMS and NSF.*

References

1. Huang, X. M. H., Zorman, C. A., Mehregany, M. & Roukes, M. L. Nanodevice motion at microwave frequencies. *Nature* **421**, 496 (2003).

2. Yang, Y. T., Ekinci, K. L., Huang, X. M. H., Schiavone, L. M., Roukes, M. L., Zorman, C. A. & Mehregany, M. Monocrystalline silicon carbide nanoelectromechanical systems. *Appl. Phys. Lett.* **78**, 162-164 (2001).

3. Ekinci, K. L., Yang, Y. T., Huang, X. M. H. & Roukes, M. L. Balanced electronic detection of displacement in nanoelectromechanical systems. *Appl. Phys. Lett.* **81**, 2253-2255 (2002).

4. Roukes, M. L. Plenty of room indeed. *Sci. Am.* **285**, 48-57 (2001).

5. Roukes, M. L. Nanoelectromechanical systems face the future. *Phys. World* **14**, 25-31 (2001).

6. Cleland, A. N. & Roukes, M. L. A nanometre-scale mechanical electrometer. *Nature* **392**, 160-162 (1998).

7. Nguyen, C. T. C., Katehi, L. P. B. & Rebeiz, G. M. Micromachined devices for wireless communications. *Proc. IEEE* **86**, 1756-1768 (1998).

8. Carr, D. W., Evoy, S., Sekaric, L., Craighead, H. G. & Parpia, J. M. Measurement of mechanical resonance and losses in nanometer scale silicon wires. *Appl. Phys. Lett.* **75**, 920-922 (1999).

9. Lifshitz, R. Phonon-mediated dissipation in micro- and nano-mechanical systems. *Physica B* **316**, 397-399 (2002).

10. Cross, M. C. & Lifshitz, R. Elastic wave transmission at an abrupt junction in a thin plate with application to heat transport and vibrations in mesoscopic systems. *Phys. Rev. B* **6408**, art. no.-085324 (2001).

11. Wang, K., Yu, Y., Wong, A. C. & Nguyen, C. T.-C. VHF free-free beam high-Q micromechanical resonators. in *Technical Digest, 12th International IEEE Micro Electro Mechanical Systems Conference, Orlando, Florida, Jan. 17-21, 1999,* (ISBN: 0780351975), 453-458 (1999).

12. Hsu, W.-T., Clark, J. R. & Nguyen, C. T.-C. Q-optimized lateral free-free beam micromechanical resonators. in *Digest of Technical Papers, Transducers'01, the 11th International Conference on Solid State Sensors & Actuators, Munich, Germany, June 10-14, 2001,* (ISBN: 3540421505), 1110-1113 (2001).

13. Cleland, A. N. & Roukes, M. L. Fabrication of high frequency nanometer scale mechanical resonators from bulk Si crystals. *Appl. Phys. Lett.* **69**, 2653-2655 (1996).

14. Cleland, A. N. & Roukes, M. L. External control of dissipation in a nanometer-scale radiofrequency mechanical resonator. *Sens. Actuator A-Phys.* **72**, 256-261 (1999).

Chapter 3*

Fabrication of Suspended Nanostructures from Bulk 6H-SiC Substrates for Nanomechanical Resonator Applications

A tilted electron cyclotron resonance (ECR) etching technique has been developed to fabricate suspended nanomechanical structures from bulk 6H-SiC wafers. The method applies an anisotropic ECR etch from three different angles relative to the wafer surface in order to pattern and release free-standing structures. A suspended nanoscale, doubly clamped beam resonator has been made as an initial demonstration of this new fabrication method. Fundamental flexural mode mechanical resonance is detected at 171.2 MHz, with a quality factor of about 3000. The availability of three-dimensional suspended nanostructures has opened up the possibility to integrate microwave-frequency nanomechanical devices with 6H-SiC based electronics, and thus significantly broaden the application scope of SiC nanomechanical systems.

* Preliminary results based on this chapter were presented at the International Conference on Silicon Carbide and Related Materials 2003 (ICSCRM 2003), Lyon, France, October 5-10, 2003.

3.1 Introduction

Miniaturized mechanical devices have been developed in parallel with the shrinkage of electronic devices from micro- down to nano- scale[1,2]. The integration of nanomechanics with nanoelectronics has promised a wide spectrum of applications for making ultrafast, high-resolution actuators and sensors, and high frequency signal processing components and systems[3,4]. Silicon Carbide (SiC)[5] is proven to be particularly well suited for nanoelectromechanical systems (NEMS) as recently shown by the successful demonstration of the first NEMS resonator with a fundamental resonant frequency greater than 1 GHz.[6] This device capitalizes on the high acoustic velocity of SiC relative to other materials by using a 3C-SiC thin film (75 nm thick) as the main structural layer[7-10]. 3C-SiC was selected over other polytypes because it can be grown on sacrificial Si substrates, thus greatly simplifying the fabrication process. However, the high defect density in 3C-SiC thin films inhibits the integration of nanomechanical components with SiC electronics. For such systems, 6H-SiC is preferred, since high-quality wafers suitable for electronics are readily available[11]. But unfortunately, sacrificial layers cannot easily be incorporated into these substrates, thus requiring alternative fabrication techniques to realize suspended mechanical structures. This chapter introduces the fabrication of 6H-SiC nanomechanical beams for NEMS applications using a method that does not depend on the removal of a buried sacrificial layer to release the suspended structures.

3.2 Tilted ECR Etch

The 6H-SiC wafer used in this study had a surface roughness of about 1 nm, as measured by AFM (Fig. 3.1). This roughness is about a factor of 2 lower than the 3C-SiC films used previously[6], and is similar to what we have achieved recently in our efforts to grow ultrasmooth 3C-SiC thin films. Since a correlation between increasing surface roughness and deteriorating quality factor has been established for nanomechanical resonators fabricated from 3C-SiC[12], the surface quality of the 6H-SiC wafer we use here is expected to contribute to the dissipation processes in a similar fashion to the best of our 3C-SiC thin films.

To fabricate the nanomechanical structures, device patterns are transferred to a thin film metallic etch mask using a combination of photo- and e-beam lithography processes. For large anchor pads, the masks consist of 4 nm of Cr followed by 80 nm of Au and are patterned photolithographically. The masking layer for the beam structures is patterned using e-beam lithography and consists of 30 nm of Al, followed by 10 nm of Ti. A highly anisotropic ECR etch process involving a mixture of Ar and NF_3 is used to pattern and release the suspended nanostructures. The chamber pressure is held at 30 mTorr, with both Ar and NF_3 flowing at a rate of 10 sccm. A DC bias of –100 V is applied to the sample stage. The etch rate for 6H-SiC is on the order of 100 nm/min, while that for the metallic mask is about 1 nm/min. To fabricate a doubly clamped beam, three etching steps are used, as shown schematically in Fig. 3.2. The first etch is performed along a direction parallel to the surface normal. This etch serves to define the general pattern of the beam and anchor pads. The second etch is performed after rotating the sample, so that the etching direction is rotated with respect to the principal axis of the

beam by 45°. The etch is performed such that at least 50% of the beam is undercut. The third etching step is performed with the etching direction at –45° and is continued until the beam is completely suspended. The three anisotropic ECR etching steps result in a suspended yet doubly clamped 6H-SiC beam with a triangular cross section. After the etch, most of the Ti layer is etched away, based on etch rate estimates. The thin aluminum layer remains on the beam after the etch, for the purpose of providing electrical conduction for device testing. Aluminum is chosen because of its very low mass density compared to other metals (such as gold), which is beneficial for achieving nanomechanical resonators resonating at higher frequencies[6,12].

The angle of sample rotation is different from the angle of etching direction. Experimentally, we have found that it is necessary to rotate the sample by about 80° in order to achieve an etching angle of about 45°. This indicates that ion beam bending occurs in the electric field perturbed by the presence of the sample. Such bending is due to the low DC bias we use, hence producing low energy ions. On the other hand, the low energy feature of the ions makes sure that the etch rate for most metals is on the order of 1 nm/min or below. This enables us to use ultrathin layer of metallic films, which is compatible with state of the art e-beam lithography to define ultrafine features, thus making ultrasmall mechanical devices.

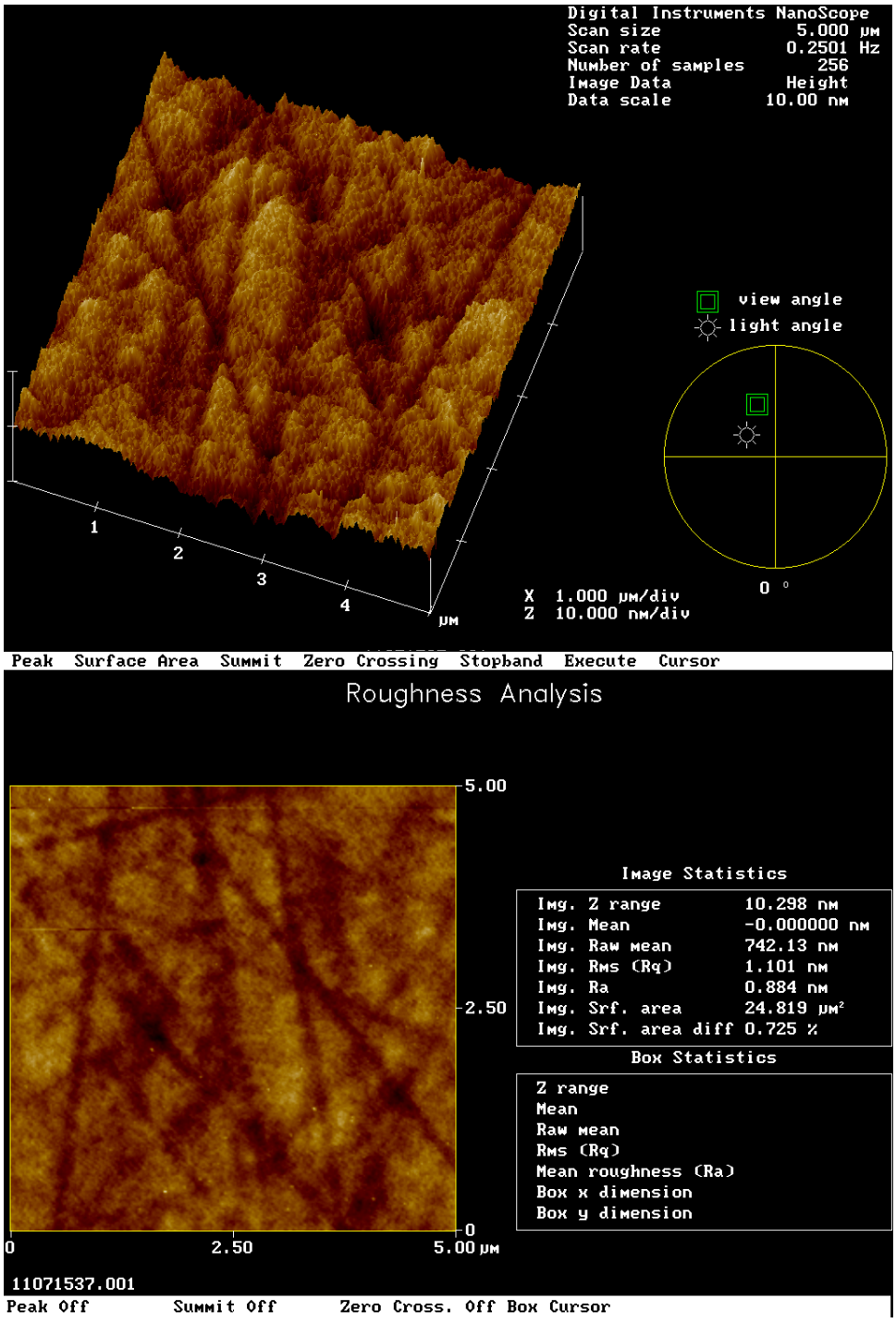

Figure 3.1 AFM scan of the 6H-SiC surface. The RMS surface roughness is about 1 nm.

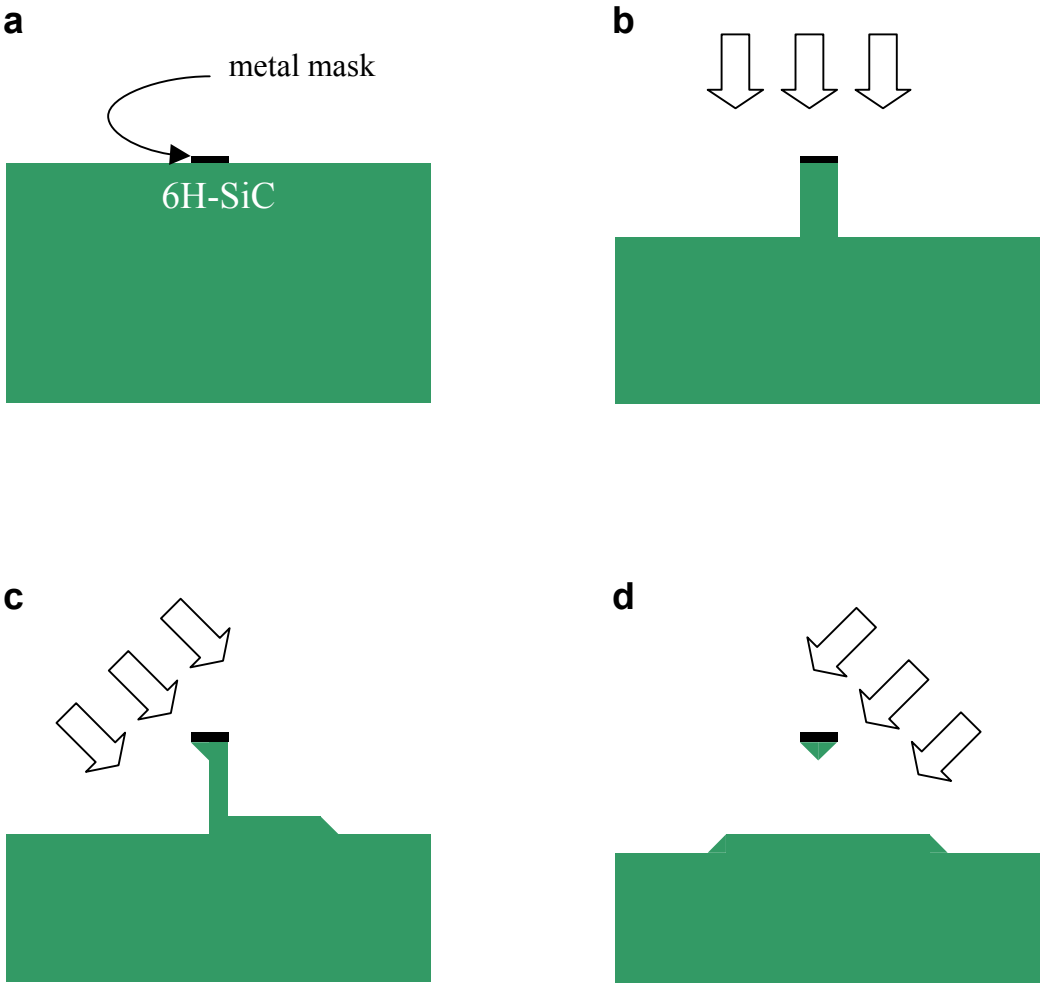

Figure 3.2 Process flow schematics. Block arrows represent ECR etching direction. **a,** Cross-sectional view of the 6H-SiC chip with patterned metallic mask (30 nm Al, followed by 10nm Ti). **b,** After first anisotropic ECR etch with etching direction perpendicular to the wafer surface. **c,** Define the beam length orientation as the axis. Tilt the ECR etching direction by about 45° to do the second ECR etch. **d,** After the third anisotropic ECR etching step with the etching direction tilted to -45°, the doubly clamped beam is suspended with a triangular cross section.

3.3 Measurement of Mechanical Resonance

Using the aforementioned process, nanoscale beams, such as the structure shown in Fig. 3.3, have been fabricated. In this particular example, the beam is approximately 3.3 μm long, 200 nm wide and 200 nm thick at its maximum point. In general, for a beam comprised of two layers of different materials, the resonance frequency can be calculated by[10]

$$f = \frac{\eta}{L^2}\left(\frac{E_1 I_1 + E_2 I_2}{\rho_1 A_1 + \rho_2 A_2}\right)^{1/2}. \qquad (3.1)$$

Here the indices 1 and 2 refer to the properties of the structural and electrode layers, respectively. The constant η depends upon mode number and boundary conditions; for the fundamental mode of a doubly clamped beam η=3.57. $E_{1(2)}$, $\rho_{1(2)}$, $I_{1(2)}$ and $A_{1(2)}$ are Young's modulus, mass density, moment of inertia and cross sectional area of layer 1(2), respectively. Considering the geometry of the doubly clamped beam we fabricated here, the fundamental flexural mode frequency in the plane of the wafer surface (in-plane mode) is calculated to be about 150 MHz.

This structure is a nanomechanical resonator that can be excited into resonance and tested using magnetomotive transduction [6,10,13-16]. Here, the sample is loaded into vacuum, and mounted so that the surface normal is along the direction of the magnetic field. The RF current through the conducting layer of the beam generates an RF force to drive the beam. The frequency of the RF drive is swept. When the driving frequency matches the in-plane fundamental resonance mode frequency of the beam, resonant motion is induced. Such motion cuts the magnetic field lines, and generates an EMF

voltage peak at the mechanical resonance frequency. This EMF is amplified and measured by a network analyzer.

Preliminary testing of the resonator performance of such nanostructures has been performed. Mechanical resonance is detected at about 171.2 MHz, which is consistent with theoretical estimates within fabrication uncertainties of device geometry. After subtracting the background from the raw data, the de-embeded resonance peak is obtained, as shown in Fig. 3.4. Through Lorentzian fit to the resonance curve, the quality factor of the resonance is estimated to be about 3000. The quality factor of the beam is similar to those 3C- beams with similar aspect ratio, indicating the dominance of clamping loss in both cases[17-19]. Even though the performance of nanomechanical components are similar in both 3C- and 6H- SiC cases, with this particular design of device geometry, the low defect property of 6H-SiC wafer has clear advantage for the purpose of integrating mechanical and electronic components on the same chip.

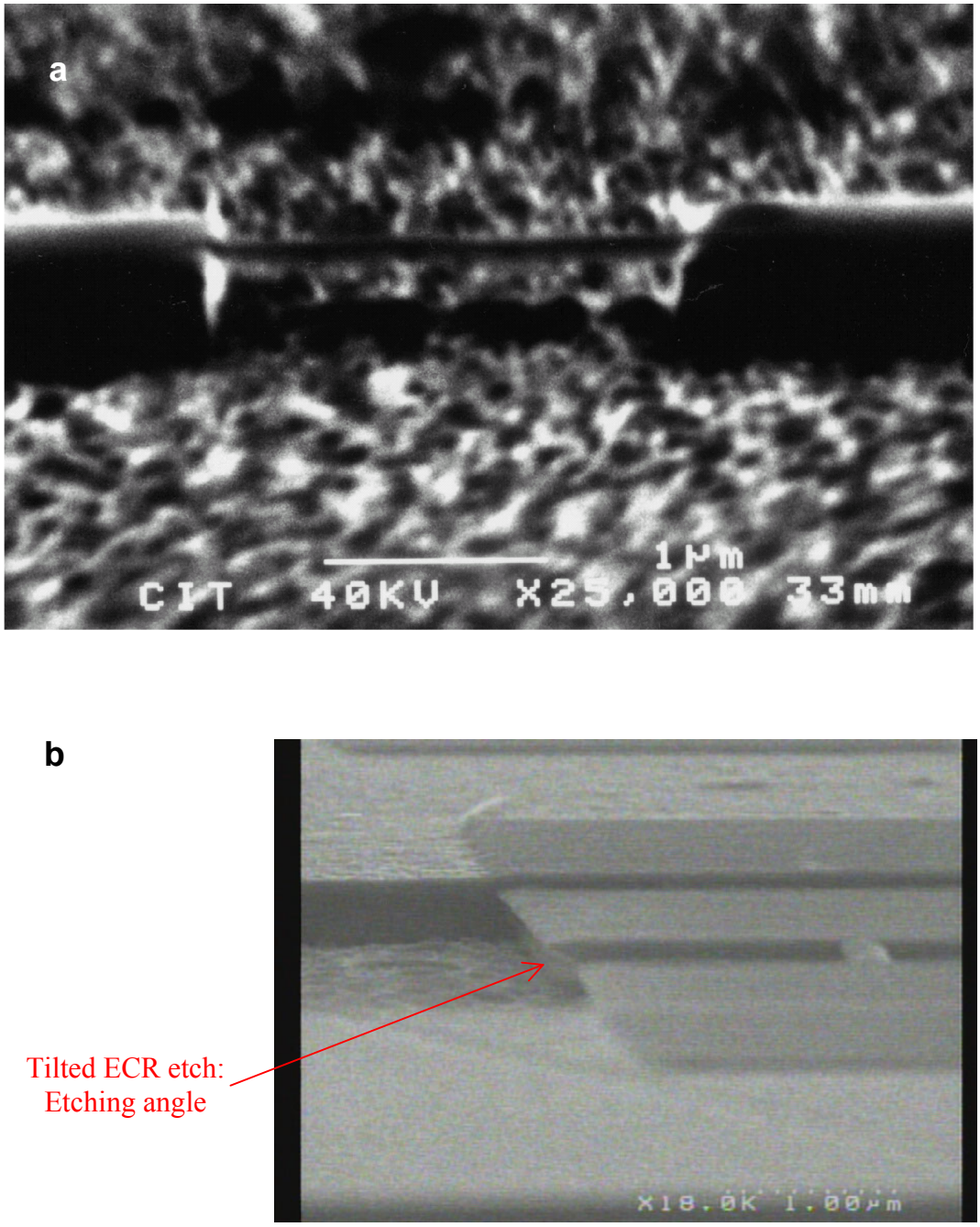

Figure 3.3 Fabrication results.

a, A suspended 6H-SiC doubly clamped beam nanomechanical resonator. **b,** Tilted ECR etch. Etch angle is shown at the edge of the beam supports. This implies that the beam cross section has a triangular shape.

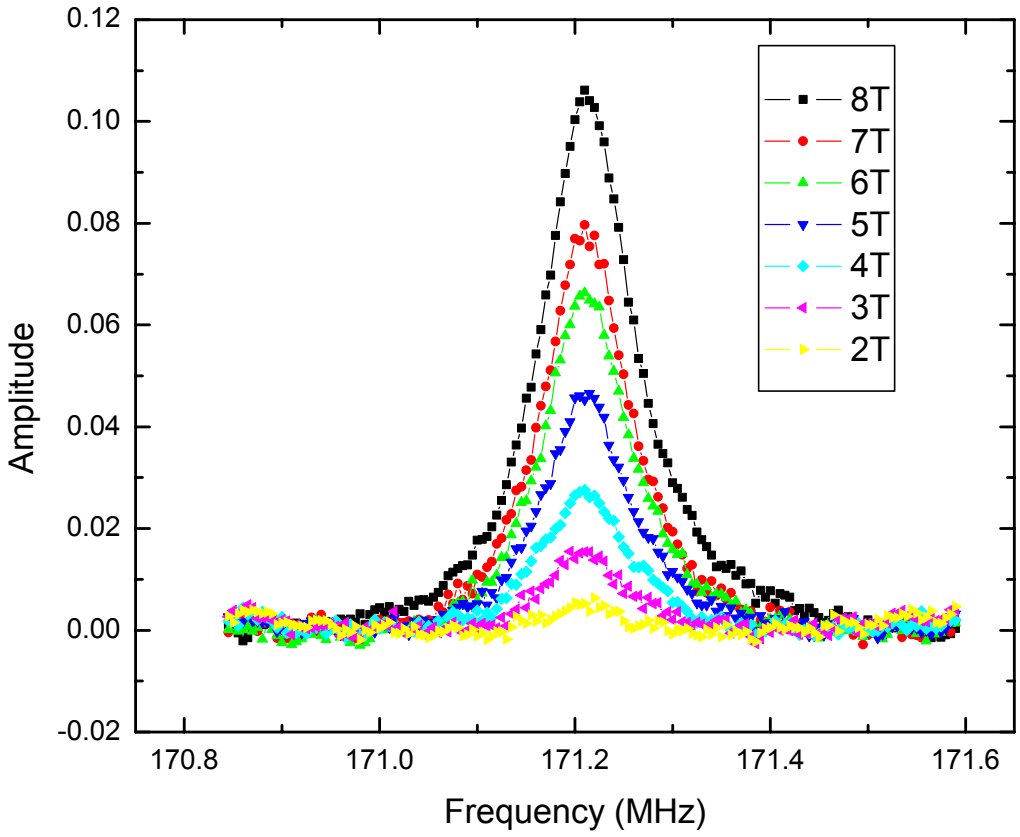

Figure 3.4 Mechanical resonance detected by magnetomotive transduction scheme, with data taken at different B field (from 2T to 8T). Electrical background is subtracted from the raw data, then the quality factor can be extracted from Lorentzian fit, which turns out to be about 3000.

3.4 Conclusions

The ability to fabricate 3-D suspended nanostructures from 6H-SiC is an important breakthrough in NEMS not only because it enables electronic integration, but also because it provides a unique platform for exploring the effects of crystal and surface quality on resonator performance at microwave frequencies.

Acknowledgements: *This work was generously supported by DARPA MTO/MEMS and NSF.*

References

1. Roukes, M. L. Nanoelectromechanical systems face the future. *Phys. World* **14**, 25-31 (2001).

2. Roukes, M. L. Plenty of room indeed. *Sci. Am.* **285**, 48-57 (2001).

3. Nguyen, C. T. C., Katehi, L. P. B. & Rebeiz, G. M. Micromachined devices for wireless communications. *Proc. IEEE* **86**, 1756-1768 (1998).

4. Tilmans, H. A. C. MEMS components for wireless communications. *Sensors and Actuators*, review paper to be published (2003).

5. Mehregany, M., Zorman, C. A., Rajan, N. & Wu, C. H. Silicon carbide MEMS for harsh environments. *Proc. IEEE* **86**, 1594-1610 (1998).

6. Huang, X. M. H., Zorman, C. A., Mehregany, M. & Roukes, M. L. Nanodevice motion at microwave frequencies. *Nature* **421**, 496 (2003).

7. Serre, C. et al. Test microstructures for measurement of SiC thin film mechanical properties. *J. Micromech. Microeng.* **9**, 190-193 (1999).

8. Tong, L. U. & Mehregany, M. Mechanical-properties of 3C- silicon carbide. *Appl. Phys. Lett.* **60**, 2992-2994 (1992).

9. Zorman, C. A. et al. Epitaxial-growth of 3C-SiC films on 4 inch diam (100)silicon- wafers by atmospheric-pressure chemical-vapor-deposition. *J. Appl. Phys.* **78**, 5136-5138 (1995).

10. Yang, Y. T. et al. Monocrystalline silicon carbide nanoelectromechanical systems. *Appl. Phys. Lett.* **78**, 162-164 (2001).

11. Ivanov, P. A. & Chelnokov, V. E. Recent developments in SiC single-crystal electronics. *Semicond. Sci. Technol.* **7**, 863-880 (1992).

12. Huang, X. M. H., Zorman, C. A., Mehregany, M. & Roukes, M. L. Quality factor issues in silicon carbide nanomechanical resonators. in *Digest of Technical Papers, volume 1, Transducers'03, the 12th International Conference on Solid-State Sensors, Actuators and Microsystems,Boston, MA, USA, June 8-12, 2003,* (ISBN: 0-7803-7732-X), 722-725 (2003).

13. Cleland, A. N. & Roukes, M. L. Fabrication of high frequency nanometer scale mechanical resonators from bulk Si crystals. *Appl. Phys. Lett.* **69**, 2653-2655 (1996).

14. Cleland, A. N. & Roukes, M. L. A nanometre-scale mechanical electrometer. *Nature* **392**, 160-162 (1998).

15. Cleland, A. N. & Roukes, M. L. External control of dissipation in a nanometer-scale radiofrequency mechanical resonator. *Sens. Actuator A-Phys.* **72**, 256-261 (1999).

16. Ekinci, K. L., Yang, Y. T., Huang, X. M. H. & Roukes, M. L. Balanced electronic detection of displacement in nanoelectromechanical systems. *Appl. Phys. Lett.* **81**, 2253-2255 (2002).

17. Wang, K., Yu, Y., Wong, A. C. & Nguyen, C. T.-C. VHF free-free beam high-Q micromechanical resonators. in *Technical Digest, 12th International IEEE Micro Electro Mechanical Systems Conference, Orlando, Florida, Jan. 17-21, 1999* (ISBN: 0780351975), 453-458 (1999).

18. Hsu, W.-T., Clark, J. R. & Nguyen, C. T.-C. Q-optimized lateral free-free beam micromechanical resonators. in *Digest of Technical Papers, Transducers'01, the 11th International Conference on Solid State Sensors & Actuators, Munich, Germany, June 10-14, 2001* (ISBN: 3540421505), 1110-1113 (2001).

19. Huang, X. M. H., Prakash, M. K., Zorman, C. A., Mehregany, M. & Roukes, M. L. Free-free beam silicon carbide nanomechanical resonators. in *Digest of Technical Papers, volume 1, Transducers'03, the 12th International Conference on Solid-State Sensors, Actuators and Microsystems,Boston, MA, USA, June 8-12, 2003,* (ISBN: 0-7803-7732-X), 342-343 (2003).

PART II

BOTTOM-UP NEMS: NANOTUBES

Chapter 4

Potentialities and Limitations of Magnetomotive Transduction in Studying Nanotube Mechanical Motion

Magnetomotive transduction scheme has been successfully applied to the study of micro- and nano- scale mechanical resonators in the past. When the size scale approaches that of a single molecule, comparable to that of a single single-walled nanotube, the validity of this method needs to be re-assessed. In this chapter, we experimentally study the eddy current damping mechanism in the context of the proposed SWNT motion detection by magnetomotive transduction. A specially designed high aspect ratio SiC nanowire resonator is fabricated by top-down e-beam lithography to serve as a *dummy nanotube*, which is capable of providing information about this dissipation mechanism in a more easily fabricated structure of larger size scale. Such information will be important for future data interpretation, when we actually perform similar experiments on molecular scale devices.

4.1 Introduction

Magnetomotive transduction technique[1-5] has played a very important role in a series of recent achievements involving gigahertz silicon carbide nanomechanical resonators[6] and platinum nanowire resonators[7]. There has been tremendous interest in attempting to use this method for studying mechanical motion of single-walled nanotubes[8], and molecular-scale objects in general. However, the validity of this technique needs to be re-assessed when such deep nanoscale is experimentally accessed. As recently pointed out by Schwab[9], eddy current damping force caused by this transduction scheme will become important. Such mechanism was carefully studied by Cleland and Roukes[3] and usually can be easily made negligible, but will become crucial for single molecules, such as a single-walled nanotube (SWNT). In this chapter, we have designed a high aspect ratio silicon carbide nanowire resonator to serve as a *dummy nanotube* to study this dissipation mechanism by simulating the situation to be faced by single-walled nanotubes.

4.2 Magnetomotive Transduction and Eddy Current Damping

The basics of magnetomotive transduction scheme has been extensively discussed elsewhere[1-5]. Briefly, we use a doubly clamped beam nanowire resonator, which is placed in a magnetic field perpendicular to the direction of nanowire axis. An rf current is sent through the conducting layer of the beam. The frequency of the current is swept. When this driving frequency matches the in-plane fundamental resonance frequency of the nanowire, resonant motion is induced. Such motion cuts the magnetic field line, and

induces an EMF voltage across the beam. Mechanical resonance is detected by measuring this additional EMF voltage on top of the electrical driving background.

In the magnetomotive transduction scheme, we rely on the EMF voltage generated by the motion to infer the action of the nano-resonator. As pointed out by Cleland and Roukes[3], no additional dissipation is expected when the external impedance seen by the EMF voltage source is infinite. Of course, this is generally not the case for practical high-frequency measurements. As a result, eddy currents in addition to the driving current present due to the EMF, thus generating an additional force, which is always opposed to the velocity and leads to dissipation.

Quantitatively, we express the quality factor Q by

$$\frac{1}{Q} = \frac{1}{Q_M} + \frac{1}{Q_E} = \frac{1}{m\omega_0}(\beta_M + \beta_E) \ , \tag{4.1}$$

where Q_M is the mechanical quality factor, β_M is the mechanical damping constant. Q_E, β_E are the partial quality factor and eddy current damping constant due to the loss from EMF induction[9], where β_E is defined as

$$\beta_E \equiv \frac{\partial I}{\partial V} B^2 l^2 \ , \tag{4.2}$$

where I and V are current and voltage across the beam, l is the length of the beam. Eq. (4.1) is valid if the dissipation processes are independent.

For low operating frequencies, $\frac{\partial V}{\partial I}$ can be made large to minimize the effect. However, this becomes not practical at high frequencies due to the unavoidable parasitic components in the electronic circuitry.

4.3 *Dummy Nanotube* Test Results and Discussions

The doubly clamped beam nanowire resonator we use here is made out of 3C-SiC thin film (75 nm thick), fabricated by top-down nanolithography. The nanowire beam is about 15 μm long, 0.15 μm wide, with 45nm Al, followed by 5 nm Ti on top as etch mask, and for electrical conduction. The fabrication process has been discussed elsewhere[6,10]. SEM micrographs of the suspended nanostructure for this experiment are shown in Fig. 4.1.

The device is wire-bonded, loaded into an evacuated dipper and cooled down to liquid-helium temperatures. A strong magnetic field is applied perpendicular to the sample surface. Fundamental mode mechanical resonance is detected at 12.76958 MHz. Fig. 4.2 shows the resonance curve at different driving voltage, at a constant B field value of 6 Tesla. At high driving amplitude, the device will perform as a standard nonlinear Duffing oscillator. This result enables us to choose a drive, so as to work within the linear regime for the resonator.

The resonance curve at different B field is plotted in Fig. 4.3. The driving voltage is chosen to be 1 μV. The maximum amplitude vs. B^2 is shown in the insert of Fig. 4.3, which differs significantly from a linear dependence found in the literature[2,10]. It resembles linear dependence only at low field values. Obviously, such deviation is due to the increase of dissipation at higher B field values. Quality factor Q is experimentally determined from these traces by Lorentzian fit to the resonance curves, and calculating

$$Q = \frac{\omega_0}{\Delta\omega} , \tag{4.3}$$

where ω_0 is the resonance center frequency, $\Delta\omega$ is the full width at half maximum of power spectra.

Fig. 4.4 is a plot of $1/Q$ vs. B^2, which is linear, as expected from Eq. (4.1). From the intercept of the linear fit, we can calculate Q_M is about 50,000, which is the quality factor of the resonator without additional loss caused by the magnetomotive transduction scheme.

When we come to the point of experimenting with an actual single SWNT resonator, for example, of 1 micron length with doubly clamped boundary condition, eddy current damping is expected to be dominant at 8T, making Q to be on the order of 100. As we reduce the B field to 1T, Q should increase, and approach the order of 10^4 (if other dissipation processes contribute much less dissipation than the eddy current damping at 1 Tesla B field). This can be considered a signature of nanotube motion to look for.

The sensitivity of such detection is limited by the first stage electrical amplifier noise, when the signal is optimally coupled to the amplifier. Nonideal coupling will reduce the sensitivity further, thus it's important to improve impedance matching between the device output and amplifier input. This is technically difficult, but do-able.

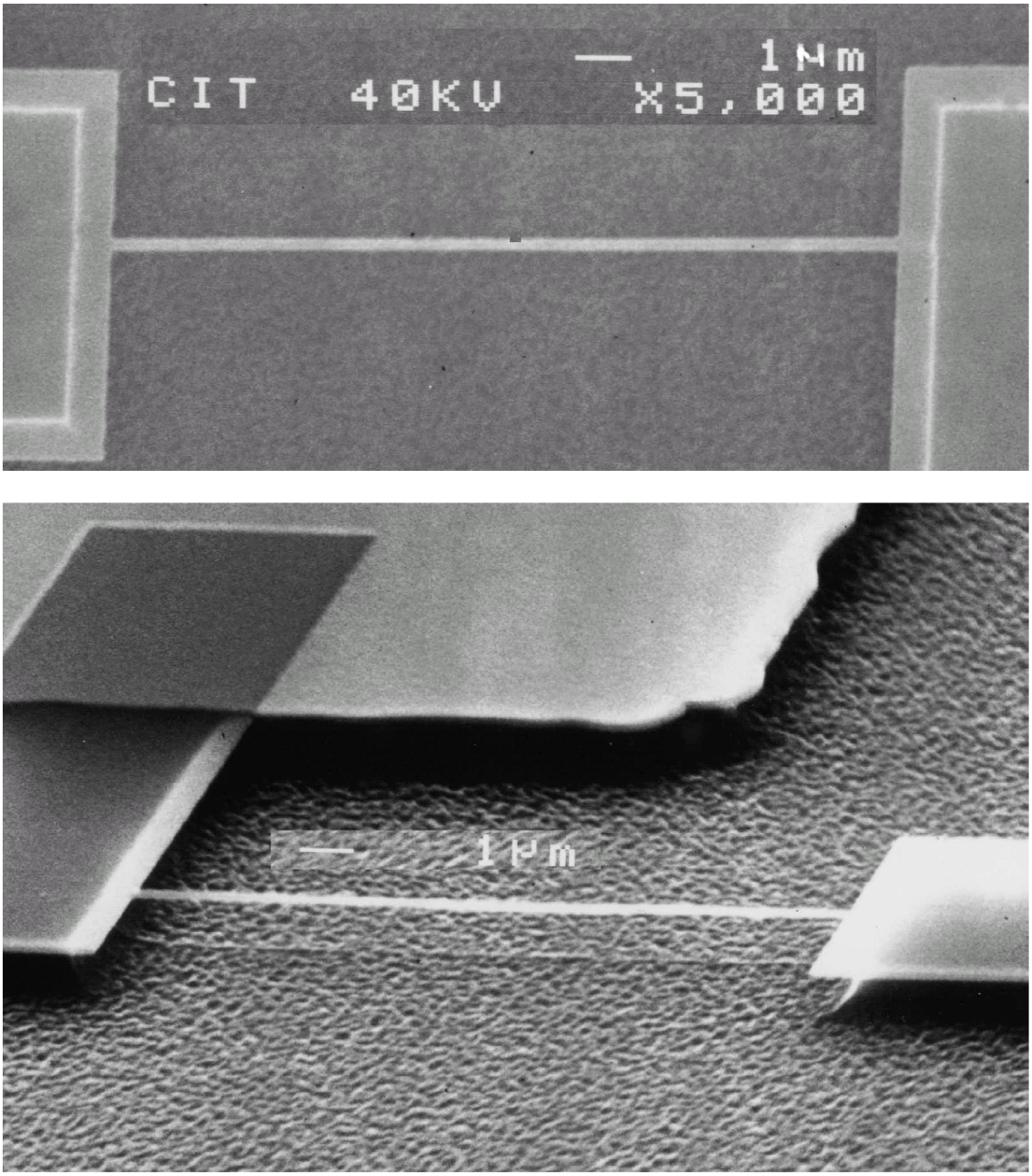

Figure 4.1 SEM micrographs of suspended SiC doubly clamped beam resonator. The device is metallized by 45 nm Al, followed by 5 nm Ti. The beam is about 15 μm long, 150 nm wide. (top) Top view of the device; (bottom) Side view of the device.

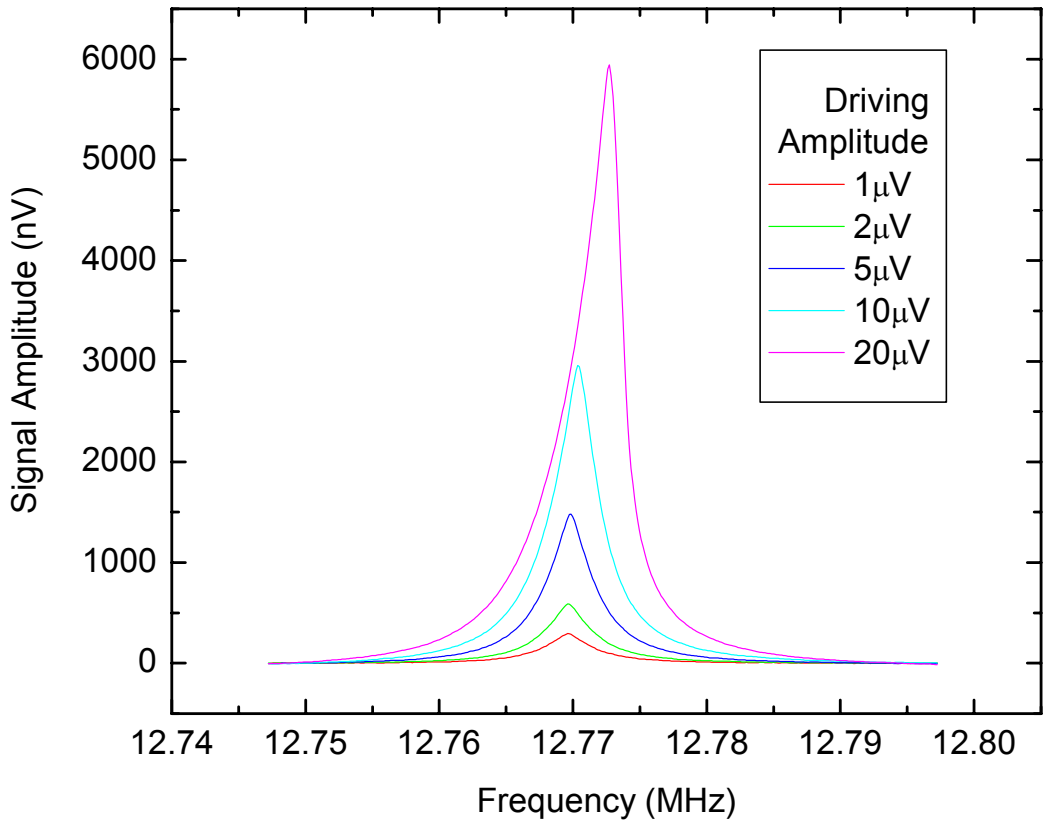

Figure 4.2 Resonance curve at different driving amplitude. Data taken at constant B field of 6 T.

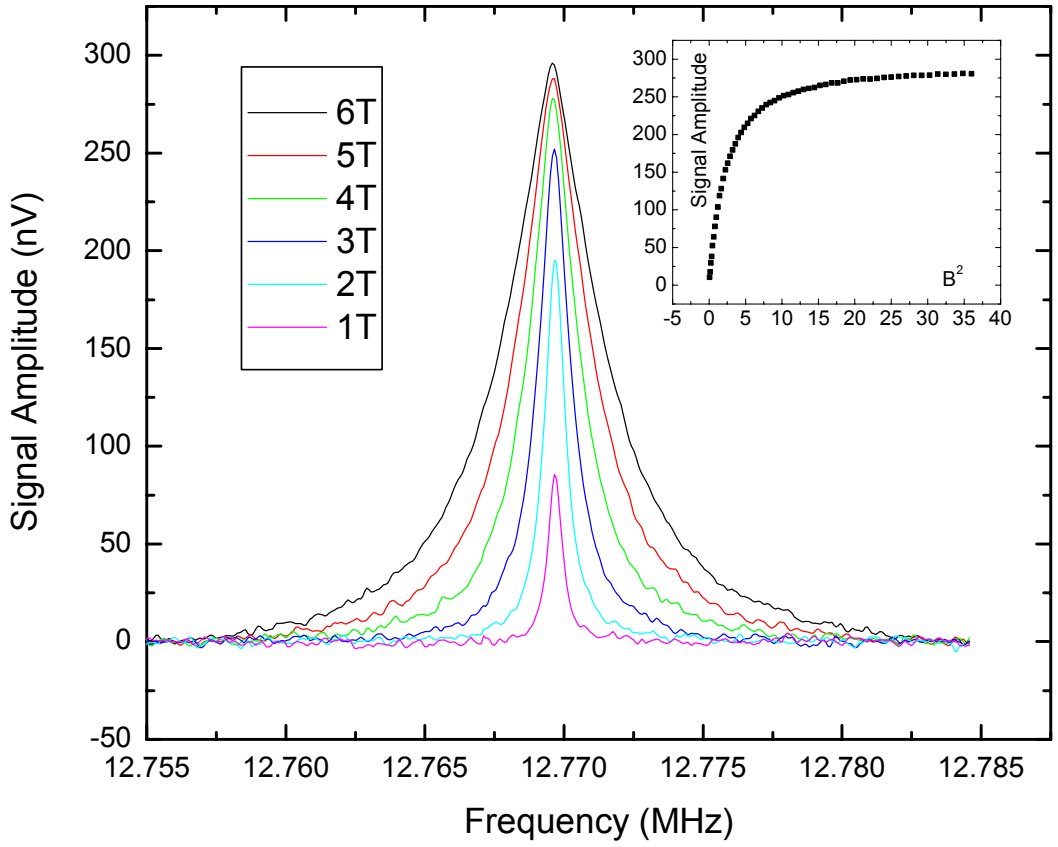

Figure 4.3 Measured resonance curve at different B field. The maximum resonance amplitude is plotted vs. B^2 in the insert, which deviate significantly from the usual linear dependence. Data taken at driving amplitude of 1 μV.

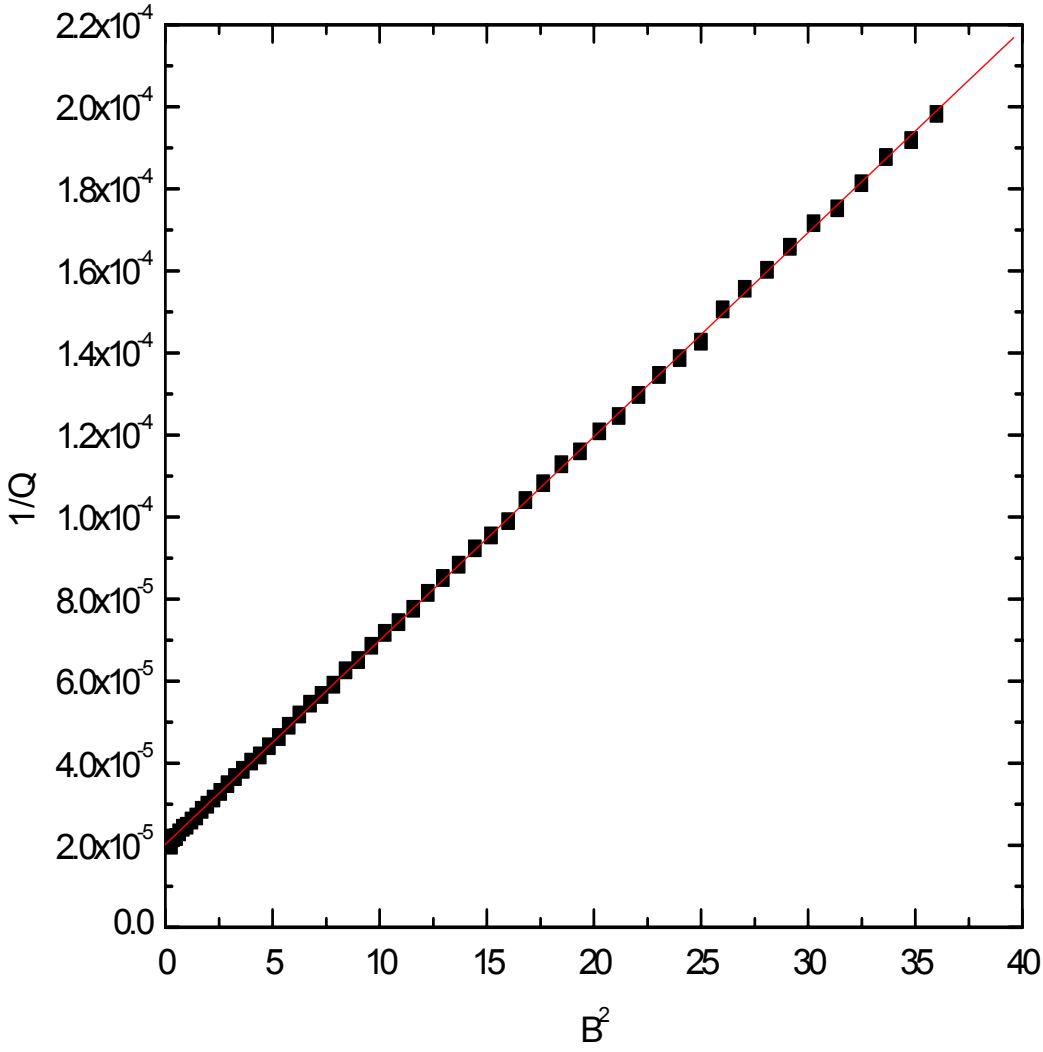

Figure 4.4 Dissipation (1/Q) vs. B^2 plot.

4.4 Conclusions

We thus conclude that magnetomotive transduction scheme may still be useful in studying fundamental flexural mode molecular motion. However, the experimental signature would be different from what we know from previous micro- and nano- scale experiments. The results discussed in this paper will be crucial in data interpretation for future experiments to be performed on single molecules.

Acknowledgements: *This work was generously supported by DARPA and NSF.*

References

1. Cleland, A. N. & Roukes, M. L. A nanometre-scale mechanical electrometer. *Nature* **392**, 160-162 (1998).

2. Cleland, A. N. & Roukes, M. L. Fabrication of high frequency nanometer scale mechanical resonators from bulk Si crystals. *Appl. Phys. Lett.* **69**, 2653-2655 (1996).

3. Cleland, A. N. & Roukes, M. L. External control of dissipation in a nanometer-scale radiofrequency mechanical resonator. *Sens. Actuator A-Phys.* **72**, 256-261 (1999).

4. Ekinci, K. L., Yang, Y. T., Huang, X. M. H. & Roukes, M. L. Balanced electronic detection of displacement in nanoelectromechanical systems. *Appl. Phys. Lett.* **81**, 2253-2255 (2002).

5. Harrington, D. A. Ph.D. Thesis. (Caltech, 2003).

6. Huang, X. M. H., Zorman, C. A., Mehregany, M. & Roukes, M. L. Nanodevice motion at microwave frequencies. *Nature* **421**, 496 (2003).

7. Husain, A., Hone, J., Postma, H. W. C., Huang, X. M. H., Drake, T., Barbic, M., Scherer, A. & Roukes, M. L. Nanowire-based very-high-frequency electromechanical resonator. *Appl. Phys. Lett.* **83**, 1240-1242 (2003).

8. Saito, R., Dresselhaus, G. & Dresselhaus, M. S. *Physical Properties of Carbon Nanotubes* (Imperial College Press, Singapore, 2001).

9. Schwab, K. Spring constant and damping constant tuning of nanomechanical resonators using a single-electron transistor. *Appl. Phys. Lett.* **80**, 1276-1278 (2002).

10. Yang, Y. T., Ekinci, K. L., Huang, X. M. H., Schiavone, L. M., Roukes, M. L., Zorman, C. A. & Mehregany, M. Monocrystalline silicon carbide nanoelectromechanical systems. *Appl. Phys. Lett.* **78**, 162-164 (2001).

Chapter 5

Design of a Nanotube-Based Magnetomechanical Resonator for Zeptonewton Force Detection

Magnetic resonance force microscopy (MRFM)[1] aims to achieve three-dimensional imaging of biological macromolecules with atomic resolution. Despite significant advances in improving the force sensitivity of mechanical resonators, achieving the ultimate goals of MRFM is still an open challenge. Here we propose a novel device structure, using a nanotube carrying a single domain nanomagnet[2] paddle, to form a torsional mechanical resonator. This device design appears capable of force sensing with zeptonewton/Hz$^{1/2}$ sensitivity at room temperature, which is essential for realizing 3-D nuclear magnetic resonance imaging by MRFM with atomic resolution.

5.1 Introduction

Three-dimensional imaging of individual biological molecules is a great challenge for microscopy. One plausible approach to achieve this goal is through imaging of individual nuclear spins carried by each atom in the molecule. In principle, this can be realized by magnetic resonance force microscopy (MRFM)[1]. This technique was first proposed by Sidles[1], and later demonstrated by Rugar et al.[3,4] and Hammel et al.[5]. MRFM requires a mechanical resonator with extremely high force sensitivity and a magnetic probe tip that is capable of atomic spatial resolution. Even though efforts to date have been quite impressive in improving force sensitivity and spatial resolution, there is still a long way to go towards the ultimate goal of 3-D biomolecular imaging.

The device used by Rugar and his collaborators relies heavily on the small spring constant of a large aspect ratio cantilever, which yields the sub-attonewton force sensitivity at 300 mK temperatures[6]. Here we propose an alternative device structure based on nanotubes, which supports a single domain nanomagnet paddle. We utilize the excellent mechanical properties of nanotubes[7-9], to allow an extremely low torsional spring constant, and thus an extremely high torque sensitivity. When such torque is applied in the form of an applied force onto one end of the paddle, it appears that it may be possible to attain ultrahigh force sensitivity, even below 10^{-19} N/$\sqrt{\text{Hz}}$ (100 zN/$\sqrt{\text{Hz}}$).

5.2 Device Design Principle

The basic structure of the device is shown in Fig. 5.1. The axle is a section of a single nanotube.

The paddle is a single domain nanomagnet, which is a piece of Ni (or NiFe) with typical dimensions of 1 μm long, 100 nm wide, 50 nm thick.

The torsional spring constant of the resonator is dominated by that of the axle, while the moment of inertia is mainly from the paddle.

For small oscillations, the equation of motion for linear mechanical resonators, torsional mechanical resonators, and electrical resonators with one degree of freedom can all be described by the same differential equation[10].

Applying the simple harmonic oscillator approximation for small motional amplitude, the equation of motion for the torsional case can be written as

$$I\ddot{\varphi} + c_R\dot{\varphi} + k_R\varphi = T_0 \sin \omega t \ , \tag{5.1}$$

where I is the moment of inertia of the resonator, c_R is the torsional damping coefficient, k_R is the torsional spring constant, $T_0 \sin \omega t$ is the external torque.

The fundamental torsional mode resonance frequency can be calculated by

$$f_0 = \sqrt{\frac{k_R}{I}} \ . \tag{5.2}$$

The torsional spring constant k_R can be calculated by[10]

$$k_R = \frac{\pi G(D^4 - d^4)}{8L} \approx \frac{\pi G D^4}{8L} \ , \tag{5.3}$$

where G is the shear modulus of the nanotube, D and d are its outer and inner diameter, L is the total length of the suspended nanotube section used for supporting the paddle. In terms of the moment of inertia, the contribution from the nanotube I_{tube} is much smaller than that from the paddle. Ignoring the contribution from the nanotube, we have

$$I = I_{tube} + I_{paddle} \approx I_{paddle} = \frac{1}{12} m l^2 \ , \tag{5.4}$$

where m is the mass of the paddle, l is the length of the paddle.

The fundamental limit for the torque sensitivity of the device is dominated by thermomechanical noise. The thermal noise spectral density for torque is

$$\begin{aligned} S_T^{1/2} &= \sqrt{\frac{4k_B T k_R}{Q\omega_0}} \\ &= \sqrt{\frac{4k_B T k_R}{2\pi\left(\sqrt{\frac{k_R}{I}}\right)Q}} \\ &= \sqrt{\frac{2k_B T}{\pi Q}\sqrt{k_R I}} \\ &= \sqrt{\frac{2k_B T}{\pi Q}\sqrt{\frac{\pi G D^4}{8L}\cdot\frac{1}{12}(\rho l w t) l^2}} \end{aligned} \quad . \qquad (5.5)$$

We note that the torsional spring constant is proportional to D^4, thus smaller tube diameter is crucial for achieving extremely high sensitivity. For nanostructures that can be made by top-down e-beam lithography, the feature size is about an order of magnitude larger than single walled nanotube (SWNT) diameter, thus 10^4 larger in spring constant, contributing an order of magnitude reduction in force sensitivity.

In order to test the torque sensitivity of the device (and effective force sensitivity, if a net force is applied, that is predominantly distributed at the probe tip end of the paddle), we have an electric circuit on chip (see Fig. 5.1), which allows an ac current to run close to the probe tip end of the paddle. A "test magnetic moment" (whose value can be calculated numerically) can be generated by the current.

The above summarizes the mechanical resonator part of the device. The expected properties of some typical devices of this kind are shown in Fig. 5.2. We assume the paddle geometry to be l = 1 μm long, w = 100 nm wide, t = 50 nm thick. The total length

of the nanotube section is $L = 1\ \mu m$. Then, we immediately know the torsional spring constant (Fig. 5.2a) and the fundamental torsional mode resonance frequency (Fig. 5.2b) for different nanotube diameters. The thermomechanical noise torque spectral density is calculated for different temperatures and different quality factors, as shown in Fig. 5.2c.

For certain measurement orientations, the paddle itself could serve as a probe magnet in MRFM experiment. When the nanomaget tip is brought close to a spin the magnetic resonance occurs at the frequency

$$\omega_{0,magnetic} = \gamma \cdot B(\vec{r}) \ , \tag{5.6}$$

where γ is the gyromagnetic ratio, $B(\vec{r})$ is the local B field value at the location $\vec{r}$.

The magnetic resonance is excited by an rf or microwave coil, with proper orientation (depending on the specific MRFM protocol taken[11,12]). There are different ways to couple the magnetic resonance to the mechanical resonance, as summarized by Sidles[1]. Transverse detection of MRFM matches the magnetic and mechanical resonance frequency, so that the oscillating magnetic moment will apply an oscillating force on the mechanical resonator at its natural frequency. Due to technical challenges, this has not yet been demonstrated so far. Instead, detection of longitudinal moment has been demonstrated experimentally, e.g., through cyclic modulation to the gradient field, at half of the mechanical resonance frequency.

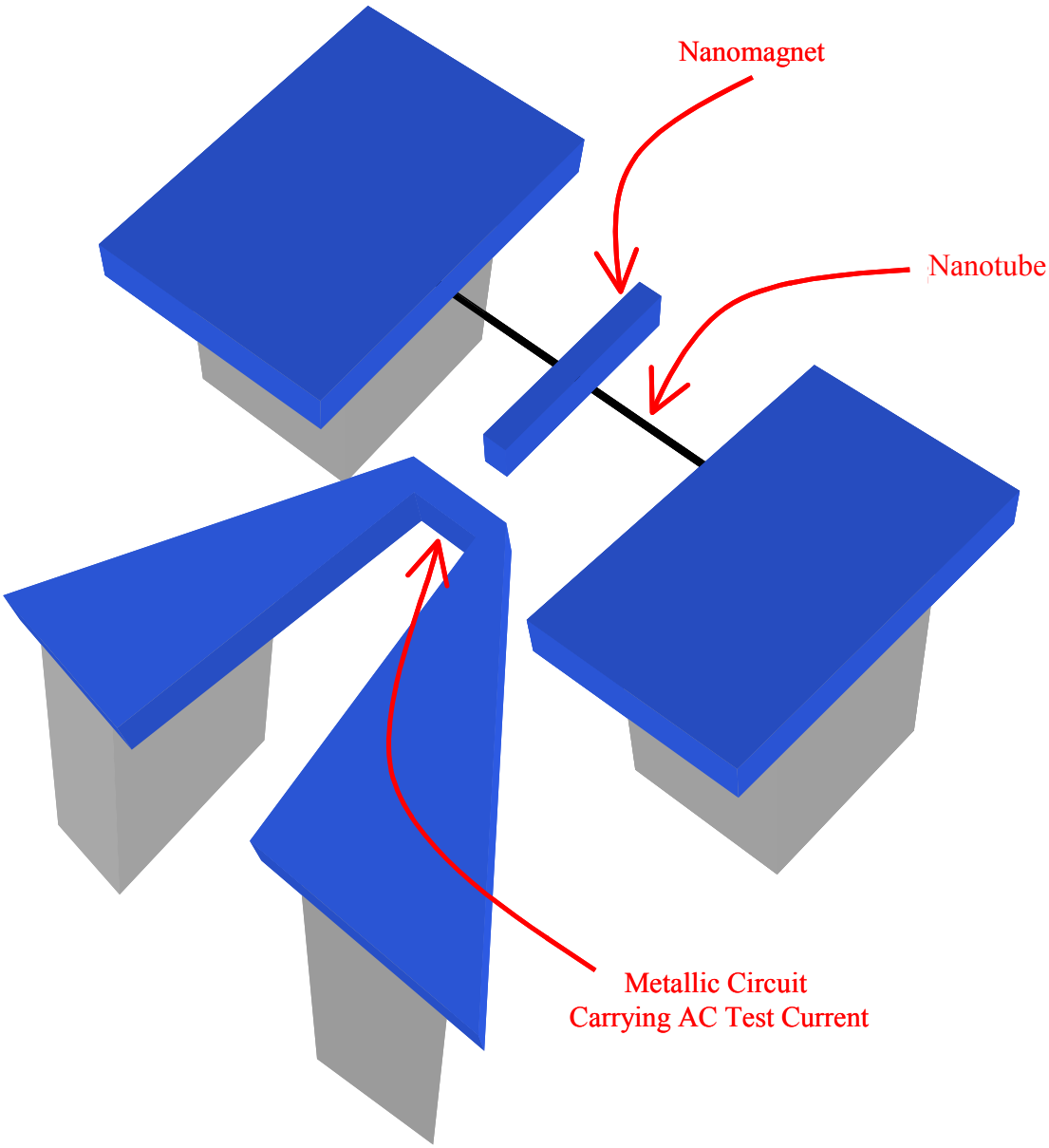

Figure 5.1 Device schematics.

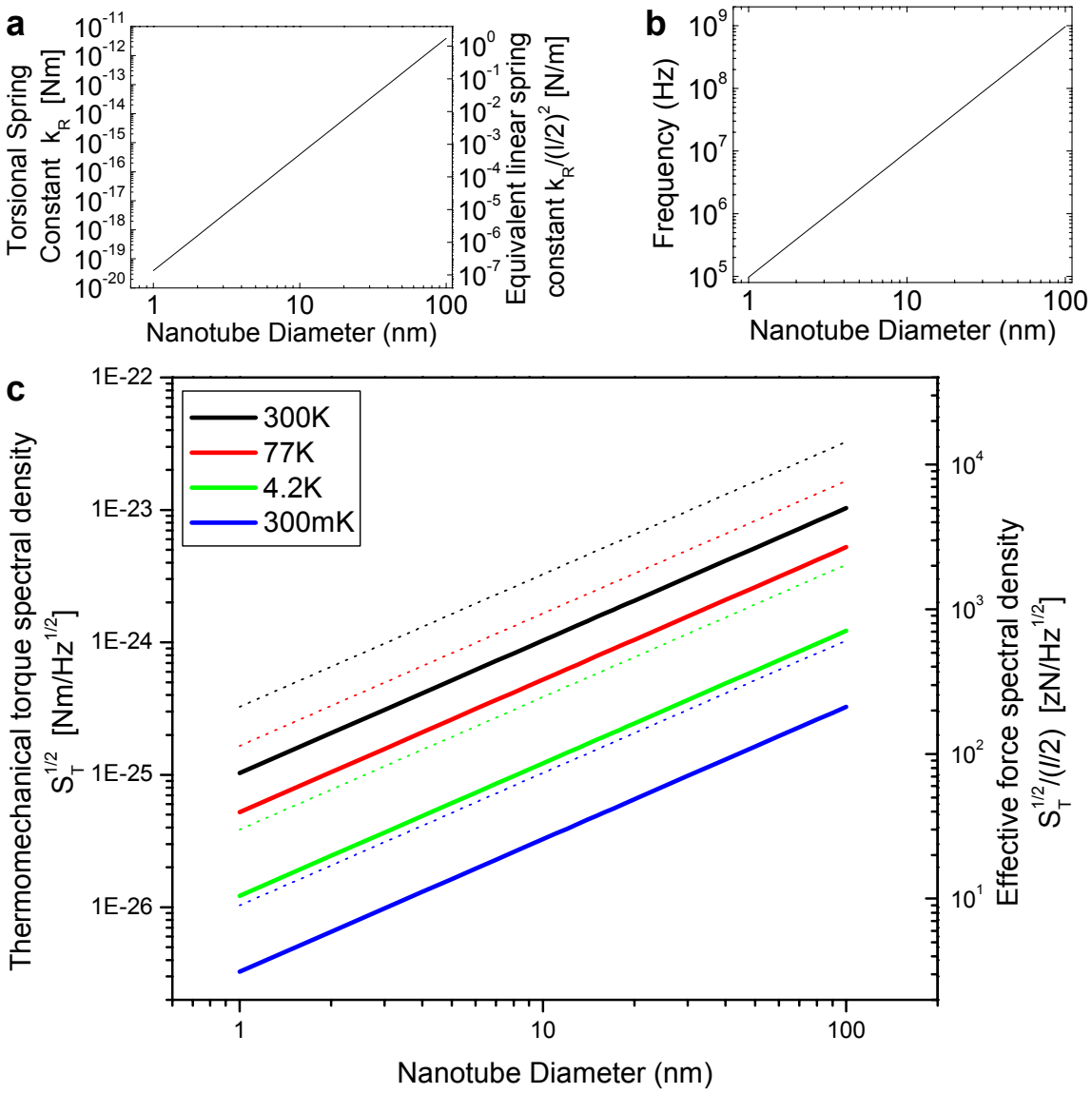

Figure 5.2 The expected properties of some typical devices. We assume the paddle geometry to be l = 1 μm, w = 100 nm, t = 50 nm. The total length of the nanotube section is L = 1 μm. We assume the torque spectrum is generated by a force spectrum applied at the probe end of the paddle, the equivalent linear spring constant and the effective force spectral density can then be defined. **a,** Torsional spring constant and its equivalent linear spring constant vs. nanotube diameter plot. **b,** Fundamental torsional mode resonance frequency vs. nanotube diameter plot. **c,** The thermomechanical noise torque spectral density at different temperatures is plotted vs. nanotube diameter, assuming $Q \sim 10^5$ (solid lines), or $Q \sim 10^4$ (dotted lines).

5.3 Resonance Measurement Scheme

One straightforward approach to measurement of the resonance frequencies is through use of a commercial scanning electron microscope (SEM).[13,14] In this case the sample is rotated by 45 degrees with the length of the paddle as the axis. The electron beam is focused on a point near the detection end, and near the edge of the paddle. The output signal from a photomultiplier (serving as a secondary electron detector) is monitored using a spectrum analyzer to detect mechanical displacement (see Fig. 5.3). The work by Buks and Roukes has demonstrated displacement sensitivity at the level of $4\times10^{-13}\,\mathrm{m}/\sqrt{\mathrm{Hz}}$, and their setup has been experimentally proven to be useful for resonance frequencies up to about 10 MHz.

The spectral density for angular displacement response on resonance is

$$S_\theta^{1/2} = S_T^{1/2}\cdot\frac{Q}{k_R} = \sqrt{\frac{2k_BTQ}{\pi}\sqrt{k_RI}}\cdot\frac{1}{k_R} \quad . \tag{5.7}$$

The known parameters of the beam allow determination of the scaling factor translating the signal of the spectrum analyzer to actual angular displacement noise. $S_\theta^{1/2}\cdot(l/2)$ gives the displacement noise peak at the detection point where the electron beam is focused.

Corresponding to the devices discussed in Fig. 5.2 (assuming the paddle geometry to be l = 1 μm long, w = 100 nm wide, t = 50 nm thick. The total length of the nanotube section is L = 1 μm. Here, assuming the quality factor of the device to be $Q\sim10^5$), the calculated angular displacement response is plotted for different temperatures (solid

lines) in Fig. 5.4. The dotted lines are effective force sensitivity contours, which defines the dependence with the same thermomechanical force spectral density.

To assess the practical limits to the motion transduction scheme proposed here, it is necessary to consider both the electron recoil back action noise and electron shot noise induced fluctuations in (angular) displacement readout.

When electrons get scattered by the paddle, momentum transfer occurs in the process. This causes random motion of the paddle, which, in turn, induces fluctuation in the readout. This noise process is called electron recoil back action noise. On the other hand, electron shot noise is caused by the discreteness of electrons. Statistical fluctuations of the number of electrons in the primary beam are transduced into fluctuations in the number of electrons that reach the detector. Both of these noise processes cause the readout to fluctuate, thus impose lower limits for the smallest angular displacement that can possibly be detected.

Analogous to the optical case[15], the force spectral density of electron recoil back action noise can be written as

$$S_{F,ba}^{1/2} = \sqrt{4IVh/\upsilon\lambda} = \sqrt{4IVm_e} \ , \tag{5.9}$$

where υ is the velocity of the electrons, λ is the electron wavelength, h is Planck's constant, m_e is the mass of the electrons, I and V are e-beam current and acceleration voltage, respectively. For beam current of 1 pA and acceleration voltage of 1 kV, we have $S_{F,ba}^{1/2} = 60 \text{ pN}/\sqrt{\text{Hz}}$. The corresponding angular displacement noise can be calculated by

$$S_{\theta,ba}^{1/2} = \frac{Q}{k_R} S_{F,ba}^{1/2}(l/2) \ . \tag{5.10}$$

The results are added to Fig. 5.4 for 1 kV acceleration voltage, and beam currents of 1 pA and 1 fA, respectively.

Electron beam shot noise causes the beam current to fluctuate, with a current spectral density

$$S_I^{1/2} = \sqrt{\frac{2}{3} eI} \quad . \tag{5.11}$$

This current noise causes fluctuations in the displacement readout,

$$S_{x,shot}^{1/2} \propto \frac{S_{I,shot}^{1/2}}{I} \propto \frac{1}{\sqrt{I}} \quad . \tag{5.12}$$

It has been determined by Buks and Roukes, in a separate experiment on the JEOL 6400 SEM in our lab[13,14], that the sensitivity of our displacement detection scheme is about 4×10^{-13} m/$\sqrt{\text{Hz}}$. In their work, the operating e-beam current is 100 pA, and the electron recoil back action noise is expected to be negligible for the devices used in their test. Here, we can use such result to infer an upper bound for electron shot noise induced fluctuation in our specific setup. Such shot noise upper bound at other e-beam currents can then be deduced. These are also plotted in Fig. 5.4.

Another important consideration is the minimization of device heating due to electron bombardment. This will impose a practical and unavoidable constraint upon the beam current used to sense resonator motion. The energy absorbed by the sample depends on the penetration depth of electrons and on the thickness of the metal layer. But in the worst extreme case, all of the e-beam power $I \cdot V$ gets absorbed by the paddle, and the only pathway to transfer the heat to the environment is through the nanotube section supporting the paddle. In equilibrium, the temperature increase on the paddle can be roughly estimated by

$$\Delta T_{\max} \le \frac{\Theta / 2}{\mathrm{K}} \cdot (l / 2) \ , \tag{5.13}$$

where Θ is heat flux, K is thermal conductivity. For thermal conductivity of nanotubes, measured[16,17] to be larger than $200\ \mathrm{W/(m \cdot K)}$, we can estimate the upper limit in heating for our example devices described above.

Using 1 pA beam current measuring a device at room temperature, we have $\Delta T_{\max} \sim 3\ \mathrm{K}$. However, it is unlikely that the heating effect reaches this limit, since only a fraction of the total e-beam power will be absorbed by the paddle and generate heat.

Similarly, for 1 fA beam current, operating at 300 mK, $\Delta T_{\max} \sim 3\ \mathrm{mK}$. Again, the actual effect would depend on the fraction of e-beam power getting dissipated.

Therefore, in order to avoid heating up the paddle to a temperature much higher than that of its environment, proper e-beam current needs to be chosen at the temperature of device operation.

From the examples shown in Fig.5.4, we can see that it appears possible to achieve ~250 $\mathrm{zN}/\sqrt{\mathrm{Hz}}$ force sensitivity at room temperature with e-beam current of 1 pA, and acceleration voltage of 1 kV.

Acknowledgements: *This work was generously supported by DARPA MTO/MEMS and NSF.*

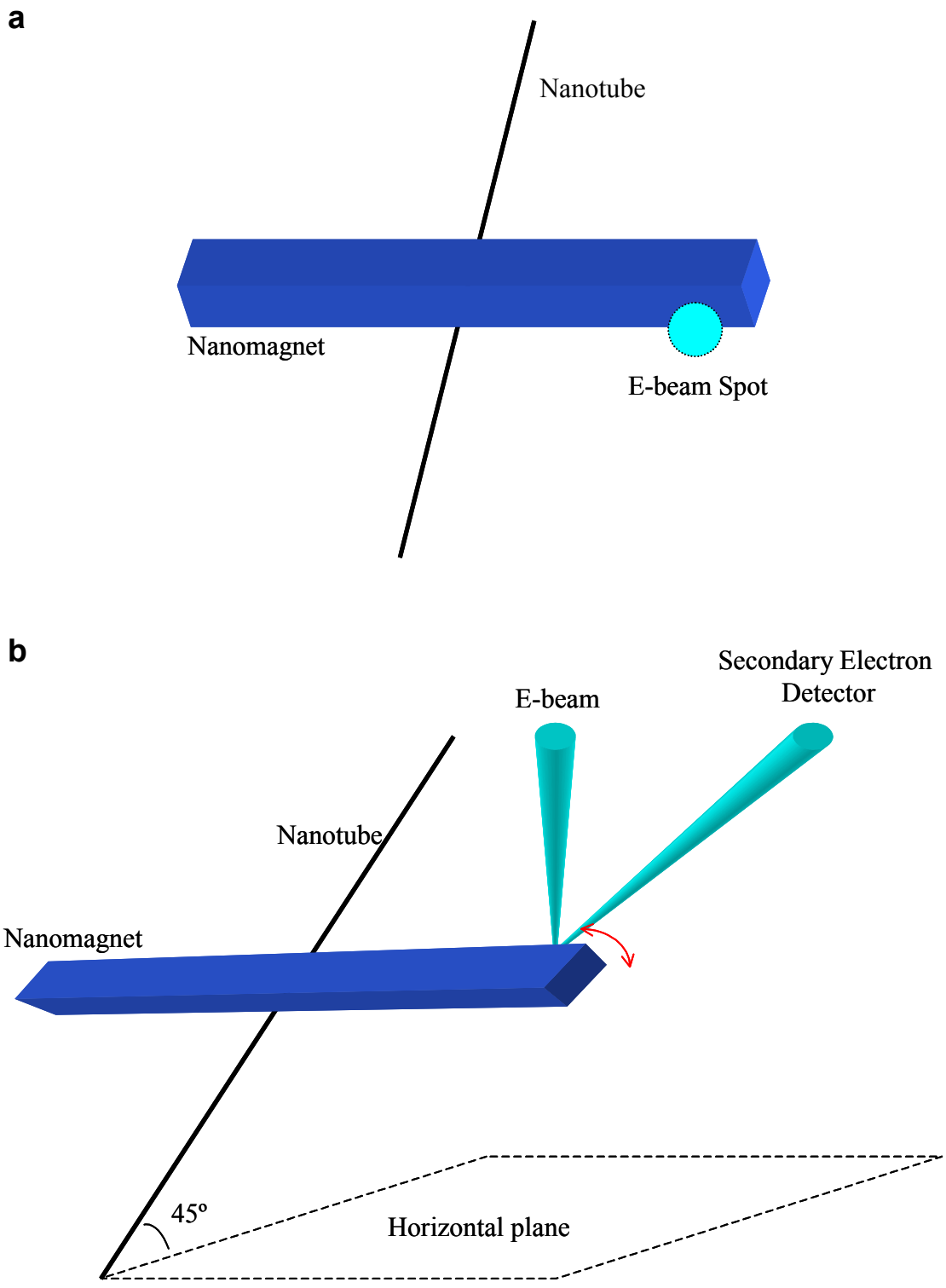

Figure 5.3 Measurement setup. **a,** Approximate top view. **b,** Side view.

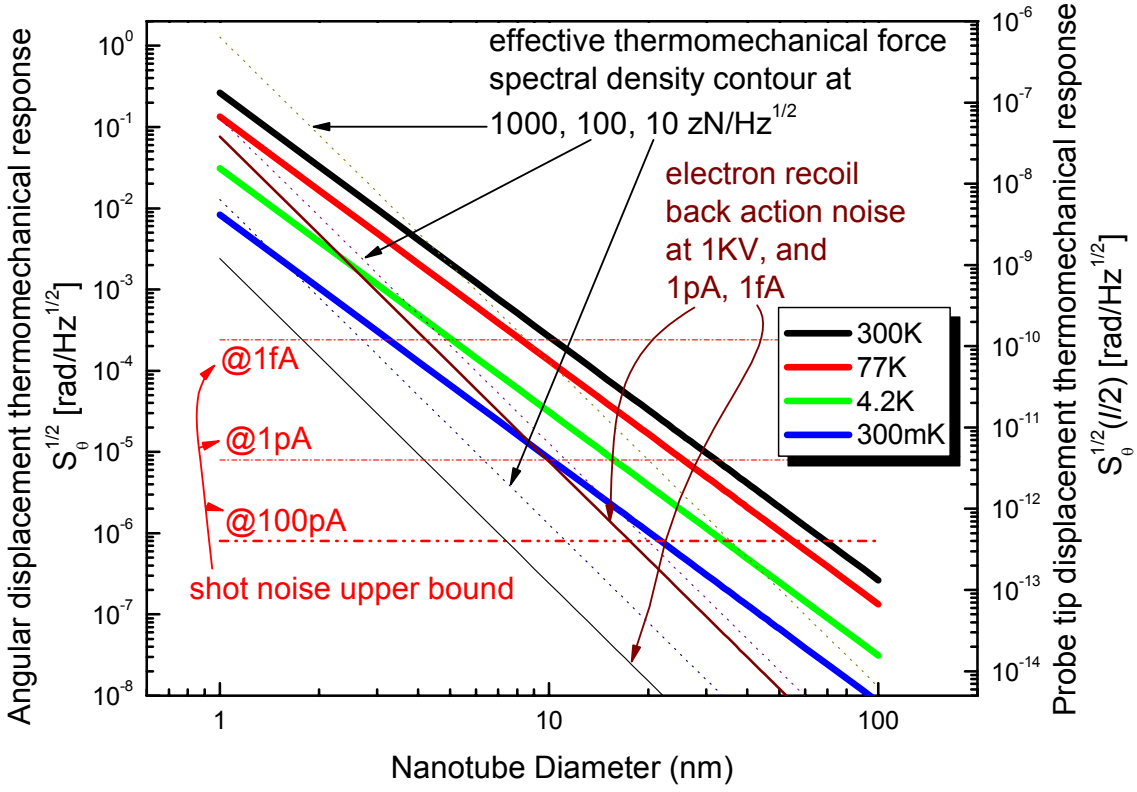

Figure 5.4 Calculated angular displacement thermomechanical response at different temperatures (thick solid lines). It was assumed that the paddle geometry is $l = 1\,\mu\text{m}$, $w = 100$ nm, $t = 50$ nm; the total length of the nanotube section is $L = 1\,\mu\text{m}$; the quality factor of the resonator device is $Q \sim 10^5$. The measurement detects the linear displacement at the probe end of the paddle. The probe tip displacement spectral density is shown on the right-hand-side axis. The dotted lines are effective force sensitivity contours, which defines the trajectory with the same thermomechanical force spectral density, at different values of 10, 100, 1000 $\text{zN}/\sqrt{\text{Hz}}$. The area below $1000\,\text{zN}/\sqrt{\text{Hz}}$ line is the area that the resonator has sub-attonewton effective force sensitivity. Also plotted are the electron recoil back action noise floors for 1 kV e-beam acceleration voltage, and 1 pA, 1 fA beam current, respectively (thin solid lines). The upper bounds of electron shot noise induced fluctuations in displacement readout are plotted for e-beam currents of 100 pA, 1 pA and 1 fA, respectively (slash-dotted lines).

References

1. Sidles, J. A., Garbini, J. L., Bruland, K. J., Rugar, D., Zuger, O., Hoen, S. & Yannoni, C. S. Magnetic-resonance force microscopy. *Rev. Mod. Phys.* **67**, 249-265 (1995).

2. Monzon, F. G., Patterson, D. S. & Roukes, M. L. Characterization of individual nanomagnets by the local Hall effect. *J. Magn. and Magn. Mater.* **195**, 19-25 (1999).

3. Rugar, D., Yannoni, C. S. & Sidles, J. A. Mechanical detection of magnetic-resonance. *Nature* **360**, 563-566 (1992).

4. Rugar, D. et al. Force detection of nuclear-magnetic-resonance. *Science* **264**, 1560-1563 (1994).

5. Hammel, P. C., Zhang, Z., Moore, G. J. & Roukes, M. L. Subsurface imaging with the magnetic-resonance force microscope. *J. Low Temp. Phys.* **101**, 59-69 (1995).

6. Mamin, H. J. & Rugar, D. Sub-attonewton force detection at millikelvin temperatures. *Appl. Phys. Lett.* **79**, 3358-3360 (2001).

7. Saito, R., Dresselhaus, G. & Dresselhaus, M. S. *Physical Properties of Carbon Nanotubes* (Imperial College Press, Singapore, 2001).

8. Poncharal, P., Wang, Z. L., Ugarte, D. & de Heer, W. A. Electrostatic deflections and electromechanical resonances of carbon nanotubes. *Science* **283**, 1513-1516 (1999).

9. Fennimore, A. M. et al. Rotational actuators based on carbon nanotubes. *Nature* **424**, 408-410 (2003).

10. Den Hartog, J. P. *Mechanical Vibrations* (Dover Publications, Inc., New York, 1985).

11. Midzor, M. M. et al. Imaging mechanisms of force detected FMR microscopy. *J. Appl. Phys.* **87**, 6493-6495 (2000).

12. Hammel, P. C. et al. The magnetic-resonance force microscope: a new tool for high- resolution, 3-D, subsurface scanned probe imaging. *Proc. IEEE* **91**, 789-798 (2003).

13. Buks, E. & Roukes, M. L. Stiction, adhesion energy, and the Casimir effect in micromechanical systems. *Phys. Rev. B* **6303**, art. no.-033402 (2001).

14. Buks, E. & Roukes, M. L. Electrically tunable collective response in a coupled micromechanical array. *J. Microelectromech. Systems* **11**, 802-807 (2002).

15. Rugar, D. & Grutter, P. Mechanical parametric amplification and thermomechanical noise squeezing. *Phys. Rev. Lett.* **67**, 699-702 (1991).

16. Hone, J., Batlogg, B., Benes, Z., Johnson, A. T. & Fischer, J. E. Quantized phonon spectrum of single-wall carbon nanotubes. *Science* **289**, 1730-1733 (2000).

17. Hone, J. et al. Thermal properties of carbon nanotubes and nanotube-based materials. *Appl. Phys. A-Materials Science & Processing* **74**, 339-343 (2002).

PART III

QUANTUM ELECTRO MECHANICS

Chapter 6

Quantum Jumps in Nanomechanics: Issues of Principle and Prototype Devices

A structure designed to enable observation of quantum jumps in nanomechanical devices is described. A prototype device demonstrating a frequency shift transduction scheme is fabricated and tested in the classical domain. The coupling mechanism involved is analogous to Kerr nonlinearity in quantum optics. This nanomechanical approach should allow quantum nondemolition (QND) measurements if the experimental technique is extended into the quantum regime. Based on quantum simulations and experimental analysis, we argue that single quanta sensitivity can be achieved in next-generation devices of this kind.

6.1 Introduction

Quantum Mechanics has achieved tremendous success since its birth over a hundred years ago. However, except in a few systems, direct observation of mechanical quanta remains a great experimental challenge even today. Physicists in the field of gravitational wave detection have been actively seeking ways to make quantum nondemolition (QND) measurements at, and beyond, the standard quantum limit for more than 20 years[1-5]. More recently, with the rapid development of the emerging field of nanomechanics[6,7], notably the demonstration of nanomechanical resonators operating at microwave frequencies[8], great interest has been generated to explore the possibility of seeing single mechanical quanta in nanoelectromechanical systems[9-12]. Technologically, nanomechanical sensors with single quanta sensitivity can be used for single spin detection[13], which could, in turn, pave the way towards imaging of single molecules with atomic resolution[14].

6.2 Standard Quantum Limit and Quantum Nondemolition Measurement

In quantum mechanics, the uncertainty principle dictates that position and momentum can not be measured simultaneously with arbitrarily high precision. The best can be done by observing both of the conjugate observables at the same time, defines the standard quantum limit (SQL). For example, the standard quantum limit for a measurement of harmonic oscillator position can be expressed as

$$\Delta x = \sqrt{\frac{\hbar}{2m\omega_0}}\ , \tag{6.1}$$

where $2\pi\hbar$ is Planck's constant, m is the effective mass of the simple harmonic oscillator, $\omega_0 / 2\pi$ is the frequency of the resonator.

For a system in an eigenstate of certain observables, if we use an instrument to measure such an observable, but not its conjugate, the system will remain in the same eigenstate after repeated observation. The uncertainty for the measured observable then can be smaller than the corresponding standard quantum limit. Such kind of measurement is quantum nondemolition (QND) measurement.

A full discussion about the concepts of SQL and QND measurement is out of the scope of this thesis, such information can be found in specialized review articles available in the literature[1,4].

6.3 Device Proposal

Milburn and Walls have analysed a QND measurement scheme using four-wave-mixing interaction[15]. The interaction Hamiltonian involved is identical to that of the optical Kerr effect, with which QND measurement has been achieved in the field of quantum optics[16,17]. More recently, QND measurements with single optical photons[18] and single microwave photons[19] are also realized. Despite the success with electromagnetic wave and particles, it seems, little attention has been paid to possible physical realizations for measuring the mechanical phonon numbers, even though the original QND measurement proposals[1,2] were targeted at mechanical phonons.

Here, we consider a structure schematically shown in Fig. 6.1a, which supports similar interaction Hamiltonian, and thus may be used to realize a phonon number measurement in NEMS. There are two resonator beams, indicated as the signal resonator

and the probe resonator. They are coupled through a coupling junction in between. We take their fundamental resonance mode in the wafer plane as the modes of interest. The motion from the signal mode generates tension along the length of the signal resonator beam. Such tension is used to tune the resonant frequency of the detection mode.

The interaction between the signal and probe beams through the coupling junction has been modelled, by Santamore[20], to have the dominant coupling term $x_a^2 \cdot x_b^2$, since this is the leading order anharmonic coupling term[21].

Taking this interaction term into the quantum regime, the Hamiltonian becomes

$$H_I = \hbar\lambda(a^\dagger + a)^2(b^\dagger + b)^2 \ , \tag{6.2}$$

Under the approximation that the measurement time is much shorter than the coherence time, but much longer than single motional cycle, most terms would vanish if averaged over the measurement time, and the remaining term would be

$$H_I' = \hbar\lambda a^\dagger a b^\dagger b \ , \tag{6.3}$$

After making this approximation, the interaction has the form of Hamiltonian that is identical to that of Kerr nonlinearity. What's essential for nanomechanical systems is that the thermomechnical noise process is not negligible, since the mechanical Fock state spacing $\hbar\omega_0$ is usually smaller than thermal fluctuation energy $k_B T$ for experimentally accessible mechanical systems. On the other hand, the demonstration of the first microwave frequency NEMS resonator device[8] with fundamental mode resonance frequency above 1 GHz has made it plausible to have a thermal occupation number, defined as

$$n_T \equiv \frac{k_B T}{\hbar\omega_0} \ , \tag{6.4}$$

to be smaller than unity. For example, for a 1 GHz nanomechanical resonator, cooled down to 50 mK, n_T equals unity. It is plausible to make nanomechanical resonators with fundamental mode resonance frequency to be 2 or 3 GHz. It is also possible to get to a temperature below 50 mK, with a dilution refrigerator. Therefore, we should be able to access a regime, in future, where the thermal fluctuation is smaller than the Fock state energy level spacing, in the harmonic oscillator approximation.

Our approach in this chapter is to demonstrate experimentally the possibility of realizing an x^2 coupling mechanism in the classical domain.

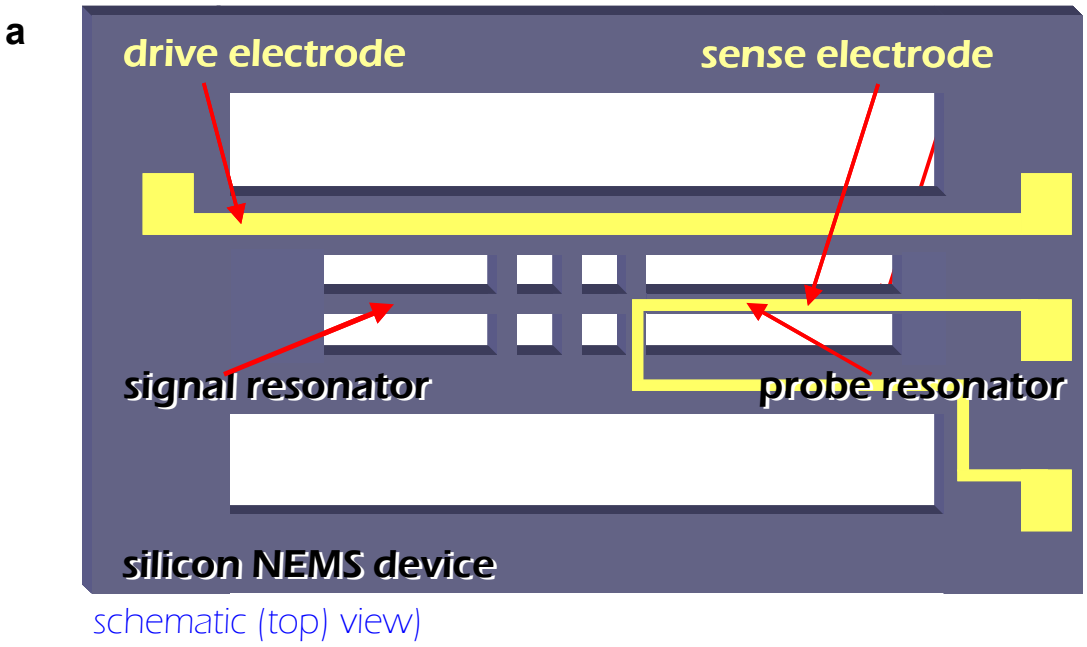

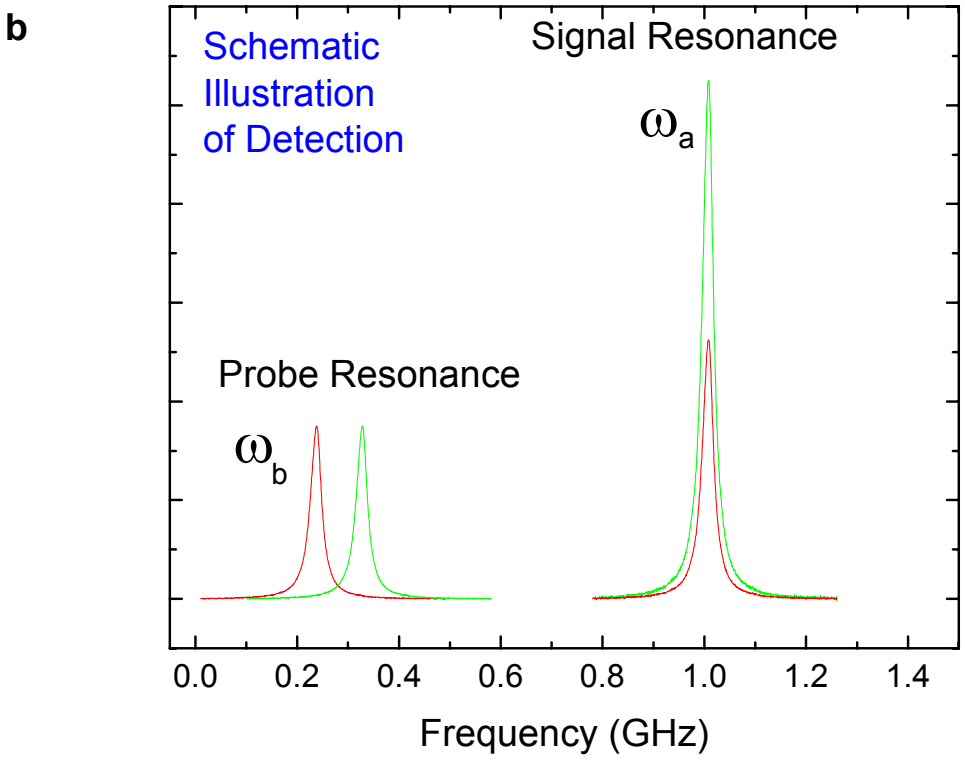

Figure 6.1 Device and Measurement schematics. **a,** Schematic drawing of proposed device structure. **b,** Schematic illustration of measurement principle.

6.4 Experimental Details

6.4.1 Prototype Device Fabrication

Device fabrication[8,22] starts from a monocrystalline 3C-SiC thin film on top of Si substrate. Standard photolithography and e-beam lithography procedures are used to define contact pads and device patterns, respectively. These patterns are then transferred to metallic masks by liftoff processes. A two-step ECR etch involving Ar, O_2, and NF_3 plasma is used to etch away SiC not covered by metal, and then suspend the nanostructure. The first step operates at 3 mTorr of chamber pressure, with 10 sccm flow rate for both Ar and NF_3, 5 sccm for O_2. Also, a DC bias of –250 V is applied on the sample. As a result, SiC is etched anisotropically. The direction of the etch is perpendicular to the wafer surface. The etch rate is on the order of 100 nm/min, depending on the exact location of the sample in the plasma. The second step is also carried out at a chamber pressure of 3 mTorr, with flow rate of 20 sccm for both Ar and NF_3 gases. DC bias on the sample is –100 V. This step gets Si etched isotropically. Here, the Si serves as the sacrificial layer that ultimately enables suspension of the mechanically functional nanostructure. The etch rate for Si is about 1 μm/min. By comparison, the etch rate for metals in both steps is on the order of 1 nm/min or less (for essentially all metal we use, including Cr, Au, Ag, Pt, Al, Ni, Ti).

SEM micrographs of a completed device are shown in Fig. 6.2. The width of the fine features is 0.2 μm, which contains 40 nm Au atop 2 nm Cr (for cohesion) as metallic layer on top of 75 nm SiC.

From these photos, we can see that the resonator beams and the coupling junction structure are completely undercut. The large finger pads and the small support structure are partially undercut, but still sufficiently anchored to the silicon substrate.

6.4.2 Device Testing Setup

The schematic circuit diagram for device testing is shown in Fig. 6.3. Instrument "a" and "b" physically can be either a network analyser, e.g., model HP3577A, or an rf signal generator (HP8648B) coupled with an rf lock-in amplifier (SR844). Both configurations give similar results. Instrument "a" operates around the fundamental resonance frequency of resonator "a", while Instrument "b" operates around that of resonator "b".

Joule-heating effect from the currents needs to be considered. Here, we use the input power level required to shift the resonance by half peak width to define the onset of this effect. In this work, we have experimentally determined that it is necessary to have an input power of about 30 nW to reach such onset for the signal mode resonance. The power levels we used in our measurements are at least an order of magnitude lower.

This measurement circuit incorporates the essence of the balanced electronic detection developed recently by Ekinci et al.[23]. All driving signals first pass through a 180° power splitter, and then are sent through electrodes from the clamped ends of the two resonators. The common end of the two resonators, i.e., the central pad at the coupling junction, is used as the device output port. In this circuit, effects from the parasitic components of the two circuit branches can be minimized when the two branches of the circuit are closely matched in terms of attenuation and phase shift.

Fig. 6.3 shows the basic circuit for this measurement. Additional components can be added to optimise the performance, including additional attenuator and phase shifter to help improve the balancing between the two circuit branches for driving, and impedance matching networks at each port.

For this experiment, we found that, as-fabricated, the sample had the proper resistance values at 4.2 K, so that the output impedance at the detection port was initially reasonably well-matched to 50 Ω, i.e., to within a few percent.

6.4.3 Test Results and Discussions

The characterization of the signal mode by instrument "a" is shown in Fig. 6.4. The top figure shows the B field dependence of resonance. By fitting to Lorentzian curve, we can determine the signal mode resonance quality factor is about 11,400.

In the design of this prototype device, the large aspect ratio of the signal resonator beam helps to provide its high Q. In this kind of beam resonator, using magnetomotive transduction, two dissipation mechanisms are important, the clamping loss[24] and the eddy current damping[25] (see also, Chapter 4 of this thesis). And they compete with each other.

The inset in Fig. 6.4a shows maximum amplitude of the resonance depends linearly on B^2, as expected for this magnetomotive transduction scheme of mechanical motion[25-27]. Fig. 6.4b shows the driving amplitude dependence of the resonance, so as to keep track when our experiment is addressing the linear regime for the signal resonator mechanical resonance.

The signal mode resonance frequency shifts downward slightly as the driving power goes up. This is due to Joule heating effect at high driving power. However, for

the purpose of this experiment, we are more interested in the low amplitude regime, approaching the quantum noise limit.

From the QND measurement point of view, the detection scheme is an attempt to read out the energy excitation of the signal mode. This excitation manifests itself as a phase shift in the detection mode.

Fig. 6.5 shows the amplitude and phase of the detection mode resonance. When the drive to the signal mode is turned off, the resonance of the detection resonator is shown by the black traces. These are measured under the condition that the motion of the signal resonator is at the thermomechanical noise limit, which can be estimated by

$$S_x^{1/2} = \sqrt{\frac{4k_B TQ}{2\pi f_a k_{eff}}} \ , \tag{6.5}$$

where k_{eff} is the effective spring constant of the signal beam. For the signal resonator used in this prototype experiment, this is calculated to be on the order of $4\,\mathrm{fm}/\sqrt{\mathrm{Hz}}$. In the example shown in Fig. 6.5, the drive applied to the signal resonator results in a resonance amplitude of about 0.36 nm; this motion, in turn, results in a phase shift of the detection mode resonance of 30.2 degrees. The minimum detectable amplitude of signal resonator motion is estimated to be about 10 pm based on the measured noise floor of this experiment.

To characterize this detection method, the amplitude of motion for the signal resonator is varied stepwise while the resulting phase shift of the detection mode is recorded. The result is plotted in Fig. 6.6. We note that the result from Fig. 6.5 gives one of the points in Fig. 6.6. As the signal mode resonance amplitude is decreased, the noise floor of this detection method is approached; in this initial work it is dominated by the

first stage amplifier noise. The amplifier noise floor ($\sim 1\,\mathrm{nV}/\sqrt{\mathrm{Hz}}$) translates into the minimum phase shift, which in turn corresponds to a minimum detectable energy of the signal mode resonance. Here the minimum energy is $\sim 10^6$ quanta under the condition of this experiment for this particular device. On the other hand, the signal beam's thermomechanical noise floor is on the order of 10^3 quanta as calculated from thermal occupation number $k_B T / \hbar\omega_a$ for signal resonator.

It is important to note that, based on quantum measurement theory[28], the thermal occupation number does not need to be smaller than 1 in order to see quantum behaviour in the system. As pointed out by Braginsky et al.[29], as long as the measurement time is shorter than the quantum coherence time, quantum measurement is achievable in principle even if $k_B T$ is larger than $\hbar\omega_0$. The quantum coherence time issue in devices of this kind is very important, which requires much further investigation (beyond this thesis).

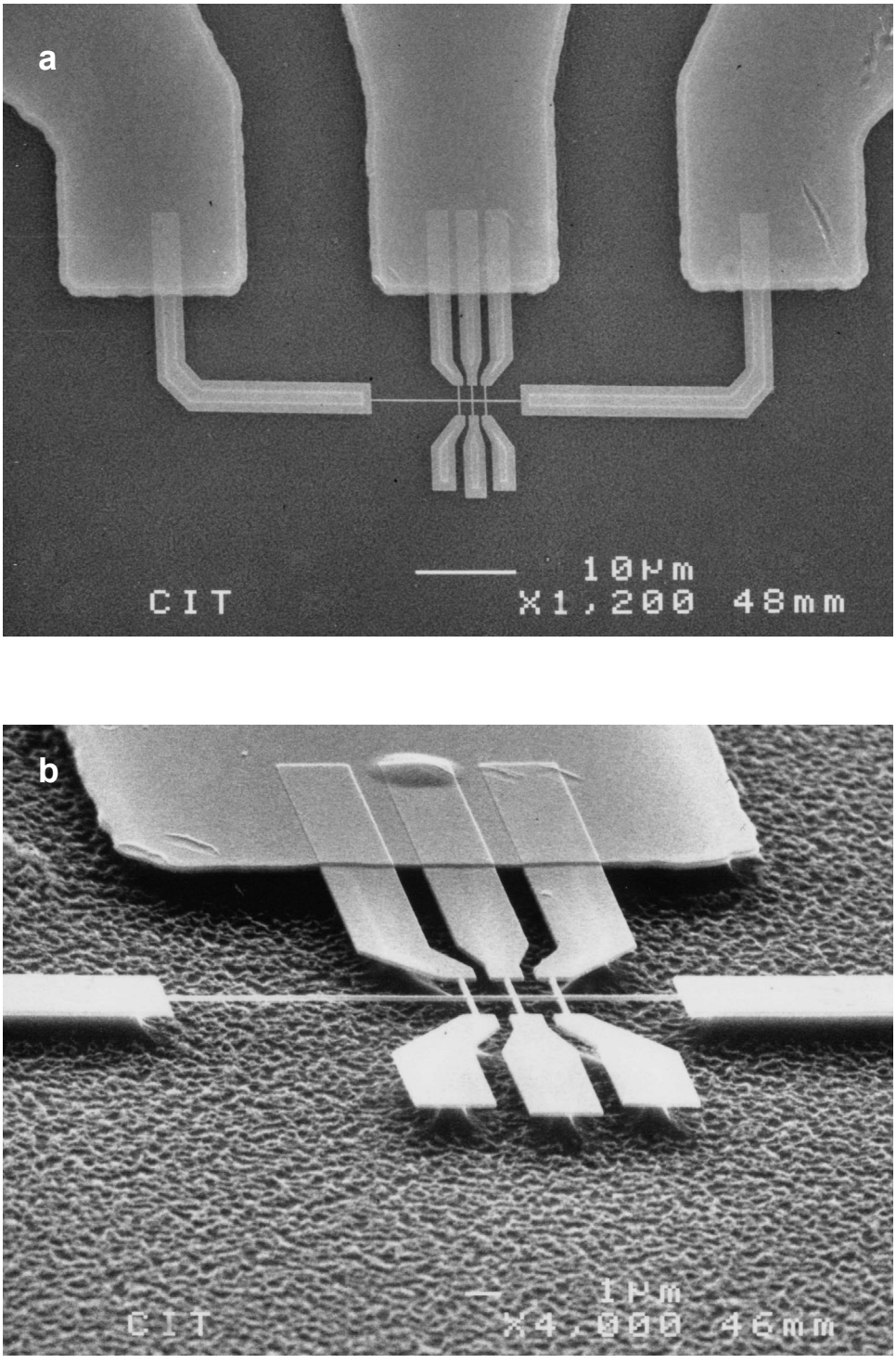

Figure 6.2 Device SEM photos. **a,** Top view. **b,** Side view.

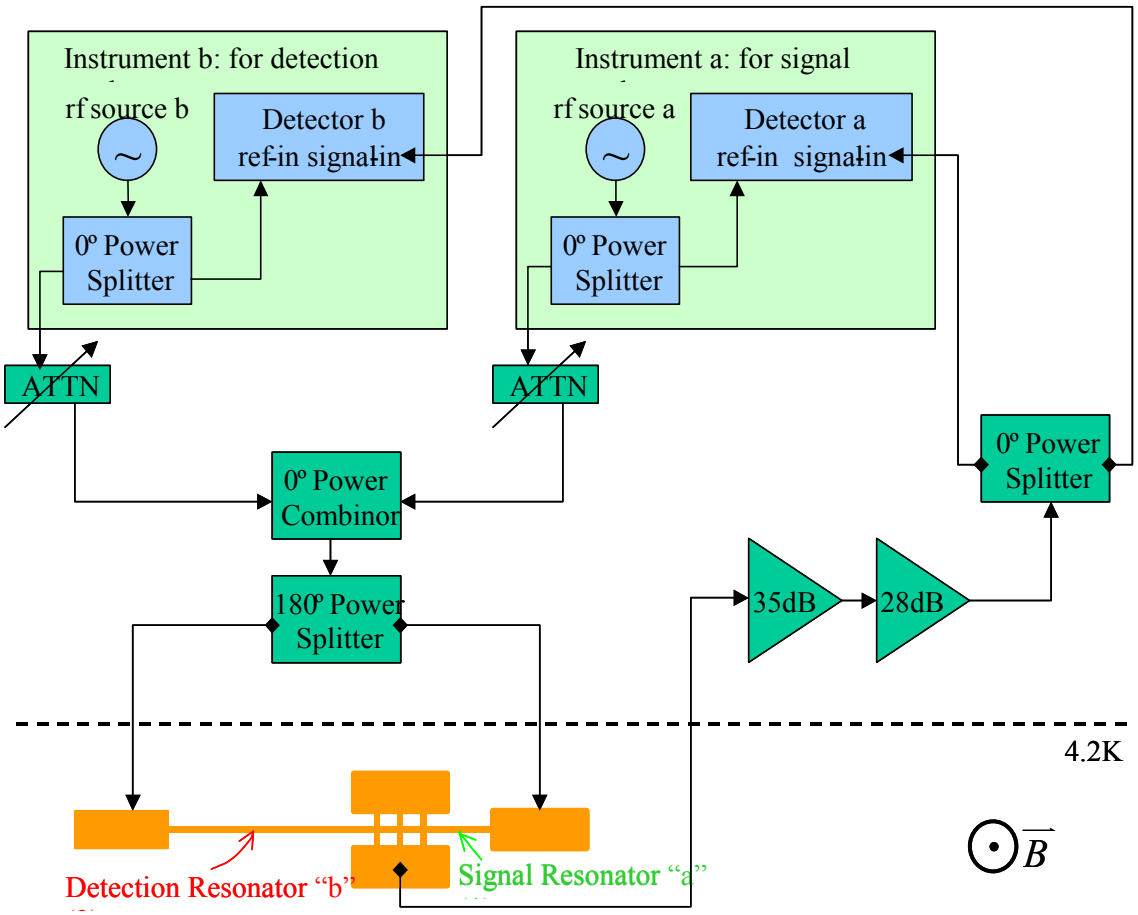

Figure 6.3 Measurement circuit diagram. Instrument "a" and "b" can either be a network analyzer, e.g., model HP3577A, or an rf signal generator (HP8648B) connected to an rf lock-in (SR844).

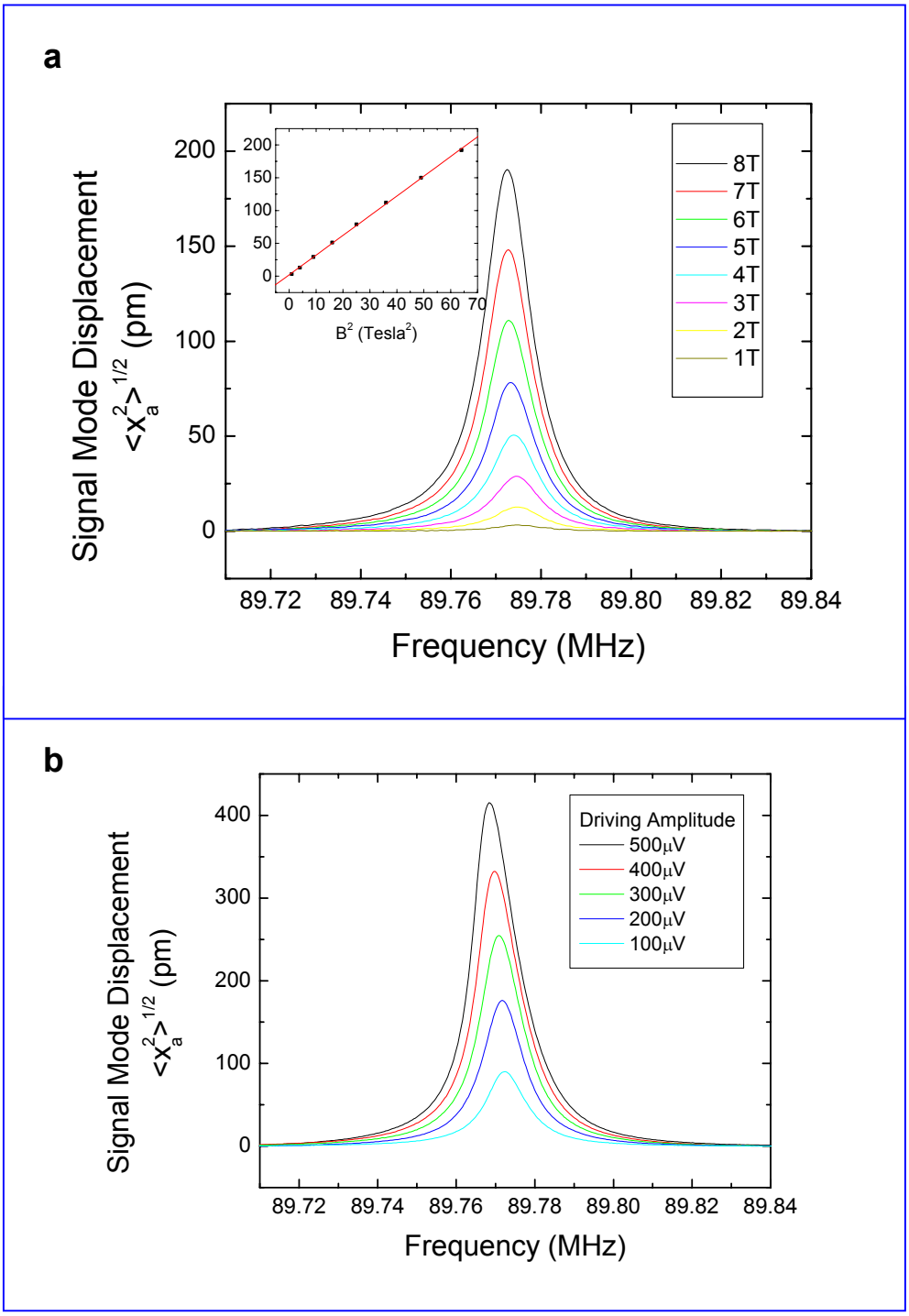

Figure 6.4 Signal mode characterization. **a,** Resonance traces at different B field. **b,** Resonance traces at different driving amplitude. This enables us to choose the driving amplitude, so as to insure operation within the linear regime of the signal resonator.

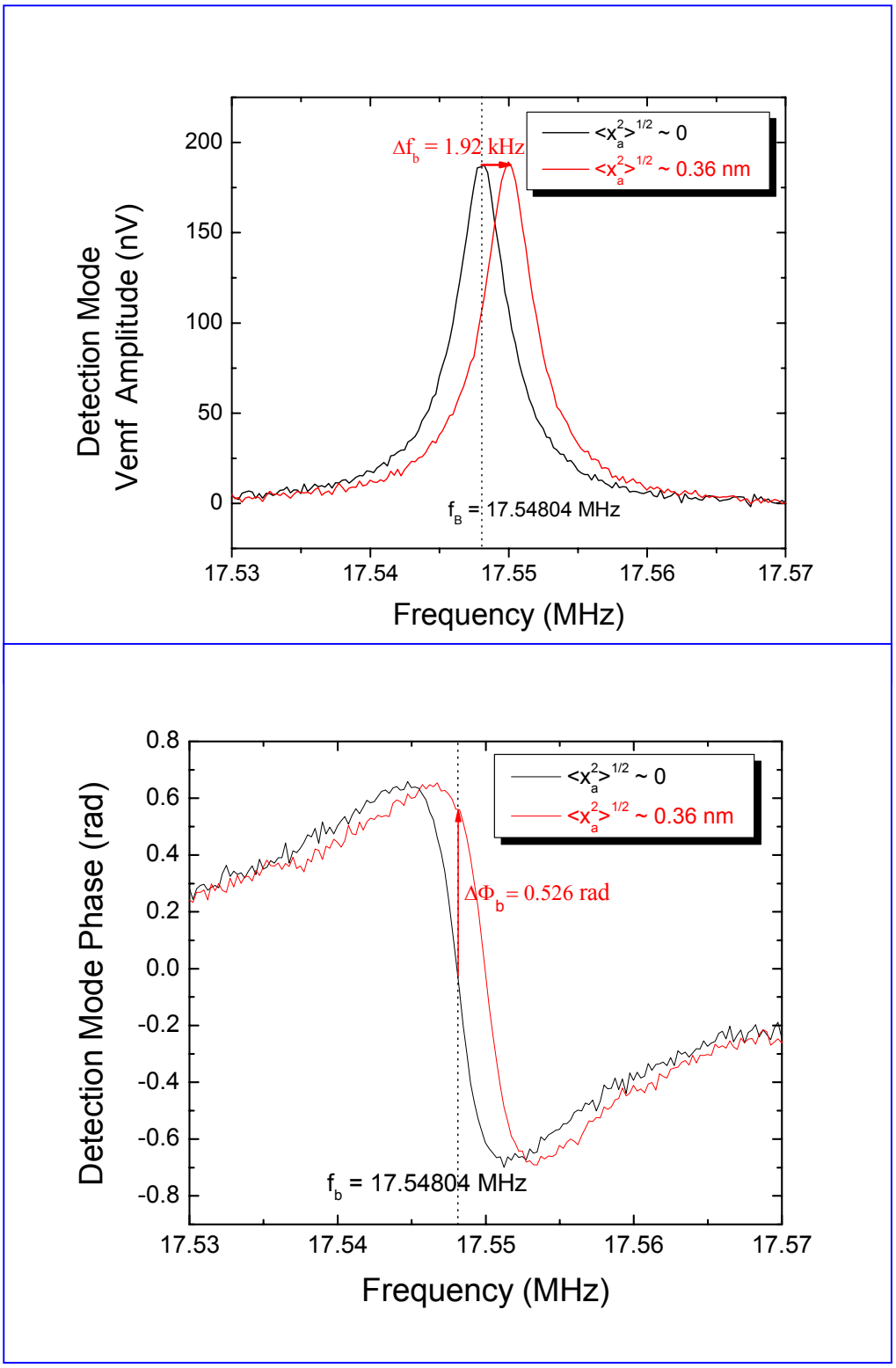

Figure 6.5 Detection mode frequency/phase shift due to signal mode motion.

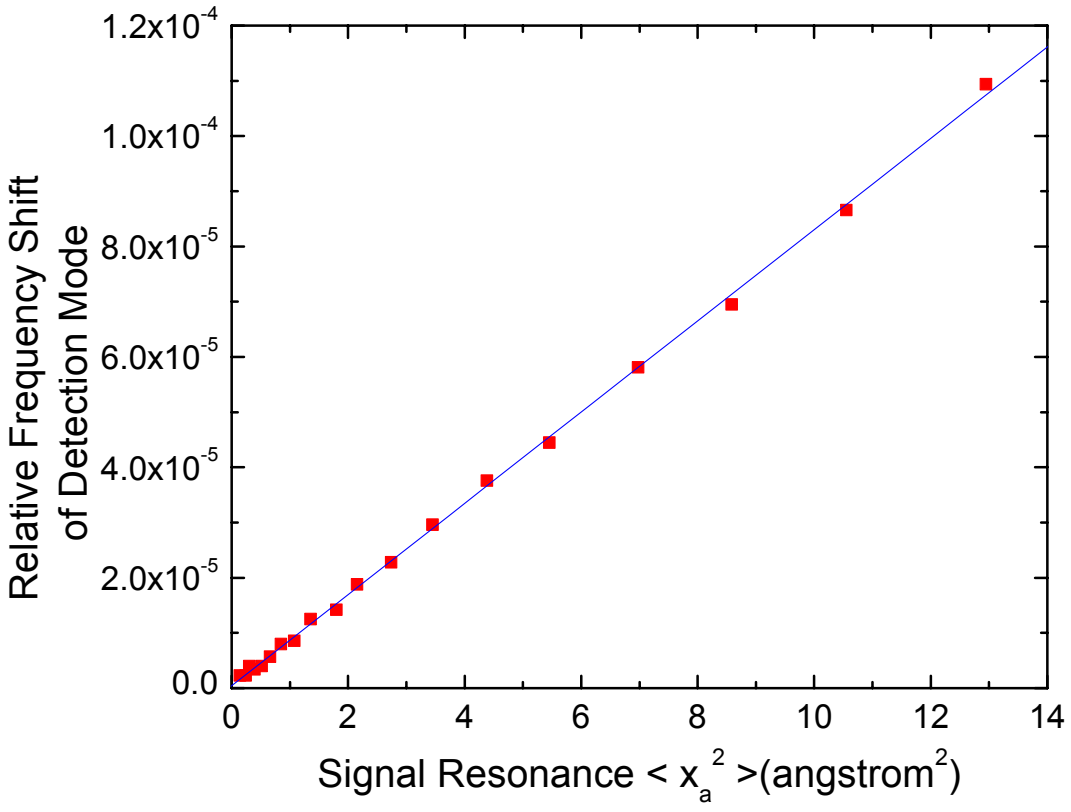

Figure 6.6 Primary result: $\langle x^2 \rangle$ coupling. The sensitivity of these experiments is limited by readout amplifier noise, which corresponds to ~10^6 signal-mode quanta in this particular case.

6.5 Quantum Dynamics Modelling and Simulations

6.5.1 Theoretical Model

The device contains two mesoscopic elastic beams with rectangular cross-section, connected by a junction that couples the flexing motion of signal beam (system) to the flexing modes of the detection beam (ancilla) anharmonically. Our interest is quantum jumps occurring in the system, i.e., the time evolution of $< a^{\dagger} a(t) >$.

All thermal baths (environment) are modeled as infinite numbers of harmonic oscillators, however, the physics of the environment couplings to the system and that to the ancilla are quite different. For the system, the environment coupling is due to non-zero temperature thermal bath whilst for the driven ancilla, it is mainly thermal noise generated by the flexing motion of the beam. Nevertheless the mathematical structures of the bath's Hamiltonian are very similar and differ only by coeffcients. Two thermal baths are linearly coupled (coordinate-coordinate coupling, or *x*-coupling) to the system and ancilla. For the readout coupling, the coupling between the ancilla and read-out is also x-coupling since the displacement of the ancilla's flexural mode is monitored by the read-out (a physical instrument).

6.5.2 Summary of Simulation Results

The quantum dynamics simulations have been carried out by our theoretical collaborator, D. H. Santamore, as part of her Ph.D. research. Detailed simulation results as well as in-depth discussions about the theoretical principle can be found in her thesis[20].

Briefly, the trajectory can be obtained by quantum state diffusion method[30] to get stochastic motion of an individual quantum system in a possible single run of experiment. Discreteness in $< a^{\dagger} a(t) >$ following one trajectory can be seen, with proper choice of parameters. The jumps become more pronounced as one increases the measurement strength relative to the thermal coupling. Over a long period of time, the state settles down to a given number state in the limit that there is no thermal coupling.

6.6 Next Generation Device Design

When the device used in this experiment is cooled down to 100 mK, which is accessible through the use of a dilution refrigerator, the thermal occupation number, defined as $k_B T / \hbar \omega_0$, for the signal resonator is about 20. This can be even smaller by increasing the frequency of the signal resonator. So far, it has been demonstrated that resonators of this kind can go beyond 1 GHz.[8] It is also quite plausible to go to 3 GHz, so as to access a regime of $k_B T / \hbar \omega_0 < 1$ at 100 mK.

Another fabrication parameter that needs to be tuned is the width of the beams. Reducing the width and length at the same time, but keeping the resonance frequency unchanged, will give a larger aspect ratio, smaller spring constant in the design, thus better responsivity. The feature size of the 1GHz resonator achieved so far still have a feature size slightly over 100 nm. It is certainly within our fabrication capability to reduce the width of the beam to few nanometers, either by state-of-the-art top-down e-beam lithography, or by bottom-up nanowire imprinting[31].

In order to approach single quanta sensitivity, we'll need to optimise the device geometry for both the signal resonator and the probe resonator.

For signal resonator, maintaining the same signal resonance frequency, but shrinking the signal resonator to smaller feature sizes would allow us to use larger aspect ratio resonator beams. Such beams has smaller mass, smaller spring constant and thus better responsivity, namely, the quantum fluctuations become larger.

For probe resonator, based on the principle of frequency tuning by applying tensile stress[32], we know that

$$\frac{\Delta f_b}{f_b} \propto \left\langle \Delta x_a^2 \right\rangle \cdot \left(\frac{l_b}{t_b} \right)^2 , \tag{6.6}$$

thus a certain level of detection sensitivity in $\frac{\Delta f_b}{f_b}$ would correspond to a smaller $\left\langle \Delta x_a{}^2 \right\rangle$, for a probe beam with larger aspect ratio. A specific example of future device geometry is analysed, and listed in Table 6.1 to compare with the prototype device used in this experiment.

Through this comparison, we can see that, by improving various aspects of the readout architecture, single quanta sensitivity may be attainable.

		This Experiment	Next Generation Device
Experimental Condition	T	4.2 K	100 mK
Device Geometry	w	200 nm	10 nm
	t	140 nm	10 nm
	l_a	4 μm	1 μm
	l_b	9 μm	9 μm
SQL for position	$\left\langle x_{SQL}^2 \right\rangle^{1/2}$	15 fm	0.5 pm
Detection Sensitivity	$\left.\frac{\Delta f_b}{f_b}\right\|_{\min}$	2.5×10^{-6}	
	Corresponding $< x_a^2 >^{1/2}$	10 pm	0.5 pm
	Corresponding number of quanta	5×10^5	~ 1

Table 6.1 Comparison between this experiment on the prototype device and a future experiment based on a next generation scaled-down device design. By improving various aspects of the readout architecture, single quanta sensitivity may be attainable.

6.7 Quantum Instrumentation

This chapter has analysed one of the possible schemes to get to quantum measurement in mechanics. Other approaches are possible. The Cleland group at UCSB has recently demonstrated an SET-based displacement sensor which is about a factor of 100 away from the standard quantum limit[11]. Also, Cooper pair box based displacement sensing is being analysed and attempted, led by Schwab's group at NSA and University of Maryland[9]. The field of *Quantum Electro Mechanics* is only at its beginning. It remains to be explored how different amplifier designs, such as SQUID based rf-amplifiers[33], mechanical parametric amplifiers[34,35], may help researchers in the endeavour for putting quantum into mechanics[10].

6.8 Conclusions

The scheme described here may be capable of resolving quantum jumps in nanomechanical systems. Interesting applications may become possible with this kind of device, such as potential single spin detector. Systematic studies and prototyping will pave the way towards realizing such tantalizing applications promised by future forms of such devices.

Acknowledgements: *We thank DARPA and NSF for financial support.*

References

1. Caves, C. M., Thorne, K. S., Drever, R. W. P., Sandberg, V. D. & Zimmermann, M. On the measurement of a weak classical force coupled to a quantum-mechanical oscillator .1. Issues of principle. *Rev. Mod. Phys.* **52**, 341-392 (1980).

2. Braginsky, V. B., Vorontsov, Y. I. & Thorne, K. S. Quantum non-demolition measurements. *Science* **209**, 547-557 (1980).

3. Braginsky, V. B. & Khalili, F. Y. Quantum nondemolition measurements: The route from toys to tools. *Rev. Mod. Phys.* **68**, 1-11 (1996).

4. Bocko, M. F. & Onofrio, R. On the measurement of a weak classical force coupled to a harmonic oscillator: experimental progress. *Rev. Mod. Phys.* **68**, 755-799 (1996).

5. Mabuchi, H. Standard quantum limits for broadband position measurement. *Physical Review A* **58**, 123-127 (1998).

6. Roukes, M. L. Nanoelectromechanical systems face the future. *Phys. World* **14**, 25-31 (2001).

7. Roukes, M. L. Plenty of room indeed. *Sci. Am.* **285**, 48-57 (2001).

8. Huang, X. M. H., Zorman, C. A., Mehregany, M. & Roukes, M. L. Nanodevice motion at microwave frequencies. *Nature* **421**, 496 (2003).

9. Armour, A. D., Blencowe, M. P. & Schwab, K. C. Entanglement and decoherence of a micromechanical resonator via coupling to a Cooper-pair box. *Phys. Rev. Lett.* **88**, 148301 (2002).

10. Cho, A. Physics - Researchers race to put the quantum into mechanics. *Science* **299**, 36-37 (2003).

11. Knobel, R. G. & Cleland, A. N. Nanometre-scale displacement sensing using a single electron transistor. *Nature* **424**, 291-293 (2003).

12. Schwab, K. & colleagues. *Science, accepted* (2004).

13. Stipe, B. C. et al. Electron spin relaxation near a micron-size ferromagnet. *Phys. Rev. Lett.* **87**, 277602 (2001).

14. Sidles, J. A., Garbini, J. L., Bruland, K. J., Rugar, D., Zuger, O., Hoen, S. & Yannoni, C. S. Magnetic-resonance force microscopy. *Rev. Mod. Phys.* **67**, 249-265 (1995).

15. Milburn, G. J. & Walls, D. F. Quantum nondemolition measurements via quadratic coupling. *Phys. Rev. A* **28**, 2065-2070 (1983).

16. Imoto, N., Haus, H. A. & Yamamoto, Y. Quantum nondemolition measurement of the photon number via the optical Kerr effect. *Phys. Rev. A* **32**, 2287-2292 (1985).

17. Yamamoto, Y., Machida, S. & Richardson, W. H. Photon number squeezed states in semiconductor-lasers. *Science* **255**, 1219-1224 (1992).

18. Nogues, G. et al. Seeing a single photon without destroying it. *Nature* **400**, 239-242 (1999).

19. Peil, S. & Gabrielse, G. Observing the quantum limit of an electron cyclotron: QND measurements of quantum jumps between Fock states. *Phys. Rev. Lett.* **83**, 1287-1290 (1999).

20. Santamore, D. H. Ph.D. Thesis. (Caltech, 2003).

21. Santamore, D. H., Goan, H.-S., Milburn, G. J. & Cross, M. C. MOSAIC Review Report. (Caltech, Pasadena, 17 October 2002).

22. Yang, Y. T. et al. Monocrystalline silicon carbide nanoelectromechanical systems. *Appl. Phys. Lett.* **78**, 162-164 (2001).

23. Ekinci, K. L., Yang, Y. T., Huang, X. M. H. & Roukes, M. L. Balanced electronic detection of displacement in nanoelectromechanical systems. *Appl. Phys. Lett.* **81**, 2253-2255 (2002).

24. Huang, X. M. H., Zorman, C. A., Mehregany, M. & Roukes, M. L. Quality factor issues in silicon carbide nanomechanical resonators. in *Transducers'03, the 12th International Conference on Solid-State Sensors, Actuators and Microsystems, Boston, MA, USA, June 8-12, 2003,* (ISBN: 0-7803-7732-X), 722-725 (2003).

25. Cleland, A. N. & Roukes, M. L. External control of dissipation in a nanometer-scale radiofrequency mechanical resonator. *Sens. Actuator A-Phys.* **72**, 256-261 (1999).

26. Cleland, A. N. & Roukes, M. L. A nanometre-scale mechanical electrometer. *Nature* **392**, 160-162 (1998).

27. Cleland, A. N. & Roukes, M. L. Fabrication of high frequency nanometer scale mechanical resonators from bulk Si crystals. *Appl. Phys. Lett.* **69**, 2653-2655 (1996).

28. Braginsky, V. B. & Khalili, F. Y. *Quantum Measurement* (ed. Thorne, K. S.) (Cambridge University Press, 1992).

29. Braginsky, V. B., Mitrofanov, V. P. & Panov, V. I. *Systems with Small Dissipation* (eds. Thorne, K. S. & Eller, C.) (The University of Chicago Press, Chicago, 1985).

30. Walls, D. F. & Milburn, G. J. *Quantum Optics* (Springer-Verlag, 1995).

31. Melosh, N. A. et al. Ultrahigh-density nanowire lattices and circuits. *Science* **300**, 112-115 (2003).

32. Harrington, D. A. & Roukes, M. L. Caltech Technical Report CMP-106 (Caltech, Pasadena, 25 December 1994).

33. Muck, M., Kycia, J. B. & Clarke, J. Superconducting quantum interference device as a near-quantum- limited amplifier at 0.5 GHz. *Appl. Phys. Lett.* **78**, 967-969 (2001).

34. Rugar, D. & Grutter, P. Mechanical parametric amplification and thermomechanical noise squeezing. *Phys. Rev. Lett.* **67**, 699-702 (1991).

35. Harrington, D. A. Ph.D. Thesis (Caltech, 2003).

APPENDIX A

ADDITIONAL PROJECTS

Appendix A.1*

Monocrystalline Silicon Carbide Nanoelectromechanical Systems

SiC is an extremely promising material for nanoelectromechanical systems given its large Young's modulus and robust surface properties. We have patterned nanometer scale electromechanical resonators from single-crystal 3C-SiC layers grown epitaxially upon Si substrates. A surface nanomachining process is described that involves electron beam lithography followed by dry anisotropic and selective electron cyclotron resonance plasma etching steps. Measurements on a representative family of the resulting devices demonstrate that, for a given geometry, nanometer-scale SiC resonators are capable of yielding substantially higher frequencies than GaAs and Si resonators.

 [DOI: 10.1063/1.1338959]

* This section has been published as: Y. T. Yang, K. L. Ekinci, X. M. H. Huang, L. M. Schiavone, M. L. Roukes, C. A. Zorman & M. Mehregany, *Appl. Phys. Lett.* **78**, 162-164 (2001).

Silicon carbide is an important semiconductor for high temperature electronics due to its large band gap, high breakdown field, and high thermal conductivity. Its excellent mechanical and chemical properties have also made this material a natural candidate for microsensor and microactuator applications in microelectromechanical systems (MEMS)[1].

Recently, there has been a great deal of interest in the fabrication and measurement of semiconductor devices with fundamental mechanical resonance frequencies reaching into the microwave bands. Among technological applications envisioned for these nanoelectromechanical systems (NEMS) are ultrafast, high-resolution actuators and sensors, and high frequency signal processing components and systems[2]. From the point of view of fundamental science, NEMS also offer intriguing potential for accessing regimes of quantum phenomena and for sensing at the quantum limit.

SiC is an excellent material for high frequency NEMS for two important reasons. First, the ratio of its Young's modulus, *E*, to mass density, ρ, is significantly higher than for other semiconducting materials commonly used for electromechanical devices, e.g., Si and GaAs. Flexural mechanical resonance frequencies for beams directly depend upon the ratio $\sqrt{E/\rho}$. The goal of attaining extremely high fundamental resonance frequencies in NEMS, while simultaneously preserving small force constants necessary for high sensitivity, requires pushing against the ultimate resolution limits of lithography and nanofabrication processes. SiC, given its larger $\sqrt{E/\rho}$, yields devices that operate at significantly higher frequencies for a given geometry, than otherwise possible using conventional materials. Second, SiC possesses excellent chemical stability[3]. This makes

surface treatments an option for higher quality factors (Q factor) of resonance. It has been argued that for NEMS the Q factor is governed by surface defects and depends on the device surface-to-volume ratio[2].

Micron-scale SiC MEMS structures have been fabricated using both bulk and surface micromachining techniques. Bulk micromachined 3C-SiC diaphragms, cantilever beams, and torsional structures have been fabricated directly on Si substrates using a combination of 3C-SiC growth processes and conventional Si bulk micromachining techniques in aqueous KOH[4] and TMAH solutions[5]. Surface micromachined SiC devices have primarily been fabricated from polycrystalline 3C-SiC (poly-SiC) thin films deposited directly onto silicon dioxide sacrificial layers, patterned using reactive ion etching, and released by timed etching in aqueous hydrofluoric acid solutions[6]. Single crystal 3C-SiC surface micromachined structures have been fabricated in a similar way from 3C-SiC-on-SiO2 substrates created using wafer bonding techniques[7]. We have developed an alternative approach for nanometer-scale single crystal, 3C-SiC layers that is not based upon wet chemical etching and/or wafer bonding. Especially noteworthy is that our final suspension step in the surface nanomachining process is performed by using a dry etch process. This avoids potential damage due to surface tension encountered in wet etch processes, and circumvents the need for critical point drying when defining large, mechanically compliant devices. We first describe the method we developed for fabrication of suspended SiC structures, then demonstrate the high frequency performance attained from doubly clamped beams read out using magnetomotive detection.

The starting material for device fabrication is a 259 nm thick single crystalline 3C-SiC film heteroepitaxially grown on a 100 mm diameter (100) Si wafer. 3C-SiC epitaxy is performed in a rf induction-heated reactor using a two-step, carbonization-based atmospheric pressure chemical vapor deposition (APCVD) process detailed elsewhere[8]. Silane and propane are used as process gases and hydrogen is used as the carrier gas. Epitaxial growth is performed at a susceptor temperature of about 1330°C. 3C-SiC films grown using this process have a uniform (100) orientation across each wafer, as indicated by x-ray diffraction. Transmission electron microscopy and selective area diffraction analysis indicates that the films are single crystalline. The microstructure is typical of epitaxial 3C-SiC films grown on Si substrates, with the largest density of defects found near the SiC/Si interface, which decreases with increasing film thickness. A unique property of these films is that the 3C-SiC/Si interface is absent of voids, a characteristic not commonly reported for 3C-SiC films grown by APCVD.

Fabrication begins by defining large area contact pads by optical lithography. A 60 nm thick layer of Cr is then evaporated and, subsequently, standard lift-off is carried out with acetone. Samples are then coated with a bilayer polymethylmethacrylate (PMMA) resist prior to patterning by electron beam lithography. After resist exposure and development, 30–60 nm of Cr is evaporated on the samples, followed by lift-off in acetone. The pattern in the Cr metal mask is then transferred to the 3C-SiC beneath it by anisotropic electron cyclotron resonance (ECR) plasma etching. We use a plasma of NF_3, O_2, and Ar at a pressure of 3 mTorr with respective flow rates of 10, 5, 10 sccm, and a microwave power of 300 W. The acceleration dc bias is 250 V. The etch rate under these conditions is ~65 nm/min.

The vertically etched structures are then released by controlled local etching of the Si substrate using a selective isotropic ECR etch for Si. We use a plasma of NF_3 and Ar at a pressure of 3 mTorr, both flowing at 25 sccm, with a microwave power 300 W, and a dc bias of 100 V. We find that NF_3 and Ar alone do not etch SiC at a noticeable rate under these conditions. The horizontal and vertical etch rates of Si are ~300 nm/min. These consistent etch rates enable us to achieve a significant level of control of the undercut in the clamp area of the structures. The distance between the suspended structure and the substrate can be controlled to within 100 nm.

After the structures are suspended, the Cr etch mask is removed either by ECR etching in an Ar plasma or by a wet Cr photomask etchant (perchloric acid and ceric ammonium nitrate). The chemical stability and the mechanical robustness of the structures allow us to perform subsequent lithographic fabrication steps for the requisite metallization (for magnetomotive transduction) step on the *released* structures. Suspended samples are again coated with bilayer PMMA and after an alignment step, patterned by electron beam lithography to define the desired electrodes. The electrode structures are completed by thermal evaporation of 5 nm thick Cr and 40 nm thick Au films, followed by standard lift-off. Finally, another photolithography step, followed by evaporation of 5 nm Cr and 200 nm Au and conventional lift-off, is performed to define large contact pads for wire bonding. Two examples of completed structures, each containing a family of doubly clamped SiC beams of various aspect ratios, are shown in Fig. A.1.1.

We have measured the fundamental resonance frequencies of both the in-plane and out-of-plane vibrational modes for a family of doubly clamped SiC beams, with

rectangular cross section and different aspect ratios (length/width). Samples were glued into a chip carrier and electrical connections were provided by Al wirebonds. Electromechanical characteristics were measured using the magnetomotive detection technique[9] from 4.2 to 295 K, in a superconducting solenoid within a variable temperature cryostat. The measured fundamental frequencies in this study ranged from 6.8 to 134 MHz. The quality factors, extracted from the fundamental mode resonances for each resonator, range from $10^3<Q<10^4$. Fig. A.1.2 shows the response of one representative beam with dimensions 8 μm (length) × 600 nm (width) × 259 nm (thickness). This particular device yields an in-plane resonant frequency of 71.91 MHz and a $Q \sim 4000$ at 20 K. Quality factors at room temperature were typically a factor of 4-5 smaller than values obtained at low temperature.

We now demonstrate the benefits of SiC for NEMS, by directly comparing frequencies attainable for structures of similar geometry made with SiC, Si, and GaAs. The fundamental resonance frequency, f, of a doubly clamped beam of length, L, and thickness, t, varies linearly with the geometric factor t/L^2 according to the simple relation

$$f = 1.03\sqrt{\frac{E}{\rho}}\frac{t}{L^2}\ , \qquad \text{(A.1.1)}$$

where E is the Young's modulus and ρ is the mass density. In our devices the resonant response is not so simple, as the added mass and stiffness of the metallic electrode modify the resonant frequency of the device. This effect becomes particularly significant as the beam size shrinks. To separate the primary dependence upon the structural material from secondary effects due to electrode loading and stiffness, we employ a simple model for the composite vibrating beam[10]. In general, for a beam comprised of two layers of different materials the resonance equation is modified to become

$$f = \frac{\eta}{L^2}\left(\frac{E_1 I_1 + E_2 I_2}{\rho_1 A_1 + \rho_2 A_2}\right)^{1/2} . \qquad \text{(A.1.2)}$$

Here the indices 1 and 2 refer to the geometric and material properties of the structural and electrode layers, respectively. The constant η depends upon mode number and boundary conditions; for the fundamental mode of a doubly clamped beam η=3.57. Assuming the correction due to the electrode layer (layer 2) is small, we can define a correction factor *K*, to allow direct comparison with the expression for homogeneous beam

$$f = \frac{\eta}{L^2}\left(\frac{E_1 I_{10}}{\rho_1 A_{10}} K\right)^{1/2}, \quad \text{where} \quad K = \frac{E_1 I_1 + E_2 I_2}{E_1 I_{10}} \frac{1}{1 + \dfrac{\rho_2 A_2}{\rho_1 A_1}} . \qquad \text{(A.1.3)}$$

In this expression, I_{10} is the moment calculated in the absence of the second layer. The correction factor K can then be used to obtain a value for the *effective geometric factor*, $[t/L^2]_{eff}$, for the measured frequency[11]. Further nonlinear correction terms, of order higher than $[t/L^2]_{eff}$, are expected to appear if the beams are under significant tensile or compressive stress. The linear trend of our data, however, indicates that internal stress corrections to the frequency are small.

In Fig. A.1.3, we display the measured resonance frequencies as a function of $[t/L^2]_{eff}$ for beams made of three different materials: GaAs, Si and SiC[12]. The lines in this logarithmic plot represent least squares fits to the data assuming unity slope. From these we can deduce the effective values of the parameter, $\upsilon = \sqrt{E/\rho}$, which is similar (but not identical) to the velocity of sound for the three materials[13]. The numerical values obtained by this process are υ(SiC)=1.5×10^4 m/s,[14] υ(Si)=8.4×10^3 m/s,[15] and υ

(GaAs)=4.4 $\times 10^3$ m/s.[16] These are quite close to values calculated from data found in the literature: υ(SiC)=1.2$\times 10^4$ m/s,[14] υ(Si) =7.5$\times 10^3$ m/s,[15] and υ(GaAs)=4.0$\times 10^3$ m/s,[16] respectively. The small discrepancies are consistent with our uncertainties in determining both the exact device geometries and the precise perturbation of the mechanical response arising from the metallic electrodes. Nonetheless, SiC very clearly exhibits the highest $\sqrt{E/\rho}$ ratio.[15]

In conclusion, we report a simple method for fabricating nanomechanical devices from single-crystal 3C-SiC materials. We demonstrate patterning mechanical resonators using a single metal mask, and just two steps of ECR etching. Our results illustrate that SiC is an ideal semiconductor with great promise for device applications requiring high frequency mechanical response.

Acknowledgements: *The authors gratefully acknowledge support for this work from DARPA MTO/MEMS under Grant Nos. DABT63-98-1-0012 (Caltech) and DABT63-98-1-0010 (CWRU). The authors would like to thank Tomoyuki Yoshie for his technical assistance.*

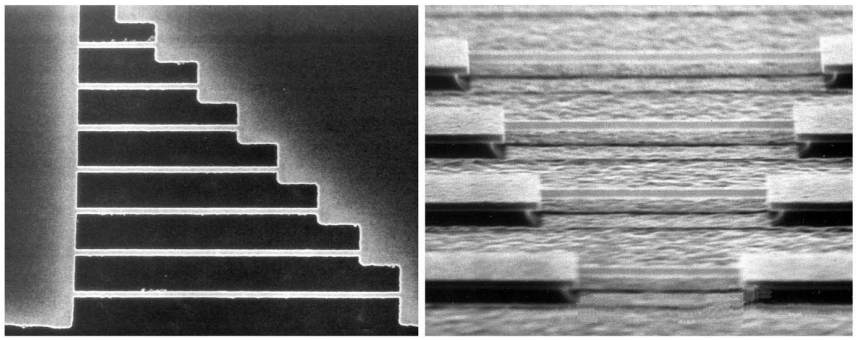

Figure A.1.1 Doubly clamped SiC beams patterned from a 259 nm thick epilayer. (left) Top view of a family of 150 nm wide beams, having lengths from 2 to 8 μm. (right) Side view of a family of 600 nm wide beams, with lengths ranging from 8 to 17 μm.

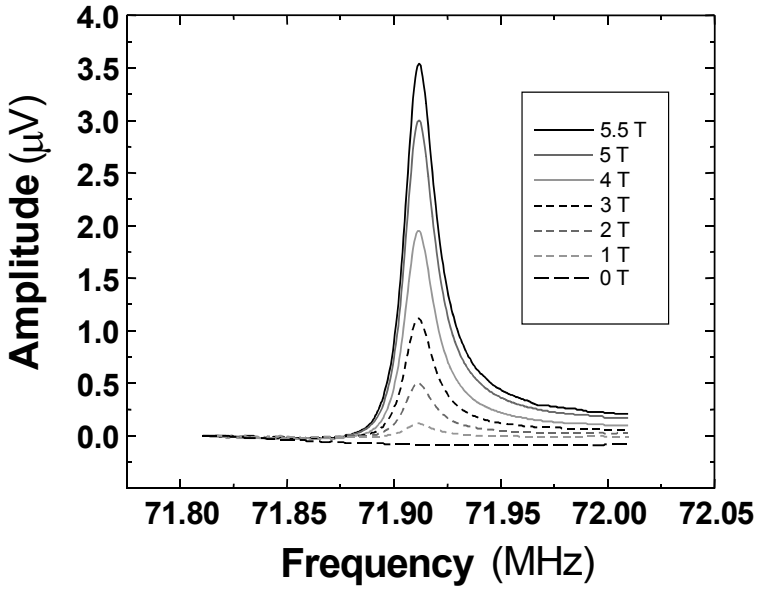

Figure A.1.2 Representative data; a SiC doubly clamped beam resonating at 71.91 MHz, with quality factor $Q \sim 4000$. The family of resonance curves are taken at various magnetic fields; the inset shows the characteristic B^2 dependence expected from magnetomotive detection. For clarity of presentation here the data is normalized to response at zero magnetic field, with the electrode's dc magnetoresistance shift subtracted from the data; these provide an approximate means for separating the electromechanical response from the that of the passive measurement circuitry.

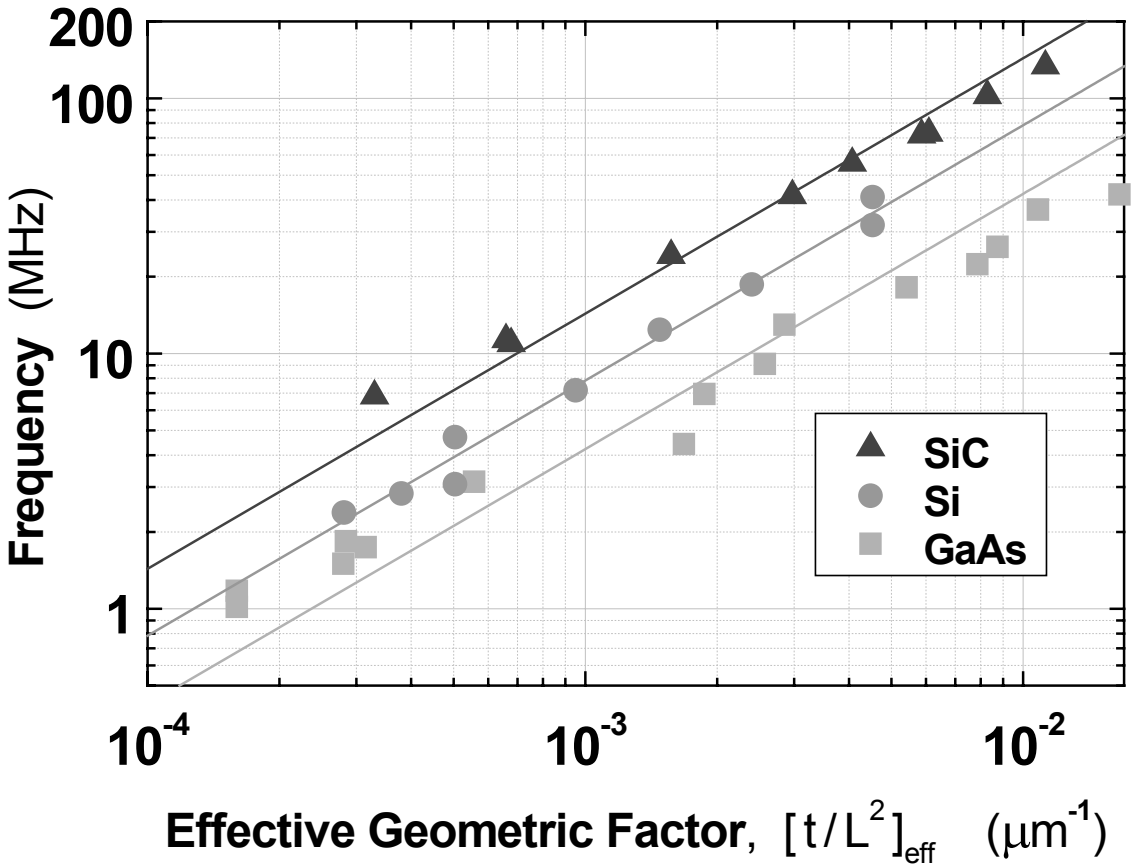

Figure A.1.3 Frequency vs. effective geometry for three families of doubly clamped beams made from single-crystal SiC, Si, and GaAs. All devices are patterned to have the long axis of the device along <100>. Ordinates are normalized to remove the effect of additional stiffness and mass loading from electrode metallization. The solid lines are least squares fits assuming unity slope, and yield values of the parameter $\upsilon = \sqrt{E/\rho}$ that closely match expected values.

References

1. Mehregany, M., Zorman, C. A., Rajan, N. & Wu, C. H. Silicon carbide MEMS for harsh environments. *Proc. IEEE* **86**, 1594-1610 (1998).

2. Roukes, M. L. Nanoelectromechanical systems. in *Technical Digest of the 2000 Solid-State Sensor and Actuator Workshop, Hilton Head Island, SC,* ISBN 0-9640024-3-4 (2000).

3. Ivanov, P. A. & Chelnokov, V. E. Recent developments in SiC single-crystal electronics. *Semicond. Sci. Technol.* **7**, 863-880 (1992).

4. Tong, L. U. & Mehregany, M. Mechanical-properties of 3C- silicon carbide. *Appl. Phys. Lett.* **60**, 2992-2994 (1992).

5. Serre, C., Perez-Rodriguez, A., Romano-Rodriguez, A., Morante, J. R., Esteve, J. & Acero, M. C. Test microstructures for measurement of SiC thin firm mechanical properties. *J. Micromech. Microeng.* **9**, 190-193 (1999).

6. Fleischman, A. J., Wei, X., Zorman, C. A. & Mehregany, M. Surface micromachining of polycrystalline SiC deposited on SiO2 by APCVD. in *Silicon Carbide, III-Nitrides and Related Materials, Pts 1 and 2* 885-888 (Transtec Publications Ltd, Zurich-Uetikon, 1998).

7. Stefanescu, S., Yasseen, A. A., Zorman, C. A. & Mehregany, M. in *Technical Digest, 10th International Conference on Solid State Sensors and Actuators, Sendai, Japan,* 194-197 (1999).

8. Zorman, C. A., Fleischman, A. J., Dewa, A. S., Mehregany, M., Jacob, C., Nishino, S. & Pirouz, P. Epitaxial-growth of 3C-SiC films on 4 inch diam (100) silicon- wafers by atmospheric-pressure chemical-vapor-deposition. *J. Appl. Phys.* **78**, 5136-5138 (1995).

9. Cleland, A. N. & Roukes, M. L. Fabrication of high frequency nanometer scale mechanical resonators from bulk Si crystals. *Appl. Phys. Lett.* **69**, 2653-2655 (1996).

10. Petersen, K. E. & Guarnieri, C. R. Young's modulus measurements of thin-films using micromechanics. *J. Appl. Phys.* **50**, 6761-6766 (1979).

11. The correction factor K primarily reflects mass loading from the metallic electrode. Using values from the literature for Young's modulus of the electrode materials we deduce that the additional stiffness introduced is completely negligible.

12. Electrodes were comprised of either Au or Al, with typical thickness ranging from 50 to 80 nm.

13. The quantity $\sqrt{E_{<100>}/\rho}$ is strictly equal to neither the longitudinal sound velocity, $\sqrt{c_{11}/\rho}$, nor the transverse sound velocity, $\sqrt{c_{44}/\rho}$ for propagation along <100> direction of cubic crystal. Here the *c*'s are elements of the elastic tensor and $E_{<100>} = (c_{11} - c_{12})(c_{11} + 2c_{12})/(c_{11} + c_{12})$ for cubic crystal. See, e.g. B. A. Auld, *Acoustic Fields and Waves in Solids*, 2nd edition (Robert E. Krieger, Malabar, FL, 1990) Vol. 1, Chaps. 6 and 7.

14. Lambrecht, W. R. L., Segall, B., Methfessel, M. & Vanschilfgaarde, M. Calculated elastic-constants and deformation potentials of cubic SiC. *Phys. Rev. B* **44**, 3685-3694 (1991).

15. Hall, J. J. Electronic effects in elastic constants of N-type silicon. *Phys. Rev.* **161**, 756-& (1967).

16. Cottam, R. I. & Saunders, G. A. Elastic-constants of GaAs from 2 K to 320 K. *J. Phys. C: Solid State* **6**, 2105-2118 (1973).

Appendix A.2*

Balanced Electronic Detection of Displacement in Nanoelectromechanical Systems

We describe a broadband radio frequency balanced bridge technique for electronic detection of displacement in nanoelectromechanical systems (NEMS). With its two-port actuation-detection configuration, this approach generates a background-nulled electromotive force in a dc magnetic field that is proportional to the displacement of the NEMS resonator. We demonstrate the effectiveness of the technique by detecting small impedance changes originating from NEMS electromechanical resonances that are accompanied by large static background impedances at very high frequencies. This technique allows the study of important experimental systems such as doped semiconductor NEMS and may provide benefits to other high frequency displacement transduction circuits.

 [DOI: 10.1063/1.1507833]

* This section has been published as: K. L. Ekinci, Y. T. Yang, X. M. H. Huang & M. L. Roukes, *Appl. Phys. Lett.* **78**, 162-164 (2002).

The recent efforts to scale microelectromechanical systems (MEMS) down to the submicron domain[1] have opened up an active research field. The resulting nanoelectromechanical systems (NEMS) with fundamental mechanical resonance frequencies reaching into the microwave bands are suitable for a number of important technological applications. Experimentally, they offer potential for accessing interesting phonon mediated processes and the quantum behavior of mesoscopic mechanical systems.

Among the most needed elements for developing NEMS based technologies—as well as for accessing interesting experimental regimes—are broadband, on-chip transduction methods sensitive to subnanometer displacements. While displacement detection at the scale of MEMS has been successfully realized using magnetic[2], electrostatic[3,4] and piezoresistive[5] transducers through electronic coupling, most of these techniques become insensitive at the submicron scales. Moreover, the attractive electronic two-port actuation-detection configuration of most MEMS devices becomes hard to realize at the scale of NEMS, due to the unavoidable stray couplings encountered with the reduced dimensions of NEMS.

An on-chip displacement transduction scheme that scales well into the NEMS domain and offers direct electronic coupling to the NEMS displacement is magnetomotive detection[6,7]. Magnetomotive reflection measurements as shown schematically[8] in Fig. A.2.1a have been used extensively[6,7,9]. Here, the NEMS resonator is modeled as a parallel *RLC* network with a mechanical impedance, $Z_m(\omega)$, a two-terminal dc coupling resistance, R_e, and mechanical resonance frequency, ω_0. When

driven at ω by a source with impedance R_s, the voltage on the load, R_L, can be approximated as

$$V_0(\omega) = V_{in}(\omega)\frac{R_e + Z_m(\omega)}{R_L + \left(R_e + Z_m(\omega)\right)} \cong V_{in}(\omega)\frac{R_e + Z_m(\omega)}{R_L + R_e} \ . \qquad \text{(A.2.1)}$$

Here, $R_L = R_s = 50\Omega$. We have made the approximation that $R_e >> |Z_m(\omega)|$, as is the case in most experimental systems. Apparently, the measured electromotive force (EMF) due to the NEMS displacement proportional to $Z_m(\omega)$ is embedded in a background close to the drive voltage amplitude[10]. This facilitates the definition of a useful parameter at $\omega = \omega_0$, the detection *efficiency*, *S*/*B*, as the ratio of the signal voltage to the background. For the reflective, one-port magnetomotive measurement of Fig. A.2.1a, $S/B = Z_m(\omega_0)/R_e = R_m/R_e$, indicating some shortcomings. First, detection of the EMF becomes extremely challenging, when $R_e \gg R_m$, i.e., in unmetallized NEMS devices or metallized high frequency NEMS (small R_m). Second, the voltage background prohibits the use of the full dynamic range of the detection electronics. As mentioned above, a two-port actuation-detection configuration cannot remedy these problems due to the stray electronic coupling between the ports[11].

The balanced circuit shown in Fig. A.2.1b with a NEMS resonator on one side of the bridge and a matching resistor of resistance, $R = R_e + \Delta R$ on the other side, is designed to improve *S*/*B*. The voltage, $V_0(\omega)$ at the readout (RO) port is nulled for $\omega \neq \omega_0$, by applying two 180° out of phase voltages to the Drive 1 (D1) and Drive 2 (D2) ports in the circuit. We have found that the circuit can be balanced with exquisite sensitivity, by fabricating two identical doubly clamped beam resonators on either side of

the balance point (RO), instead of a resonator and a matching resistor, as shown in Fig. A.2.1c. In such devices, we almost always obtained two well-separated mechanical resonances, one from each beam resonator, with $|\omega_2 - \omega_1| >> \omega_i / Q_i$, where ω_i and Q_i are the resonance frequency and the quality factor of resonance of the resonators (i=1,2) (see Fig. A.2.3). This indicates that in the vicinity of either mechanical resonance, the system is well described by the mechanical resonator-matching resistor model of Fig. A.2.1b. We attribute this behavior to the high Q factors ($Q \geq 10^3$) and the extreme sensitivity of the resonance frequencies to local variations of parameters during the fabrication process.

First, to clearly assess the improvements, we compared reflection and balanced bridge measurements of the fundamental flexural resonances of doubly clamped beams patterned from n^+ (B-doped) Si as well as from n^+ (Si-doped) GaAs. Electronic detection of mechanical resonances of these types of NEMS resonators have proven to be challenging[12], since for these systems $R_e \geq 2k\Omega$ and $R_m \leq R_e$. Nonetheless, with the bridge technique we have detected fundamental flexural resonances in the 10 MHz<f_0<85 MHz range for n^+ Si resonators and in the 7 MHz <f_0<35 MHz range for n^+ GaAs beams. In all our measurements, the paradigm that $R_m \ll R_e$ remained true as $R_m \leq 10\Omega$ and $2k\Omega < R_e < 20k\Omega$. Here, we focus on our results from n^+ Si beams. These were fabricated from a B-doped Si on insulator wafer, with Si layer and buried oxide layer thicknesses of 350 and 400 nm, respectively. The doping was done at 950°C. The dopant concentration was estimated as $N_a \approx 6\times10^{19}$ cm^{-3} from the sample sheet resistance, $R_\square \approx 60\Omega$.[13] The fabrication of the actual devices involved optical lithography, electron beam lithography, and lift-off steps followed by anisotropic electron cyclotron resonance

plasma and selective HF wet etches[7,9,12]. The electromechanical response of the bridge was measured in a magnetic field generated by a superconducting solenoid. Fig. A.2.2a shows the response of a device with dimensions 15 μm (L) × 500 nm (w) × 350 nm (t) and with $R_e \approx 2.14k\Omega$, measured in the reflection (upper curves) And bridge configurations for several magnetic field strengths. The device has an in plane flexural resonance at 25.598 MHz with a $Q \approx 3\times10^4$ at $T \approx 20\,\mathrm{K}$. With $\Delta R \approx 10\Omega$ a background reduction of a factor of $\sim 200 \sim R_e / \Delta R$ was obtained in the bridge measurements (see analysis below). Fig. A.2.2b shows a measurement of the broadband transfer functions for both configurations for comparable drives at zero magnetic field. Notice the dynamic background reduction in the relevant frequency range.

Bridge measurements also provided benefits in the detection of electromechanical resonances from metallized VHF NEMS. These systems generally possess high R_e and R_m diminishes quickly as the resonance frequencies increase. Here, we present from our measurements on doubly clamped SiC beams embedded within the bridge configuration. These beams were fabricated with top metallization layers using a process described in detail[9]. For such beams with $R_e \sim 100\Omega$ and $R_m \leq 1\Omega$, we were able to detect mechanical flexural resonances deep into the VHF band. Fig. A.2.3a depicts a data trace of the in plane flexural mechanical resonances of two 2μm(L) × 150nm(w) × 80nm(t) doubly clamped SiC beams. Two well-separated resonances are extremely prominent at 198.00 and 199.45 MHz, respectively, with Q ~10^3 at T~4.2 K. The broadband response from the same device is plotted in Fig. A.2.3b. A reflection measurement in the vicinity of the mechanical resonance frequency of this system would give rise to an estimated

background on the order, $|V_0/V_{in}| \sim -20\,\mathrm{dB}$ (Ref. 10), making the detection of the resonance extremely challenging.

Fig. A.2.1b depicts our analysis of the bridge circuit. The voltage at point RO in the circuit can be determined as[14]

$$\begin{aligned} V(\omega) &= -\frac{V_{in}(\omega)[\Delta R + Z_m(\omega)]}{(Z_m(\omega)+\Delta R)(1+R_e/R_L)+R_e(2+R_e/R_L)} \\ &= -\frac{V_{in}(\omega)}{Z'_{eq}(\omega)}[\Delta R + Z_m(\omega)] \end{aligned} \tag{A.2.2}$$

by analogy to Eq. (A.2.1). At $\omega = \omega_0$, $S/B = R_m/\Delta R$. Given that ΔR is small, the the background is suppressed by a factor of order $R_e/\Delta R$, as compared to the one-port case [Fig. A.2.2a]. At higher frequencies, however, the circuit model becomes imprecise as is evident from the measurements of the transfer function. Capacitive coupling becomes dominant between D1, D2, and RO ports as displayed in Fig. A.2.2b, and this acts to reduce the overall effectiveness of the technique. With careful design of the circuit layout and the bonding pads, such problems can be minimized. Even further signal improvements can be obtained by addressing the significant impedance mismatch, $R_e \gg R_L$, between the output impedance, R_e, and the amplifier input impedance, R_L. In the measurements displayed in Fig. A.2.2a, this mismatch caused a signal attenuation estimated to be of order ~40 dB.

Our measurements on doped NEMS offer insight into energy dissipation mechanisms in NEMS, especially those arising from surfaces and surface adsorbates. In the frequency range investigated, 10MHz < f_0 < 85MHz, the measured Q factors of $2.2\times10^4 < Q < 8\times10^4$ in n^+ Si beams is a factor of 2–5 higher than those obtained from metallized beams[15]. Both metallization layers[16] and impurity dopants[3] can make an

appreciable contribution to the energy dissipation. Our measurements on NEMS seem to confirm that metallization overlayers can significantly reduce Q factor. The high Q factors attained and the metal free surfaces make doped NEMS excellent tools for the investigation of small energy dissipation changes due to surface adsorbates and defects. In fact, efficient *in situ* resistive heating in doped beams through R_e has been shown to facilitate thermal annealing[17] and desorption of surface adsorbates—yielding even higher Q factors.

In summary, we have developed a broadband, balanced radio frequency bridge technique for detection of small NEMS displacements. This technique may prove useful for other high frequency high impedance applications such as piezoresistive displacement detection. The technique, with its advantages, has enabled electronic measurements of NEMS resonances otherwise essentially unmeasurable.

Acknowledgements: *The authors gratefully acknowledge support from DARPA MTO/MEMS under Grant No. DABT63-98-1-0012 and technical assistance from D. Harrington.*

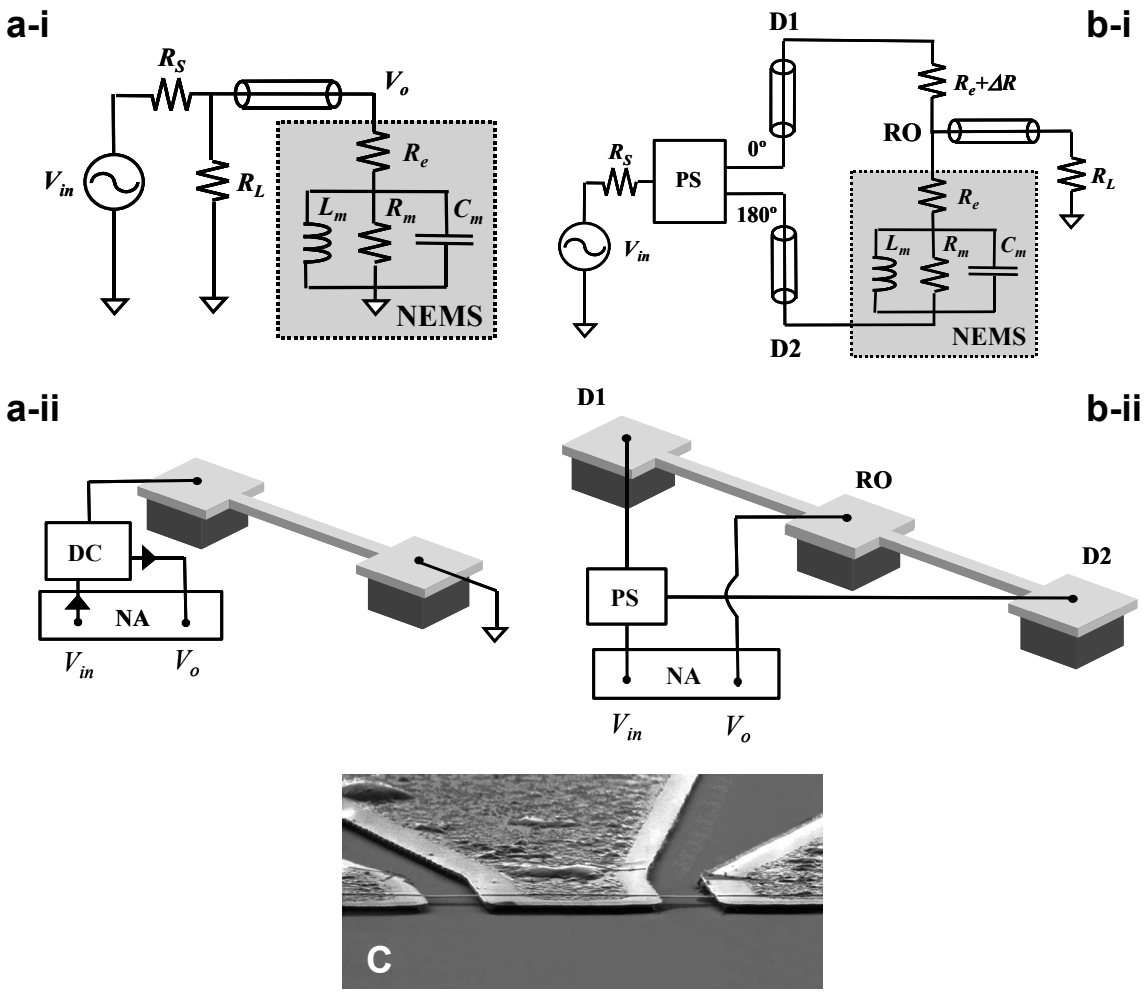

Figure A.2.1 a, Schematic diagram for the magnetomotive reflection mesurement. In both reflection and bridges measurements, a network analyzer (NA) supplies the drive voltage, V_{in} . In reflection measurement, a directional coupler (DC) is implemented to access the reflected signal from the device. **b,** Schematic diagram for the magnetomotive bridge measurement. V_{in} is split into two out of phase components by a power splitter (PS) before it is applied to ports D1 and D2. **c,** Scanning electron micrograph of a representative bridge device, made out of an epitaxially grown wafer with 50 nm thick n^+ GaAs and 100 nm thick intrinsic GaAs structural layers on top of a 1 μm thick AlGaAs sacrificial layer. The doubly clamped beams with dimensions of 8 μm(L) × 150nm(w) × 500 nm(t) at the two arms of the bridge have in plane fundamental flexural mechanical resonances at ~35 MHz. D1, D2, and RO ports on the device are as shown.

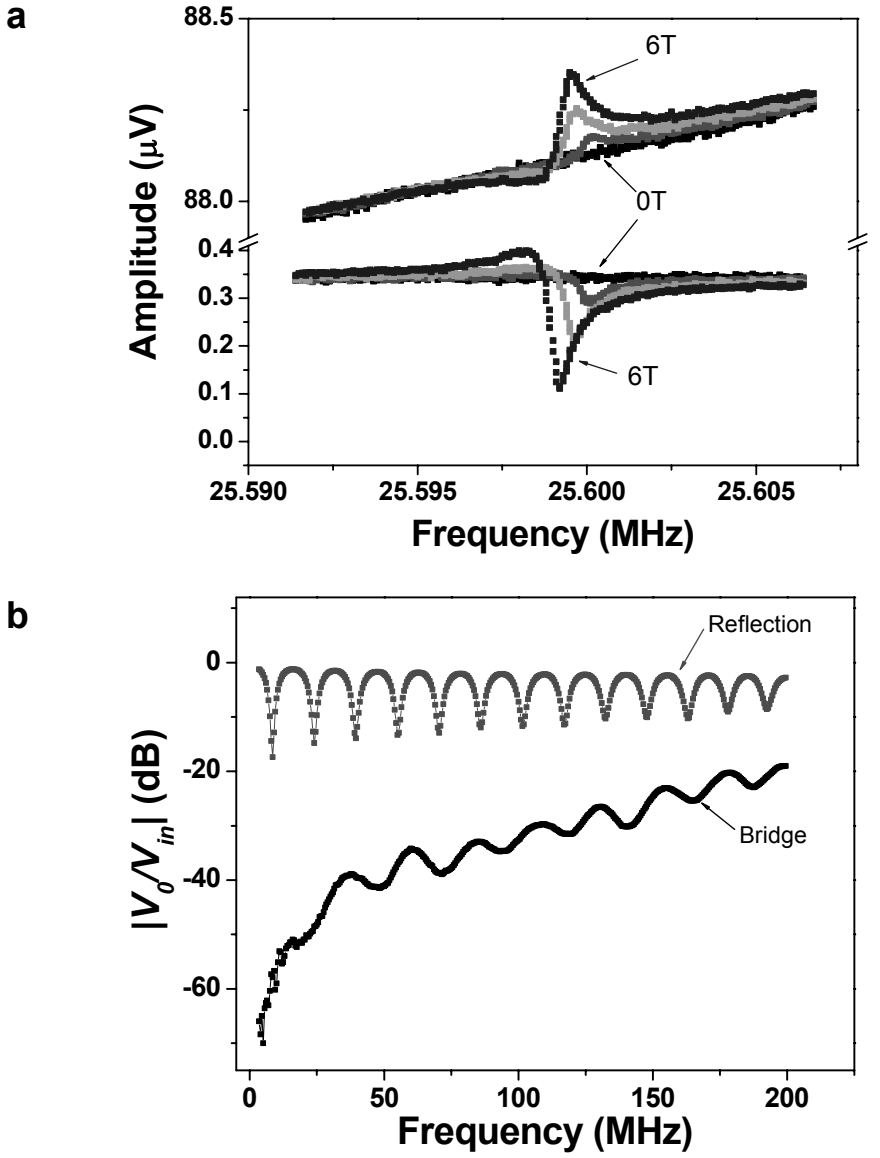

Figure A.2.2 a, Data from a doubly clamped, n^+ Si beam resonating at 25.598 MHz with a $Q \approx 3\times10^4$ measured in reflection (upper curves) and in bridge configurations for magnetic field strengths of B = 0,2,4,6 T. The drive voltages are equal. The background is reduced by a factor of ~200 in the bridge measurements. The phase of the resonance in the bridge measurements can be shifted 180° with respect to the drive signal (see Fig. A.2.3). **b,** The amplitude of the broadband transfer functions, $H(\omega) = V_0(\omega)/V_{in}(\omega)$ for both configurations. The data indicate a background reduction of at least 20 dB and capacitive coupling between the actuation–detection ports in the bridge circuit.

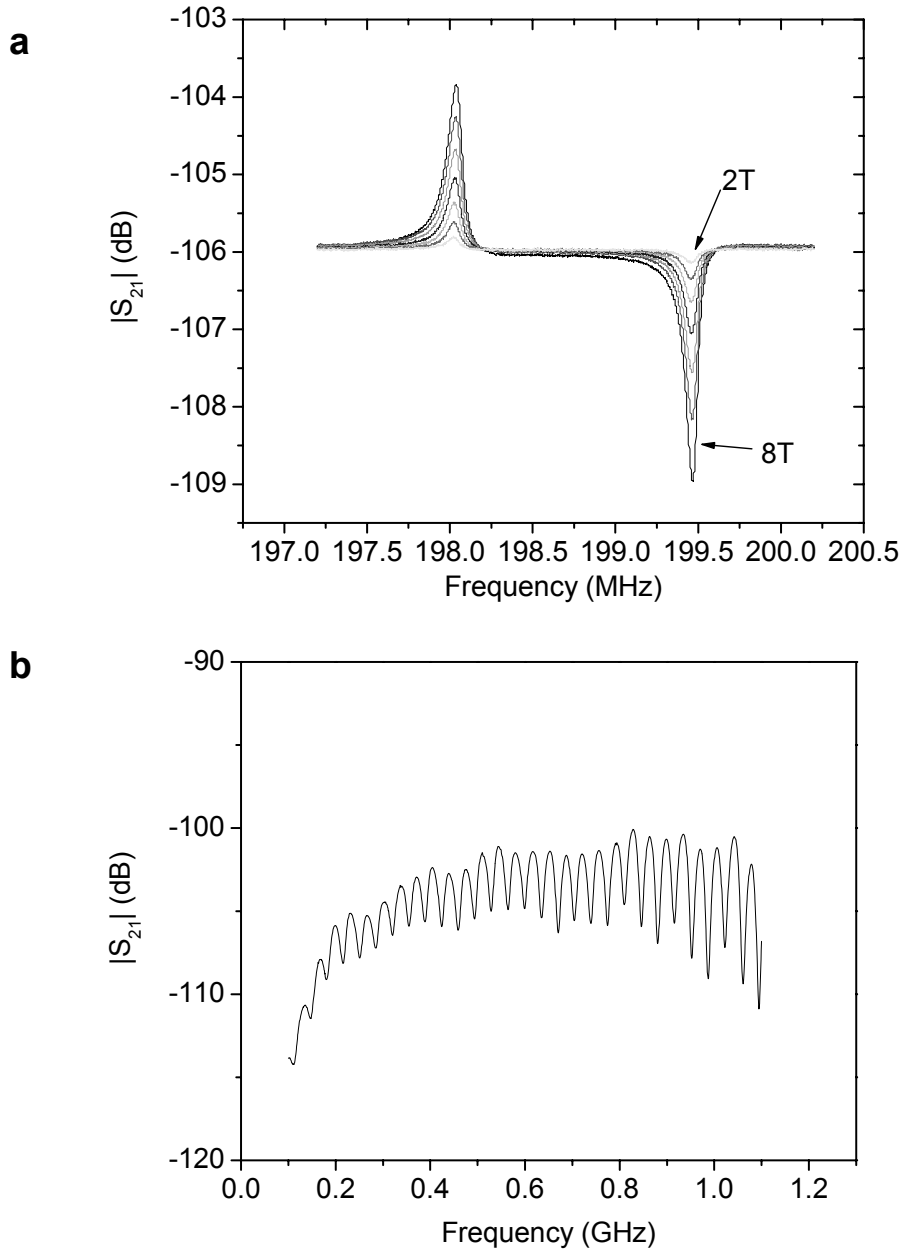

Figure A.2.3 Narrow band (a) and broadband (b) transfer function (S_{21}) amplitudes from metallized SiC beams in bridge configuration. **a,** The narrowband response is measured for different magnetic field strengths of B=2,4,6,8 T and shows two well-separated resonances at 198.00 and 199.45 MHz, respectively, with Q~10^3. **b,** The broadband response at B=0 T shows the significant background nulling attainable in bridge measurements. We estimate that a reflection measurement on this system would produce $|V_0 / V_{in}| \sim -20\,\mathrm{dB}$ for $\omega \approx \omega_0$.

References

1. Roukes, M. L. Nanoelectromechanical systems face the future. *Phys. World* **14**, 25-31 (2001).

2. Greywall, D. S., Yurke, B., Busch, P. A., Pargellis, A. N. & Willett, R. L. Evading amplifier noise in nonlinear oscillators. *Phys. Rev. Lett.* **72**, 2992-2995 (1994).

3. Mihailovich, R. E. & Parpia, J. M. Low-temperature mechanical-properties of Boron-doped Silicon. *Phys. Rev. Lett.* **68**, 3052-3055 (1992).

4. Tang, W. C., Nguyen, T. C. H., Judy, M. W. & Howe, R. T. Electrostatic-comb drive of lateral polysilicon resonators. *Sens. Actuator A-Phys.* **21**, 328-331 (1990).

5. Tortonese, M., Barrett, R. C. & Quate, C. F. Atomic resolution with an atomic force microscope using piezoresistive detection. *Appl. Phys. Lett.* **62**, 834-836 (1993).

6. Cleland, A. N. & Roukes, M. L. Fabrication of high frequency nanometer scale mechanical resonators from bulk Si crystals. *Appl. Phys. Lett.* **69**, 2653-2655 (1996).

7. Cleland, A. N. & Roukes, M. L. External control of dissipation in a nanometer-scale radiofrequency mechanical resonator. *Sens. Actuator A-Phys.* **72**, 256-261 (1999).

8. To simplify, the length of the transmission line, *l*, between the NEMS and the measurement point has been set to $l \approx \lambda/2$, where λ is the drive wavelength. Also, the reflection coefficient, Γ, from the NEMS, defined as the ratio of the amplitudes of reflected to incident voltages, is taken as unity. Experimentally, *l* is readily adjustable and $\Gamma \sim 1$ with $R_e \sim 100\Omega \rightarrow 1k\Omega$.

9. Yang, Y. T., Ekinci, K. L., Huang, X. M. H., Schiavone, L. M., Roukes, M. L., Zorman, C. A. & Mehregany, M. Monocrystalline silicon carbide nanoelectromechanical systems. *Appl. Phys. Lett.* **78**, 162-164 (2001).

10. When $\Gamma \neq 1$, $V_0 \cong \Gamma V_{in}(R_e + Z_m(\omega))/(R_L + R_e)$, giving a correction to the background on the order of $-20\log\Gamma$ dB.

11. Yang, Y. T., Ekinci, K. L. & Roukes, M. L. (unpublished).

12. Pescini, L., Tilke, A., Blick, R. H., Lorenz, H., Kotthaus, J. P., Eberhardt, W. & Kern, D. Suspending highly doped silicon-on-insulator wires for applications in nanomechanics. *Nanotechnology* **10**, 418-420 (1999).

13. Sze, S. M. *Physics of Semiconductor Devices* (Wiley, New York, 1981).

14. Replacing R_e with $R_e + R_s$ would produce the more general form.

15. We have qualitatively compared Q factors of eight metallized and 14 doped Si beams measured in different experimental runs, spanning the indicated frequency range.

16. Liu, X., Thompson, E. J., White, B. E. & Pohl, R. O. Low-temperature internal friction in metal films and in plastically deformed bulk aluminum. *Phys. Rev. B* **59**, 11767-11776 (1999).

17. Yasumura, K. Y., Stowe, T. D., Chow, E. M., Pfafman, T., Kenny, T. W., Stipe, B. C. & Rugar, D. Quality factors in micron- and submicron-thick cantilevers. *J. Microelectromech. Syst.* **9**, 117-125 (2000).

Appendix A.3*

Two-Dimensional Electron-Gas Actuation and Transduction for GaAs Nanoelectromechanical Systems

We have fabricated doubly clamped beams from GaAs/AlGaAs quantum-well heterostructures containing a high-mobility two-dimensional electron gas (2DEG). Applying an rf drive to in-plane side gates excites the beam's mechanical resonance through a dipole–dipole mechanism. Sensitive high-frequency displacement transduction is achieved by measuring the ac emf developed across the 2DEG in the presence of a constant dc sense current. The high mobility of the incorporated 2DEG provides low-noise, low-power, and high-gain electromechanical displacement sensing through combined piezoelectric and piezoresistive mechanisms.

 [DOI: 10.1063/1.1516237]

* This section has been published as: H. X. Tang, X. M. H. Huang, M. L. Roukes, M. Bichler & W. Wegscheider , *Appl. Phys. Lett.* **81**, 3879-3881 (2002).

Thin, suspended two-dimensional electron gas (2DEG) heterostructures have been recently perfected, and have subsequently been employed for nanoscale conducting devices[1,2]. In this letter, we present a high-resolution displacement readout that is based upon our ability to achieve very high mobility suspended quantum wires. Molecular beam epitaxial (MBE) grown materials are directly patterned and in-plane gates are used to excite the vibration. No metallization is needed, hence high Q values can be obtained.

The starting material was a specially designed, MBE grown, 2DEG heterostructure similar to that used in Ref. 1. The structural layer stack comprises seven individual layers having a total thickness of 115 nm. The top and bottom are thin GaAs cap layers preventing oxidation of the $Al_{0.3}Ga_{0.7}As$:Si donor layers in between. The central 10 nm thick GaAs layer forms a quantum well sustaining a high mobility 2DEG located 37 nm below the top surface and surrounded by two AlGaAs spacer layers. Below the structural layer stack is a 400 nm $Al_{0.8}Ga_{0.2}As$ sacrificial layer. The structure was intentionally made asymmetric to avoid neutralizing the piezoelectric effect of GaAs.

After ohmic contacts were deposited, a thick layer of poly-methyl-methacrylate (PMMA) is spun on the chip, followed by a single electron-beam lithography step to expose trenches in PMMA that isolate the beam from its side gates. PMMA was then employed as a direct mask against a low voltage electron cyclotron resonance etch performed to further etch the trenches to the sacrificial layer. After stripping off the PMMA, final structure relief is achieved by removing the sacrificial layer beneath the beams with diluted HF. To minimize the damage to the 2DEG from dry etching, a Cl_2 /He plasma was chosen because of its excellent etching characteristics, such as smooth surface morphology and vertical sidewall. A stable etching speed at 35Å /s is obtained

under conditions of less than 150 V self-bias (20 W constant rf power), Cl_2 and He flow rate ratio 1:9, 3 mTorr pressure, and 300 W microwave power. With the same method, we have also fabricated suspended Hall bars and extensively characterized the resulting suspended 2DEG. Before processing, the initial mobility and density after illumination are 5.1×10^5 cm^2/Vs, 1.26×10^{12} cm^{-2}, respectively. With our improved low damage etching, the mobility can be maintained at 2.0×10^5 cm^2/Vs, while the electron density is somewhat reduced to 4.5×10^{11} cm^{-2}. We observed well-developed quantum Hall plateaus in the etched structure even with channel width as small as 0.35 μm. In longitudinal resistance measurements, we detected a low field maximum, corresponding to maximal boundary scattering when the electron cyclotron motion diameter matches the electrical width of the suspended wire[3]. From the position of this peak, we are able to deduce the depletion to be 0.1 μm on each side of the wire. We also confirmed ballistic behavior of electrons from transport measurement on the Hall cross-junction. Both ‘‘last Hall plateau’’ and ‘‘negative bend resistance’’[4] are present in all of the devices. The transport mean free path was found to be approximately 2 μm.

A typical device is shown in Fig. A.3.1. The beams are 0.5 μm wide and 6 μm long, having a calculated spring constant of 0.25 N/m. When cooled to liquid helium temperature, their two-terminal resistance is about 100 $k\Omega$. After illumination, this drops to about 5 $k\Omega$ (including contact and lead resistances). The electrical width of the beam is about 0.3 μm with $R_{\square} = 170\Omega$.

In nanoelectromechanical system (NEMS), both the induction and the detection of motion pose important challenges. In our devices, the actuation is relatively trivial and very effective. The rf drive is supplied directly to one of the side gates, which is a large

area of 2DEG connected to the output of a network analyzer through alloyed ohmic contact. All the trenches have a width of 0.5 μm. The devices are first measured at 4.2 K in vacuum. A constant dc sensing current ranging from 0 to 26 μA is supplied to the vibrating beam through a 10 mH rf choke, whose value is chosen large enough to avoid loss of the small signal that is induced. The oscillatory signal is picked up by a low temperature amplifier placed in close proximity to the device. Before connecting the signal to the input of the network analyzer, a room temperature amplifier is used to improve signal-to-noise ratio. The combined amplifiers have a voltage gain of about 200 in the frequency range of these experiments.

We observed a very strong signal around the first mechanical resonance. The magnitude response curves at various driving amplitudes are shown in Fig. A.3.2a. Calculations confirm this resonance corresponds to the first out-of-plane vibrational mode. When the drive amplitude is increased above 45 mV, the response curve becomes nonlinear and assumes an asymmetric shape. In the linear response region, the amplitude at resonance is proportional to the ac gate voltage amplitude.

To clarify the origin of the observed signal, we fixed the drive at 10 mV and then varied the dc bias current from −26 μA to 0 and then to 26 μA. The response amplitude versus drive amplitude at resonance is presented in Fig. A.3.2b. Two features are evident from this data. First, at the highest currents close to 20 μA, the signal becomes saturated for two reasons: (a) Joule heating of the small beam, and (b), saturation of the drift velocity at high applied electrical fields (~15 kV/m). Second, at intermediate current the signal strength at resonance is proportional to the dc bias current, as indicated in the inset of Fig. A.3.2b. In addition, when we reverse the current direction, we also find that the

induced signal changes its sign (180° phase change). Therefore, we conclude that the dominant contribution to the observed signal is a change of resistance due to beam vibration. This appears to originate from both piezoresistive effect of bulk GaAs and transverse piezoelectric charge gating of 2DEG. Note that a small signal is observed even for zero current bias. From the slope of the linear part in the inset of Fig. A.3.2b, a nominal drive of 10 mV induces a resistance change of about 10 Ω in the device.

We now estimate the sensitivity of this technique. By looking at the critical amplitude at the onset of nonlinearity, we can determine the amplitude of vibration of the resonating beam. This critical displacement amplitude depends only on the geometry of the beam, and is approximately given as[5] $x_c \sim (2h)/\sqrt{0.5Q(1-\nu^2)}$, where h is the thickness of the beam in the vibration direction, and ν is Poisson's ratio for GaAs. Plugging in measured values of Q=2600 and ν=0.31, we obtain x_c=6 nm, which is attained at a drive level of about 45 mV. The minimum resolvable signal is achieved at 0.1 mV drive and about 5 μA sensing current. Hence, at the highest possible current of 20 μA, we can detect a resonance at x_c/450/4=0.03 Å, or 3×10^{-3} Å$/\sqrt{Hz}$, which is consistent with our estimate based on Johnson noise from beam resistance at 4.2 K. The corresponding force sensitivity is 75 fN$/\sqrt{Hz}$, comparable with previous schemes to detect small NEMS resonators by optical interferometry[6] and the magnetomotive method[7]. The required force to drive the beam to the nonlinearity threshold is 1.5 nN. The displacement resolution can be improved by using 2DEG heterostructures with even higher mobility, or by operating at ~100 mK with a state-of-the-art low temperature preamplifier.

Note that in Fig. A.3.2, all the driving force results from the applied ac gate voltage. We did not find any significant change of resonant frequency or magnitude with dc bias on the gate. This is indicative of a coupling mechanism different from electrostatic force between the gates and the beam. Electrostatic force is proportional to the product of dc and ac components of gate potential so that the response should directly scale with the dc gate voltage[8]. This assumes a direct Coulomb interaction between coupling plates. In our inplane-gate configuration, the net charge on the beam is $C(V_g^{(0)} + \upsilon_g e^{i\omega t})$. The capacitance between coplanar 2DEG areas has an estimated value of 18 aF/μm,[9] which is very small compared to parallel plates. With a nominal 1 V dc gate voltage, there are only a few hundred induced electron charges on the beam. The upper bound of the electric field applied on the gate is $(V_g^{(0)} + \upsilon_g e^{i\omega t})/d$, d is the beam–gate separation (Fig. A.3.3). Thus, the total electrostatic force applied on the beam with angular frequency ω is $f = CV_g^{(0)}\upsilon_g e^{i\omega t}/d$. Only a projection of this force drives the beam along the out-of-plane (y) direction. A reasonable estimate of the effective y-component of this force is

$$f_y = CV_g^{(0)}V_g e^{i\omega t} y_0 / d^2, \tag{A.3.1}$$

where y_0 is a static offset due to, for example, uncontrolled asymmetry of suspended beam. A 10 nm misalignment of the beam with respect to gate should be observable in our devices (but is not seen). Therefore, we take this number as the upper limit in our estimation of y_0. At a nominal 1 V dc gate voltage, 45 mV ac gate voltage, the force originating from the electrostatic drive mechanism is calculated to be $f_y \approx 0.2\,pN$. This

is four orders of magnitude smaller than the force required to drive the beam into nonlinear response.

Given the absence of direct electrostatic forces, we propose a new driving mechanism, a short-range dipole-dipole interaction. This dipole–dipole interaction potential can be expressed as $U = \int \frac{1}{4\pi\varepsilon_0} \frac{p_2 dp_1}{r^3}$, which can be understood as rf coupling between two dipole moments dp_1 and p_2. Here dp_1 is the dipole momentum of a slice of the gate, $dp_1 = \varepsilon_r \varepsilon_0 L V_g e^{i\omega t} dr$, and p_2 is the fixed dipole moment due to the piezoelectric effect within the strained beam. *y* is the beam displacement, $p_2 = 3Ed_A wt^2 \Delta y / L$, and *L*, *w*, and *t* are beam length, width and thickness, respectively (Fig. A.3.3). ε_r is dielectric constant of GaAs. Here, *E* ~ 85 Gpa is Young's modulus and $d_A \sim 3.8 pC/N$ is the piezoelectric constant of AlGaAs.[10] The resulting force along *y* direction is

$$f_y = \frac{\partial U}{\partial y} = \frac{3\varepsilon_r}{4\pi}\left(Ed_A\right)\left(\frac{wt^2}{d^2}\right)V_g e^{i\omega t}. \qquad \text{(A.3.2)}$$

This dynamic force is *independent* of the dc gate voltage, consistent with our observation. After structural relief, the suspended beams are intrinsically stressed due to the heterostructure's asymmetry and other factors. Therefore, a static dipole moment exists on the beam and yields the out-of-plane vibration. At 45 mV ac gate voltage drive, f_y is estimated to be 1.2 nN from this mechanism, four orders of magnitude higher than the direct Coulomb interaction. This is consistent with the force we observe at the onset of nonlinearity. Because of its short-range characteristics, this dipole–dipole interaction is unique to NEMS and is insignificant in microelectromechanical systems.

We have also studied the temperature dependence of our strain sensitive devices. Measurements were performed at three different temperatures in vacuum. The results are shown in Fig. A.3.4. The devices perform exceptionally well at liquid helium and nitrogen temperatures, but at room temperature, the response is diminished. The decay of signal strength with temperature can be attributed to the significant reduction of 2DEG mobility. At elevated temperature the increased two-terminal beam resistance acts as a large voltage divider, and only a small fraction of induced signal voltage is available.

Acknowledgements: *We gratefully acknowledge support from DARPA, through Grant No. DABT63-98-1-0012, and the NSF via grant ECS-0089061. We also thank F. G. Monzon and J. Casey for early contributions to this work, and J. Y. T. Yang and K. Cooper for help with the low temperature amplifier.*

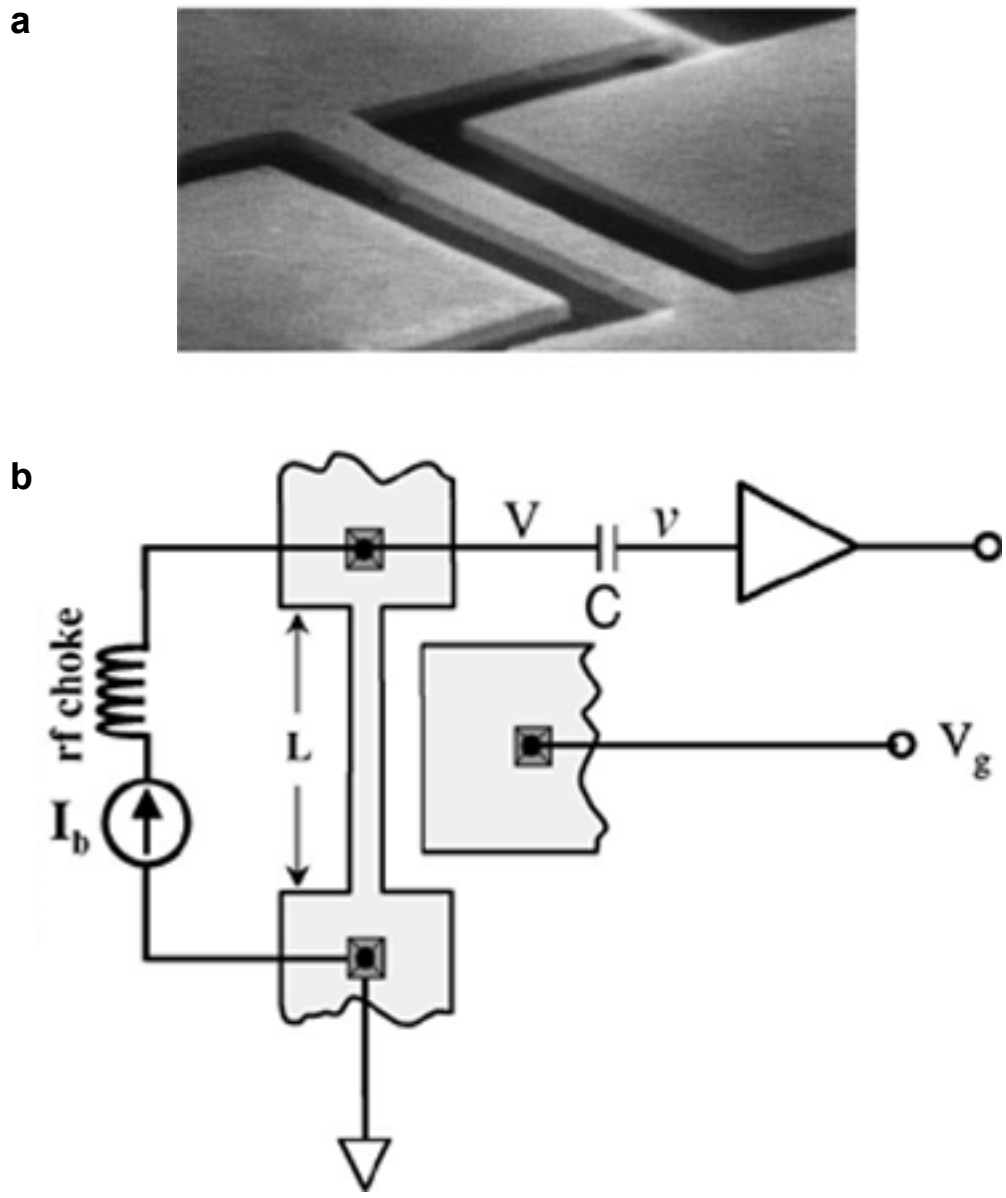

Figure A.3.1 a, SEM image of a doubly clamped beam. The in-plane gates are formed by the 2DEG. **b,** Sketch of measurement setup. A constant dc bias current (I_b) is sent through a large rf choke (~10 mH). Gate drive voltage consists of both dc and rf components: $V_g = V_g^{(0)} + \upsilon_g e^{i\omega t}$. The induced signal can be expressed as $V = V^{(0)} + \upsilon e^{i(\omega t+\varphi)}$, where the dc voltage $V^{(0)} = I_b R_{dc}$ is blocked by a capacitor C, and the oscillating component is amplified.

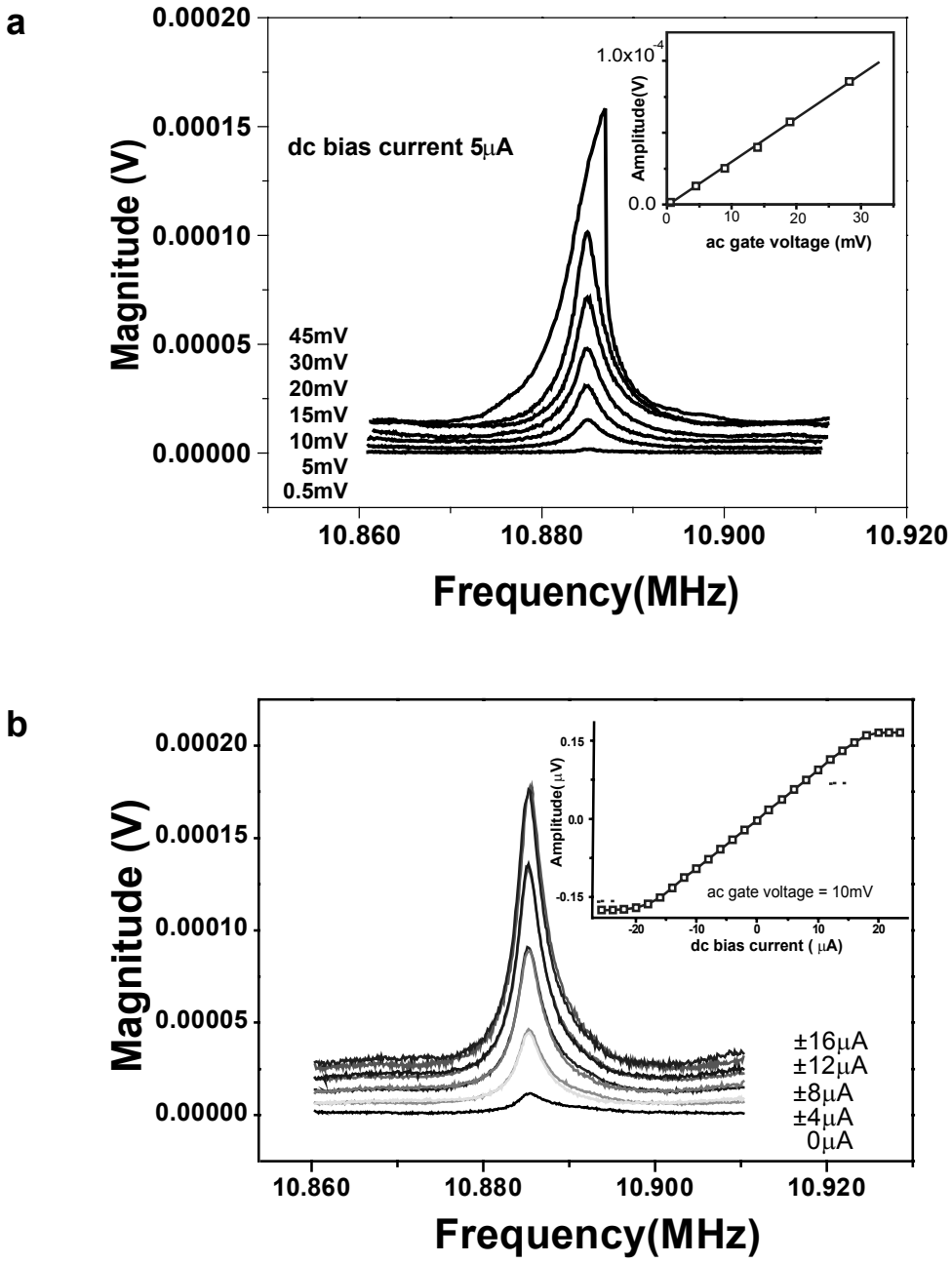

Figure A.3.2 a, Voltage drop across the beam as it is driven to its lowest mechanical resonance with increasing drive amplitudes. The dc bias current is fixed at 5 μA. Inset: The peak response as a function of driving amplitude in the linear regime. **b,** Magnitude response vs. dc bias current. Inset: The signal amplitude at resonance with sensing current increased from -26 to 26 μA.

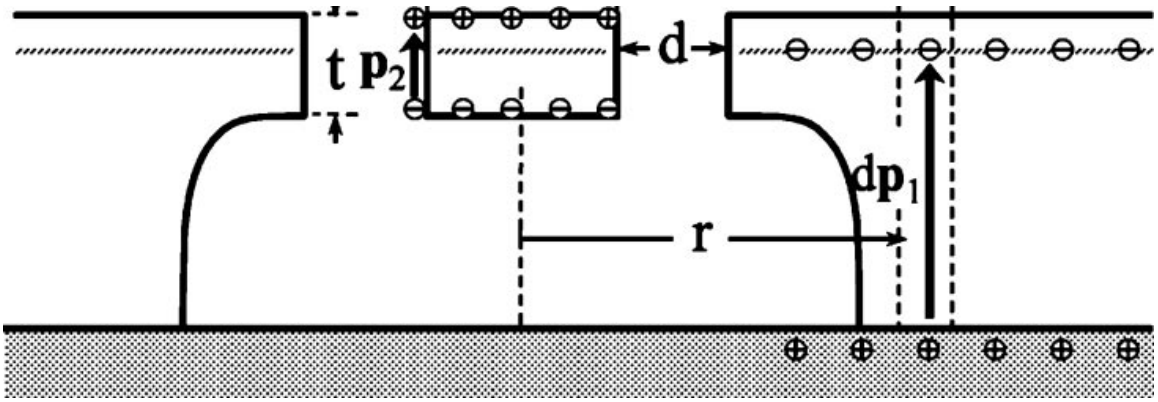

Figure A.3.3 A cross-sectional schematic of the dipolar actuation mechanism, showing dipole formation on the beam (p_1) and on the driving gate (dp_2).

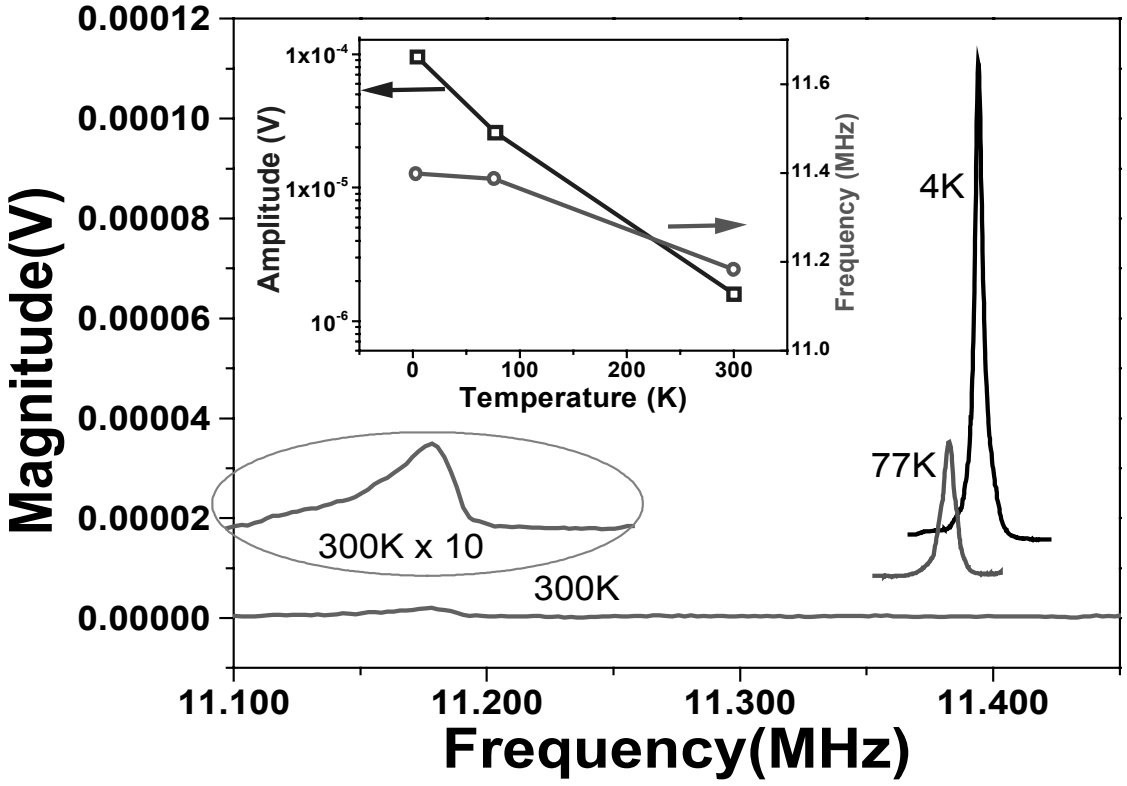

Figure A.3.4 Response curve at three different temperatures. Inset: Sketch of amplitude and frequency change with increasing temperature.

References

1. Blick, R. H., Monzon, F. G., Wegscheider, W., Bichler, M., Stern, F. & Roukes, M. L. Magnetotransport measurements on freely suspended two-dimensional electron gases. *Phys. Rev. B* **62**, 17103-17107 (2000).

2. Beck, R. G., Eriksson, M. A., Westervelt, R. M., Chapman, K. L. & Gossard, A. C. Strain-sensing cryogenic field-effect transistor for integrated strain detection in GaAs/AlGaAs microelectromechanical systems. *Appl. Phys. Lett.* **68**, 3763-3765 (1996); Beck, R. G. et al. GaAs/AlGaAs self-sensing cantilevers for low temperature scanning probe microscopy. *Appl. Phys. Lett.* **73**, 1149-1151 (1998).

3. Thornton, T. J., Roukes, M. L., Scherer, A. & Vandegaag, B. P. Boundary scattering in quantum wires. *Phys. Rev. Lett.* **63**, 2128-2131 (1989).

4. Roukes, M. L., Scherer, A., Allen, S. J., Craighead, H. G., Ruthen, R. M., Beebe, E. D. & Harbison, J. P. Quenching of the Hall-effect in a one-dimensional wire. *Phys. Rev. Lett.* **59**, 3011-3014 (1987).

5. Tilmans, H. A. C., Elwenspoek, M. & Fluitman, J. H. J. Micro resonant force gauges. *Sens. Actuator A-Phys.* **30**, 35-53 (1992).

6. Carr, D. W., Evoy, S., Sekaric, L., Craighead, H. G. & Parpia, J. M. Measurement of mechanical resonance and losses in nanometer scale silicon wires. *Appl. Phys. Lett.* **75**, 920-922 (1999).

7. Cleland, A. N. & Roukes, M. L. Fabrication of high frequency nanometer scale mechanical resonators from bulk Si crystals. *Appl. Phys. Lett.* **69**, 2653-2655 (1996).

8. Rugar, D. & Grutter, P. Mechanical parametric amplification and thermomechanical noise squeezing. *Phys. Rev. Lett.* **67**, 699-702 (1991).

9. deVries, D. K., Stelmaszyk, P. & Wieck, A. D. Intrinsic and extrinsic capacitances of in-plane-gated transistors. *J. Appl. Phys.* **79**, 8087-8090 (1996).

10. Fricke, K. Piezoelectric properties of GaAs for application in stress transducers. *J. Appl. Phys.* **70**, 914-918 (1991).

Appendix A.4*

Nanowire-Based Very-High-Frequency Electromechanical Resonator

Fabrication and readout of devices with progressively smaller size, ultimately down to the molecular scale, is critical for the development of very-high-frequency nanoelectromechanical systems (NEMS). Nanomaterials, such as carbon nanotubes or nanowires, offer immense prospects as active elements for these applications. We report the fabrication and measurement of a platinum nanowire resonator, 43 nm in diameter and 1.3 μm in length. This device, among the smallest NEMS reported, has a fundamental vibration frequency of 105.3 MHz, with a quality factor of 8500 at 4 K. Its resonant motion is transduced by a technique that is well suited to ultrasmall mechanical structures.

 [DOI: 10.1063/1.1601311]

---

* This section has been published as: A. Husain, J. Hone, Henk W. Ch. Postma, X.M.H. Huang, T. Drake, M. Barbic, A. Scherer & M. L. Roukes, *Appl. Phys. Lett.* **83**, 1240-1242 (2003).

The fabrication and readout of nanometer-scale high frequency resonators has recently been a highly active area of research. Interest in these devices is motivated both by their promise as sensors and actuators, and by fundamental interest in mechanical functionality at the nanoscale. To fabricate these nanoelectromechanical systems (NEMS), researchers typically employ "top-down" techniques, *i.e.,* high-resolution lithography followed by various etching techniques to create freely suspended structures from semiconductor materials such as silicon[1], silicon carbide[2], gallium arsenide[3], and aluminum nitride[4]. Advanced sensing applications require both high responsivity and ultrahigh frequency operation – among the most challenging of these are attainment of sub-attonewton, high frequency force sensing for magnetic resonance force microscopy[5], and the study of mechanical motion in the quantum regime[6]. For future applications such as these, it is desirable to fabricate devices that are as small as possible. Top-down fabrication, however, yields device sizes limited by such factors as the resolution of electron-beam lithography, etch roughness, and the synthesis of epitaxially grown substrates. For this and other reasons, there has been significant recent interest in the integration of nanoscale materials fabricated by a "bottom-up" approach, *e.g.,* carbon nanotubes, semiconductor and metal nanowires. A wide variety of these nano-materials can now be reproducibly produced, with dimensions down to the molecular scale. "Hybrid" (bottom-up + top-down) nanoelectronic devices are now widely realized from these materials by contacting them via lithographic methods; in this work we describe the successful use of this approach to make hybrid nanomechanical devices. To date, difficulties in realizing free suspension of such nanomaterials, compounded with the difficulty of detecting the minute motion of small, high-impedance structures have

impeded development of hybrid NEMS. Here we describe the fabrication and readout of a very-high-frequency (VHF) device consisting of a single platinum nanowire, which is 43 nm in diameter and 1.3 μm in length. We also describe the simple measurement scheme employed as its readout, which is well suited to small, high-impedance NEMS devices in general.

Platinum nanowires were synthesized by electrodeposition of Pt into a commercially available nanoporous polycarbonate membrane (nominal pore diameter 20nm)[7]. The membrane was then dissolved in chloroform, causing the wires to become suspended in solution. This suspension was then allowed to dry, one drop at a time, upon a Si substrate that had been capped by 300-nm-thick layer of thermally grown silicon dioxide and pre-patterned with Au alignment marks. The location of the deposited wires, relative to these alignment marks, was mapped in an optical microscope. (Optical imaging of the small wires is straightforward due to their strong light scattering properties[8,9].) Metallic leads (5 nm Cr, 50 nm Au) to individual nanowires were subsequently patterned by electron beam lithography, evaporation, and lift-off. Finally, the nanowires were suspended above the substrate by etching the SiO_2 in hydrofluoric acid. In this step the electrode pattern also serves as a self-aligned mask, thus forming the anchor point from which the nanowires are suspended. Critical point drying completed the devices; this circumvented damaging effects of meniscus forces.

Fig. A.4.1 shows a scanning electron microscope (SEM) image of the device whose mechanical response is described below. The suspended Pt nanowire has a diameter of 43 nm and a length of 1.3 μm, with an electrical resistance at 4 K of 454 Ω. With a suspended mass of 40 fg and a volume of 1.9 X 10^{-15} cm^3, this device is among

the smallest NEMS structures whose motion has been detected directly. Modeling its response as that of an unstrained doubly clamped beam yields a predicted fundamental mechanical resonance frequency f_0 given by[10]

$$f_0 = \frac{22.4}{2\pi}\frac{R}{2L^2}\sqrt{\frac{Y}{\rho}}\ , \tag{A.4.1}$$

where Y is the Young's modulus, ρ is the density, R is the beam radius, and L is the beam length. Using the measured dimensions and the bulk values for the Young's modulus and density of Pt (168GPa and 21,090 kg/m^3, respectively), Eq. (A.4.1) predicts a fundamental frequency of 64MHz. This is lower than the measured response; possible reasons for this are described below.

Magnetomotive detection, in which an ac current drives a beam in a transverse magnetic field, has been employed to successfully actuate and read out NEMS resonators at frequencies up to and exceeding 1 GHz.[1,11,12] On resonance the device dissipates energy from the current supply as it oscillates in the magnetic field; its behavior can be modeled as a series combination of the normal electrical resistance R_e and a motional impedance $Z_m(f)$ of what appears as an RLC tank circuit[11]. At the resonant frequency f_0, the magnitude of the motional impedance is given by

$$\left|Z_m(f_0)\right| \equiv R_m = \frac{\xi B^2 L^2 Q}{2\pi m f_0}\ , \tag{A.4.2}$$

where Q is the quality factor, m the mass of the device, and ξ a numerical factor that depends on the mode shape (0.83 for the fundamental mode of a doubly clamped beam).

Typical top-down NEMS devices have R_e ~ 10-100 Ω and R_m ~ 1 Ω. In this case, the motional contribution to the overall device impedance at resonance can be relatively

easily detected by measuring the reflected RF power[1]. Smaller-diameter devices, such as the one measured here, will in general have much higher R_m (which can be shown to vary as the cube of the aspect ratio), but will also possess higher R_e. Their compound effect is to make it difficult to match to 50 Ω drive/detection electronics. A reflection measurement will be quite insensitive to the mechanical signal, because nearly all of the power is reflected both on and off resonance. In the case of the present device, for example, the 454 Ω electrical impedance would result in a reflectance of 81.78%; and an additional motional impedance of 10 Ω (calculated from Eq. (A.4.2), assuming a Q of ~3000 and B = 8 Tesla) would change the reflectance by only a small amount, to 82.14%. Clearly, a transmission measurement is more appropriate for high-impedance devices.

We have employed a simple scheme, depicted in Fig. A.4.1, to realize transmission measurements upon the device, which is located in the vacuum space of a magnet cryostat. RF power is applied at the output of a network analyzer (HP 3577A) and fed into the cryostat on coaxial cable to the device. The transmitted signal is carried to a low-noise, room temperature preamplifier providing 62 dB of gain via a second coaxial line. Both the drive and detection lines are terminated with 50 Ω resistors next to the sample. The sample, with its effective impedance $Z_S(f) = R_e + Z_m(f)$, "bridges" these terminated drive and detection lines. For Z_s >> 50 Ω, the termination of the drive and detect lines minimizes standing waves. In this limit, the output voltage at the preamplifier is then given by

$$\frac{V_{out}}{V_{in}} \approx \frac{25\Omega}{Z_s + 25\Omega} \approx \frac{25\Omega}{Z_s} , \qquad \text{(A.4.3)}$$

where the factor of 25 Ω is due to the 50 Ω termination of the detect line in parallel with the 50 Ω input impedance of the preamplifier. The electromechanical impedance $|Z_m(f)|$ can easily be extracted by comparing the output signal to the off-resonance background signal V_b:

$$\frac{|Z_m(f)|}{R_e} \cong -\frac{V_{out} - V_b}{V_b} \quad . \tag{A.4.4}$$

This scheme is of wide applicability to the readout of small-diameter, high-impedance NEMS devices because the output signal is linear in R_m/R_e, and because it provides broadband impedance matching, resulting in a smooth background from which it is easy to pick out a mechanical resonance peak. For extremely large device impedances, however, the cost of the approach is that it can lead to significant attenuation of the signal.

Fig. A.4.2 shows the measured motional impedance of the nanowire device, $|Z_m(f)|$, vs. frequency. The data are obtained at 4 K in magnetic fields from 1-8 Tesla, with a drive signal of 100 μV. $|Z_m(f)|$ shows a peak at 105.3 MHz that increases in height with increasing magnetic field, as is expected for a mechanical resonance. The measured resonance frequency is higher than the predicted frequency of 69 MHz. This is likely due to the differential thermal contraction of the beam and the substrate, which should cause the beam to be under tension. Similar effects have been seen in larger metal resonators. There is no evidence that fabrication of the nanowire by electrodeposition results in a decreased Young's modulus compared to that of bulk Pt.

The resonance curves can be fit to a Lorentzian line shape to extract values of f_0, R_m, and Q. As shown in the left inset to Fig. A.4.2, the measured R_m scales linearly with

the square of the applied magnetic field, consistent with Eq. (A.4.2). The measured quality factor Q of the device, shown in the right inset to Fig. A.4.2, is approximately 8500, and decreases slightly with increasing magnetic field. The attainment of high quality factors is important for technological applications of NEMS devices, but the detailed physics of energy dissipation in these devices is still not well understood. Previous studies have shown that quality factors measured for NEMS generally decrease with increasing surface area-volume ratio, apparently indicating that surface processes contribute strongly to dissipation. Carr *et al.*[13], for example, measure the quality factors of single-crystal silicon beams and find that Q decreases from ~3000 for beams with a surface area-volume ratio of 0.02 nm^{-1} to a value of ~1000 for devices with a ratio of 0.06 nm^{-1}. The nanowire device described here possesses a surface area-volume ratio of 0.095 nm^{-1} and Q of 8500, and thus has surface-related dissipation comparable to or less than that of similar semiconductor structures.

Several important new applications of NEMS resonators require extremely high force sensitivity, which, in turn requires a high compliance, low mass, and large quality factor[14]. The current device is not optimized for compliance, and yields a fairly stiff effective spring constant of ~2.5 N/m. Nonetheless, its force sensitivity, if limited only by thermomechanical noise (*i.e.,* neglecting transducer and amplifier noise), is estimated to be ~13 aN/√Hz at 4K. In the future, this can be greatly enhanced by using more compliant nanowires.

Nonlinear phenomena in NEMS are of interest for a variety of applications, including mixing and parametric amplification. As they can limit dynamic range[15], they also constitute an increasingly important consideration in compliant devices with smaller

dimensions, such as the one described here. Fig. A.4.3 shows the EMF generated by the nanowire (deduced from the measured R_e, R_m, and the applied drive voltage) at a series of drive amplitudes from 60 μV to 380 μV, in steps of 40μV. At high oscillation amplitudes, the equation of motion for a doubly clamped beam becomes bistable, which results in discontinuities in the measured response curve. For our device, this behavior is seen at drive voltages of 260 μV and above: the amplitude of oscillation increases as the frequency is swept upward, and then suddenly jumps to a lower value. The inset to Fig. A.4.3 shows the response of the resonator as the frequency is swept both upward and downward, confirming the expected hysteretic nature of the response curve in the nonlinear regime[16].

In the simplest model for the phenomenon, the critical oscillation amplitude x_c above which bistability occurs is dependent only upon the geometry of the beam[17], and is given by

$$x_c = \frac{d\sqrt{2}}{\sqrt{0.528Q(1-\nu^2)}}\ , \tag{A.4.5}$$

where d is the diameter of the beam and ν is the Poisson's ratio of the material. Evaluating Eq. (A.4.5) for the present device gives a critical amplitude of 0.98 nm. As a check of our readout method, we can also compare the critical amplitude deduced from the measured signal at the onset of nonlinearity. This method gives 2.6 nm, which is reasonable since we expect an over-estimation in the second case due to losses in the signal lines. It is interesting and important to note that for even smaller and more compliant resonators, such as those made from carbon nanotubes, the critical amplitude will be in the sub-nm range. Hence we anticipate that detecting the motion of nanowire

and nanotube devices, while remaining within the linear regime, will pose a significant and generic challenge for the field of NEMS.

In conclusion, we have fabricated a NEMS doubly clamped resonator beam from a Pt nanowire. The fundamental mechanical resonance of the nanowire was excited and detected using the magnetomotive technique, modified here to improve its application to high impedance structures. The fundamental frequency attained was 105.3MHz, with a quality factor of 8500. This is large compared to other reported resonators with a comparable surface area to volume ratio. At modest drive voltages, the resonator exhibits nonlinear, hysteretic behavior.

Acknowledgements: *We gratefully acknowledge support from DARPA/MTO and SPAWAR via grant N66001-01-X-6004/02-8914/1000000928 and from the NSF via grant ECS-0089061. H.W.Ch.P. acknowledges support, in part, from the NWO.*

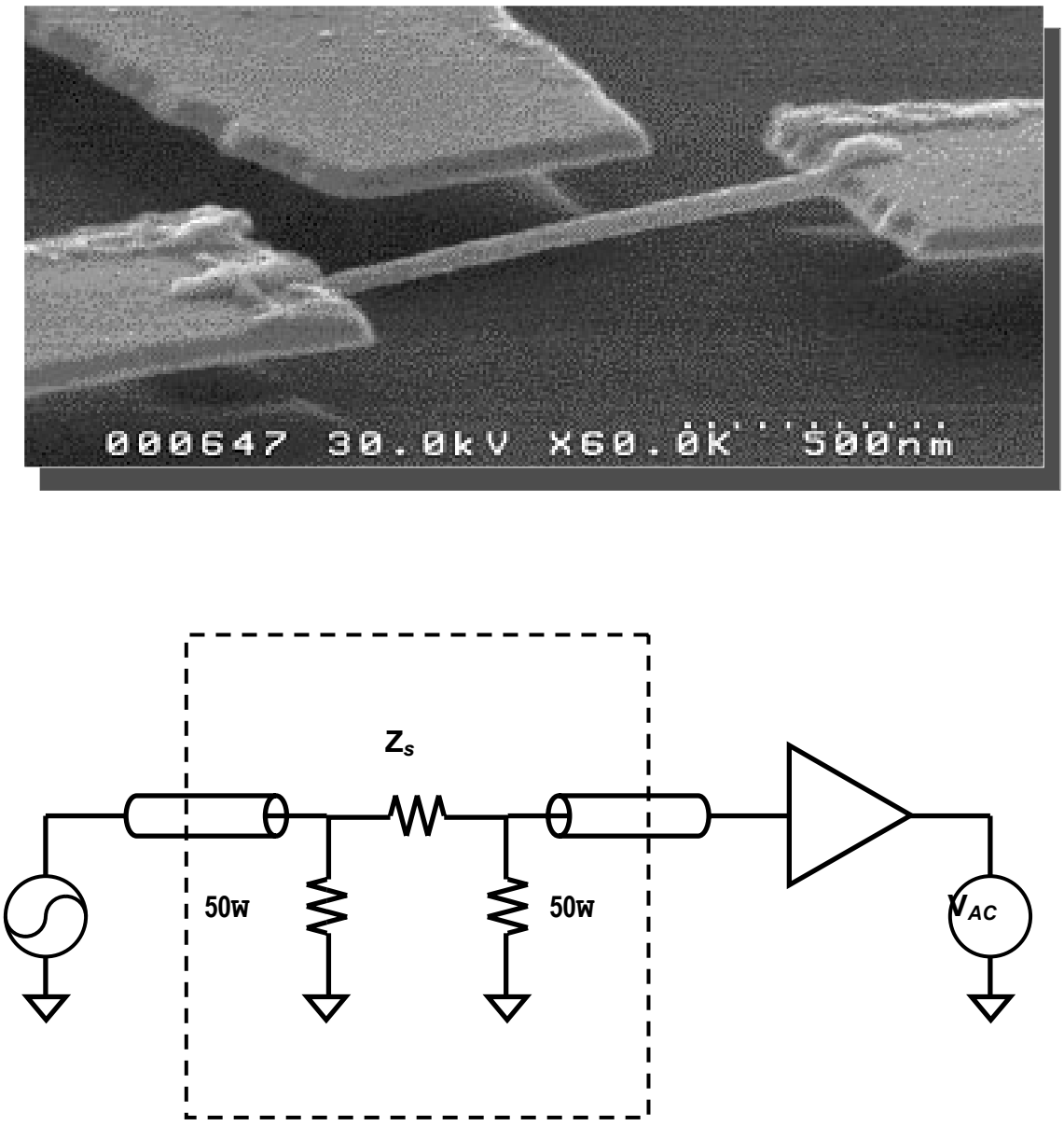

Figure A.4.1 (top) SEM image of the suspended nanowire device, 1.3 μm long and 43 nm in diameter. (bottom) Measurement circuit used for magnetomotive drive and detection.

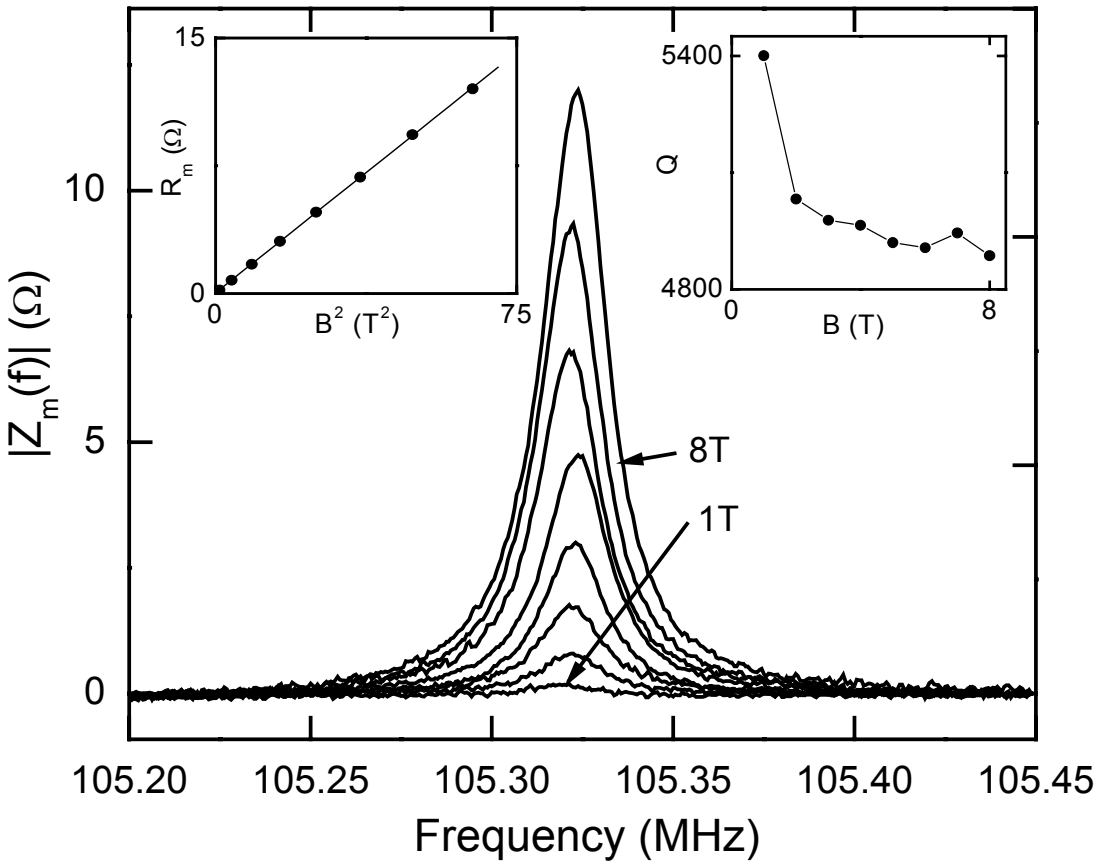

Figure A.4.2 Measured mechanical impedance of the Pt nanowire device as a function of frequency, at a series of magnetic fields from 1 to 8 Tesla. The left inset shows the characteristic B^2 dependence, characteristic of magnetomotive detection. The right inset shows the quality factor Q as a function of magnetic field.

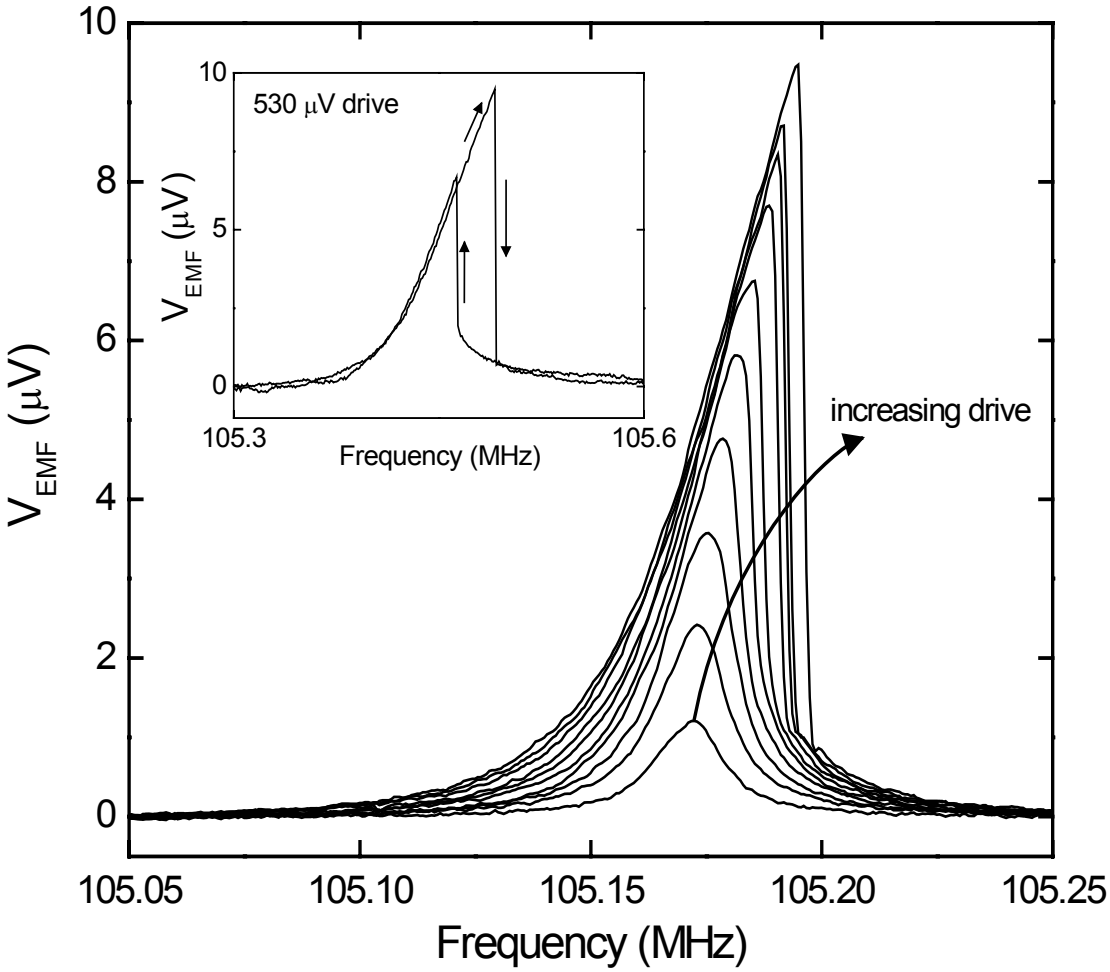

Figure A.4.3 Measured response of the Pt nanowire device, showing the transition to the nonlinear regime as the drive voltage is increased from 40 to 400 μV, in steps of 40 μV. The inset shows the hysteresis visible upon sweeping up and down in frequency (note that the frequency scales are slightly different due to thermal cycling of the device).

References

1. Cleland, A. N. & Roukes, M. L. Fabrication of high frequency nanometer scale mechanical resonators from bulk Si crystals. *Appl. Phys. Lett.* **69**, 2653-2655 (1996).

2. Yang, Y. T., Ekinci, K. L., Huang, X. M. H., Schiavone, L. M., Roukes, M. L., Zorman, C. A. & Mehregany, M. Monocrystalline silicon carbide nanoelectromechanical systems. *Appl. Phys. Lett.* **78**, 162-164 (2001).

3. Harrington, D. A., Mohanty, P. & Roukes, M. L. Energy dissipation in suspended micromechanical resonators at low temperatures. *Physica B* **284**, 2145-2146 (2000).

4. Cleland, A. N., Pophristic, M. & Ferguson, I. Single-crystal aluminum nitride nanomechanical resonators. *Appl. Phys. Lett.* **79**, 2070-2072 (2001).

5. Sidles, J. A., Garbini, J. L., Bruland, K. J., Rugar, D., Zuger, O., Hoen, S. & Yannoni, C. S. Magnetic-resonance force microscopy. *Rev. Mod. Phys.* **67**, 249-265 (1995).

6. Armour, A. D., Blencowe, M. P. & Schwab, K. C. Entanglement and decoherence of a micromechanical resonator via coupling to a Cooper-pair box. *Phys. Rev. Lett.* **88**, 148301 (2002).

7. Martin, C. R. Nanomaterials — a membrane-based synthetic approach. *Science* **266**, 1961-1966 (1994).

8. Barbic, M., Mock, J. J., Smith, D. R. & Schultz, S. Single crystal silver nanowires prepared by the metal amplification method. *J. Appl. Phys.* **91**, 9341-9345 (2002).

9. Mock, J. J., Oldenburg, S. J., Smith, D. R., Schultz, D. A. & Schultz, S. Composite plasmon resonant nanowires. *Nano Lett.* **2**, 465-469 (2002).

10. Timoshenko, S., Young, D. & Weaver, J. W. *Vibration Problems in Engineering* (Wiley, New York, 1974).

11. Cleland, A. N. & Roukes, M. L. External control of dissipation in a nanometer-scale radiofrequency mechanical resonator. *Sens. Actuator A-Phys.* **72**, 256-261 (1999).

12. Huang, X. M. H., Zorman, C. A., Mehregany, M. & Roukes, M. L. Nanodevice motion at microwave frequencies. *Nature* **421**, 496-496 (2003).

13. Carr, D. W., Evoy, S., Sekaric, L., Craighead, H. G. & Parpia, J. M. Measurement of mechanical resonance and losses in nanometer scale silicon wires. *Appl. Phys. Lett.* **75**, 920-922 (1999).

14. Roukes, M. L. Nanoelectromechanical systems face the future. *Phys. World* **14**, 25-31 (2001).

15. Roukes, M. L. Nanoelectromechanical systems. in *Technical Digest, Technical Digest of the 2000 Solid-State Sensor and Actuator Workshop, Hilton Head Island, SC,* ISBN 0-9640024-3-4 (2000).

16. Yurke, B., Greywall, D. S., Pargellis, A. N. & Busch, P. A. Theory of amplifier-noise evasion in an oscillator employing a nonlinear resonator. *Phys. Rev. A* **51**, 4211-4229 (1995).

17. Tilmans, H. A. C. MEMS components for wireless communications. *Sensors and Actuators*, review paper to be published (2003).

Appendix A.5*

Ultrasensitive Nanoelectromechanical Mass Detection

We describe the application of nanoelectromechanical systems (NEMS) to ultrasensitive mass detection. In these experiments, a modulated flux of atoms was adsorbed upon the surface of a 32.8 MHz NEMS resonator within an ultrahigh vacuum environment. The mass-induced resonance frequency shifts by these adsorbates were then measured to ascertain a mass sensitivity of 2.5×10^{-18} g. In these initial measurements, this sensitivity is limited by the noise in the NEMS displacement transducer; the ultimate, limits of the technique are set by fundamental phase noise processes. Our results and analysis indicate that mass sensing of individual molecules will be realizable with optimized NEMS devices.

* Manuscript based on this section, by K. L. Ekinci, X. M. H. Huang & M. L. Roukes, has been submitted to *Appl. Phys. Lett.* (2004).

Nanoelectromechanical systems (NEMS) are emerging as strong candidates for a host of important applications in semiconductor-based technology and fundamental science[1]. The minuscule active masses of NEMS, in particular, render them extremely sensitive to added mass — a crucial attribute for a wide range of sensing applications.

Resonant mass sensors with high mass sensitivities have been employed in many diverse fields of science and technology. Among the most sensitive are those based on the acoustic vibratory modes of crystals[2,3], thin films[4] and micron-sized cantilevers[5,6,7,8]. In all of these, the vibratory mass of the resonator, its resonance frequency, and quality factor (Q) are central in establishing its mass sensitivity. In this Letter, we demonstrate attogram-scale inertial mass sensing using high-frequency NEMS, and discuss how even greater sensitivity will be obtainable with such devices. This provides a concrete initial demonstration of the potential that nanoscale mechanical devices offer for sensing and ultimately weighing individual molecules.

These initial experiments were carried out in an ultrahigh vacuum (UHV) environment within the apparatus depicted in Fig. A.5.1a. This system allows the operation of a NEMS resonator (transduced magnetomotively[9]) while a pulsed, weak flux of Au atoms is directed upon it. The Au atoms are generated by a thermal evaporation source and travel ballistically towards the NEMS within the apparatus. The mass flux, F, of the evaporator is measured by a calibrated quartz crystal monitor and modulated by a shutter; both are in the vicinity of the evaporator. The resonator temperature is regulated at $T \approx 17$ K, both to ensure unity adsorbate sticking probability[10] and to allow careful monitoring of the resonator temperature fluctuations (see Fig. A.5.3). Then, with knowledge of the exposed NEMS surface area, S, (determined from careful scanning

electron microscopy measurements) we can determine the *exact mass*[11] of the adsorbed Au atoms on the NEMS as $\Delta m(t) \approx \int_0^t SF(r_{QCM} / r_{NEMS})^2 \, dt$. In this system, the geometric factor, $(r_{QCM} / r_{NEMS})^2 \approx 5 \times 10^{-3}$.

We employed nanomechanical doubly clamped SiC beam resonators such as the ones shown in Fig. A.5.1b as the sensor elements in these experiments. The beams are embedded within a radio frequency (RF) bridge configuration, creating a unique two-port device[12]. The fundamental in-plane flexural resonance frequency of one of the resonators in the bridge was tracked continuously by the phase-locked loop (PLL) circuit shown schematically in Fig. A.5.1c. The single suspended beam structure of Fig. A.5.1b, labeled T on the right, enables four-wire resistance measurements, which provide extremely sensitive monitoring of the local temperature of the suspended devices (cf. Fig. A.5.3).

In Fig. A.5.2, we display the temporal evolution of the fundamental-mode resonant frequency of the doubly clamped beam resonator, as it is exposed to a ballistic flux of Au atoms. Adsorption commences when the shutter (*see* Fig. A.5.1a) is opened during specific time intervals — changing the effective resonator mass, M_{eff}. The mass responsivity, $\Re = \partial\omega_0 / \partial M_{eff}$ was deduced to be $\Re / 2\pi \approx 2.56 \times 10^{18}$ Hz/g from a linear fit to the data points in the steps of the upper and lower plots, *i.e.* $\Delta\omega_0(t) / 2\pi$ vs. $\Delta m(t)$. The noise floor of the measurement was determined from the regions of constant frequency when the shutter was closed. For this experiment, a measurement bandwidth of Δf=3 kHz (τ~2ms) yielded a frequency noise floor, $\delta\omega_0 / 2\pi \approx 6.51$ Hz — corresponding to a minimum detectable mass, $\delta M = \Re^{-1}\delta\omega_0 \approx 2.5 \times 10^{-18}$ g (ref.13). In units of the atomic mass of Au, m_{Au}, $\delta M \approx 7400 m_{Au}$.

We have taken special precautions in these measurements to minimize the thermal frequency fluctuations and drifts, given that the NEMS resonator will be exposed to both hot incoming atoms and blackbody radiation from the thermal source. This is of special concern here since the thermal resistance — and hence the thermalization rate — between a suspended NEMS device and its environment can be exceptionally large[14]. In Fig. A.5.3, we show four-probe electrical measurements of the resistance fluctuations, $\delta R/R$, of a metallized suspended SiC beam identical in size to NEMS mass sensors (see Fig. A.5.1b). In this measurement, baseline $\delta R/R$ was established when the shutter was in the closed position, *i.e.,* for $t < 50$ s. The device was exposed to Au atom fluxes comparable to those employed in the mass sensitivity experiments, when the shutter was opened at $t \geq 50$ s. $\delta R/R$ of the metal electrode is converted to temperature fluctuations using measured temperature dependence of the four-terminal resistance. $\partial R / \partial T \approx 0.05$ Ω/K in the vicinity of $T \approx 17$ K (Fig. A.5.3 left inset)[15]. Separate measurements of the temperature dependence of the resonance frequency near $T \approx 17$ K yielded $\frac{1}{2\pi}\frac{\partial \omega_0}{\partial T} \approx -700$ Hz/K (Fig. A.5.3 right inset). One can then estimate the thermally induced frequency fluctuations as $\frac{\delta \omega_0}{2\pi} = \frac{1}{2\pi}\frac{\partial \omega_0}{\partial T}\left[\frac{\partial R}{\partial T}\right]^{-1} \delta R \leq 5$ Hz. The frequency fluctuations thus deduced are comparable to our noise floor for zero flux — establishing that no significant thermal effects are observable for the very low fluxes employed in these experiments.

We now turn to a noise analysis of our measurements. In general, resonant mass sensing is performed by carefully determining the resonance frequency of the resonator and then, by looking for a frequency shift in the *steady state* due to the added mass.

Hence, to determine the *mass sensitivity*, δM , one needs to consider the noise floor for frequency measurements, $\delta\omega_0$, since

$$\delta M \approx \left|\frac{\partial M_{eff}}{\partial \omega_0}\right| \delta\omega_0 = \left|\Re\right|^{-1} \delta\omega_0 \ . \qquad \text{(A.5.1)}$$

For the fundamental mode doubly clamped beam sensors, the effective mass is a fraction of the total resonator mass, $M_{eff} = 0.735 M_{tot} = 0.735\rho Ltw$. Here, $L \times t \times w$ are the beam's dimensions, *a*nd ρ its mass density. In the limit $\delta M << M_{eff}$, the resonator's characteristics — in particular, its compliance and Q — will be relatively unaffected by mass accretion. In this regime, $\left|\Re\right| = \omega_0 / 2M_{eff}$, and $\delta M \approx 2\left(M_{eff} / \omega_0\right)\delta\omega_0$. An estimate for $\delta\omega_0$ can be obtained by integrating the spectral density of the frequency fluctuations, $S_\omega(\omega)$, over the effective measurement bandwidth[16] Δf:

$$\delta\omega_0 \approx [\int_{\omega_0 - \pi\Delta f}^{\omega_0 + \pi\Delta f} S_\omega(\omega) d\omega]^{1/2} \ . \qquad \text{(A.5.2)}$$

Elsewhere[17] we have carefully analyzed the fundamental physical limits to inertial mass sensing imposed by the frequency-fluctuation noise $\delta\omega_0$. This analysis leads to the conclusion that in these initial experiments, $\delta\omega_0$ and hence, δM are both limited by the measurement electronics, *i.e.* the transducer, and readout circuitry. In other words, the spectral density of the voltage noise, $S_V(\omega)$, at the output will determine the measured frequency noise as $S_\omega(\omega) = S_V(\omega) / \left(\partial V / \partial\omega\right)^2$ (ref.18). Here, $\partial V / \partial\omega$ is the rate of change of the transducer output in the vicinity of the resonance frequency. We can crudely approximate this as $\partial V / \partial\omega \approx V_{\max} / \Delta\omega = QV_{\max} / \omega_0$. Here, $V_{\max}$ is the maximal

response of the transducer (on resonance) and depends upon the drive level. To maximize the signal-to-noise ratio, one applies the largest rms drive level, $\langle x_{\max} \rangle$, consistent with producing predominantly linear response. This, combined with the readout transducer responsivity, $R_T = \partial V / \partial x$ (with units of V/m) leads to the maximal value $(\partial V / \partial \omega)|_{\max} \approx Q R_T \langle x_{\max} \rangle / \omega_0$. Upon expressing $S_\omega(\omega)$ in terms of $S_V(\omega)$, and integrating Eq. (A.5.2), $\delta\omega_0$, limited by the readout process, is

$$\delta\omega_0 \approx \frac{\omega_0}{Q} \frac{(S_V 2\pi\Delta f)^{1/2}}{R_T \langle x_{\max} \rangle} \quad . \tag{A.5.3}$$

We have made a simplifying assumption that $S_V(\omega)$ is independent of ω, *i.e.* white, in the measurement band. Eq. (A.5.3) depends inversely upon the ratio of the transducer's maximum response to its noise floor (at the output), $R_T \langle x_{\max} \rangle / (S_V 2\pi\Delta f)^{1/2}$. Since it is the square of this ratio that defines the (power) dynamic range (DR) of the coupled mechanical resonator/transducer system, we can write $\delta\omega_0 \approx (\omega_0 / Q) 10^{-(DR/20)}$, yielding the simple and compelling expression

$$\delta M \approx 2(M_{eff} / Q) 10^{-(DR/20)} \quad . \tag{A.5.4}$$

Eq. (A.5.4) allows estimation of the mass sensitivity attainable with our 32.8 MHz device with the following (separately-measured) experimental parameters: $Q \approx 3000$, $DR \approx 60$ dB for a $\Delta f \approx 3$ kHz bandwidth, and $M_{tot} \approx 9.9 \times 10^{-12}$ g. This leads to the approximate result that $\delta M \sim 10^{-18}$ g, quite close to what we experimentally attain. Table A.5.1 summarizes mass responsivity measurements obtained from experiments employing other NEMS devices. The small inconsistencies between the predicted and

experimentally-measured inverse responsivities reflect the extreme mass sensitivity of NEMS. The presence of surface adsorbates at sub-monolayer coverage is enough to change perceptibly the experimental device parameters.

Projections based on Eq. (A.5.4), and its confirmation as provided in our experiments, make clear that NEMS mass sensing can provide significant advances in chemical and biological sensing and mass spectrometry. With the attainment of NEMS operating at microwave frequencies[19] prospects for detection of individual, electrically-neutral macromolecules with single-Dalton sensitivity become feasible. This is a regime where the distinction between conventional resonant inertial mass sensing and mass spectrometry becomes blurred.

In summary, we have demonstrated the unprecedented mass sensitivity of NEMS at the attogram scale in this work. The mass sensitivity of these first generation NEMS are dominated by the noise in the transducer circuitry, but the approach clearly offers near-term prospects for mass sensing of individual molecules.

Acknowledgements: *The authors gratefully acknowledge support for this work from DARPA MTO/MEMS under Caltech grant DABT63-98-1-0012.*

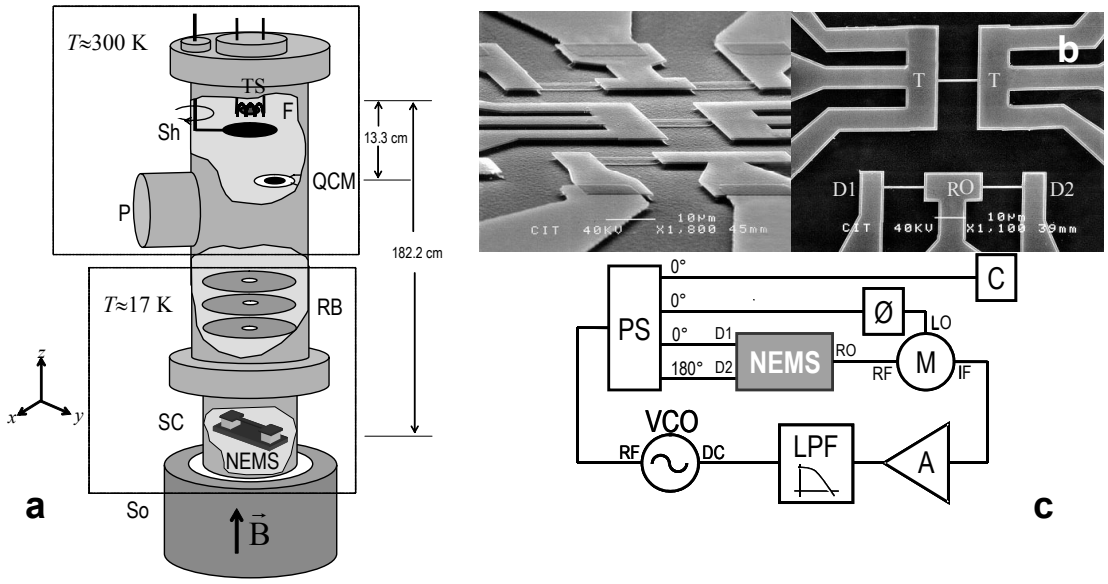

Figure A.5.1 System for nanomechanical mass sensing. **a,** Variable temperature, UHV microwave cryostat for mass sensitivity measurements. The sample chamber (**SC**) is inserted into the bore of a 6T superconducting solenoid (**So**) in liquid helium. The radiation baffles (**RB**) establish a line of sight along the *z*-axis from a room temperature thermal-evaporation source (**TS**) to the bottom of the cryostat. The NEMS resonators are carefully placed in this line-of-sight, some r_{NEMS}=182.2 cm away from the thermal-evaporation source. A calibrated quartz crystal monitor (**QCM**) at a distance of r_{QCM}=13.3 cm and a room temperature shutter (**Sh**) are employed to determine and modulate the atom flux, respectively. **b,** Scanning electron micrographs of nanomechanical doubly clamped beam sensor elements. The beams are made out of SiC with top surface metallization layers of 80 nm of Al. The beams are configured in a radio frequency (RF) bridge with corresponding actuation (D1 and D2) and detection (R) ports as shown. The central suspended structure attached to 3 contact pads on each side, labeled T, is for monitoring the local temperature. **c,** Conceptual diagram of the phase-locked loop (PLL) NEMS readout. The principal components are: voltage controlled radio frequency (RF) oscillator (**VCO**); 4-port power splitter (**PS**) (with three 0° and one 180° output ports); **NEMS** mass sensor with RF bridge readout; mixer (**M**); phase shifter (**Ø**); variable gain amplifier (**A**); low pass filter (**LPF**); frequency counter (**C**).

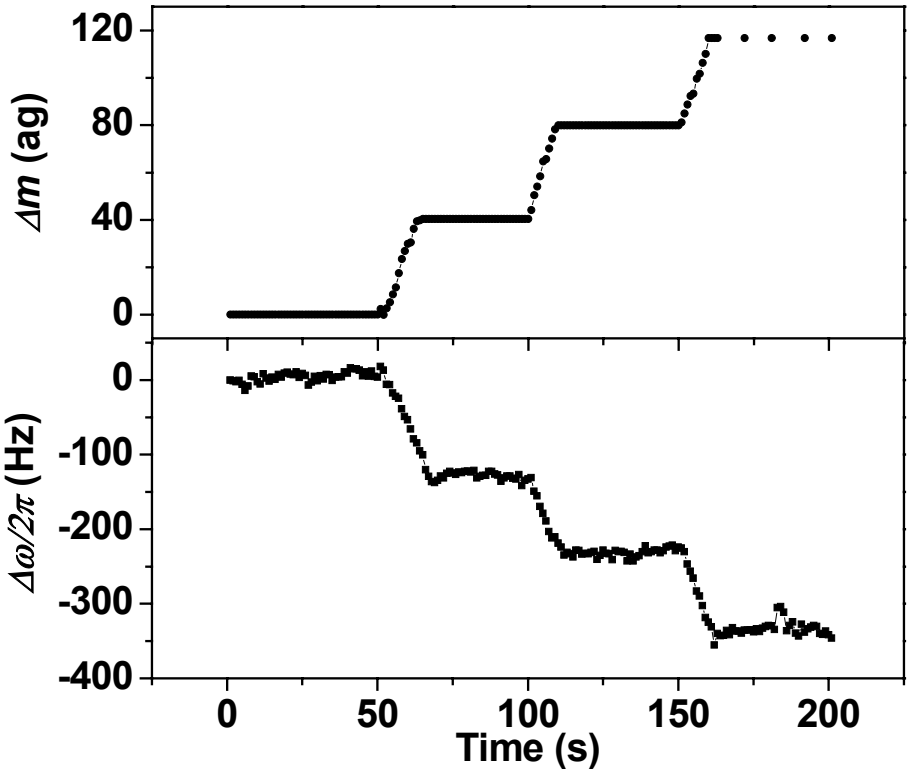

Figure A.5.2 Frequency shifts, $\Delta\omega/2\pi$, (bottom) induced by sequential 40 attogram (ag) (1 ag=10^{-18} g) gold atom adsorption upon a 14.2 μm × 670 nm × 259 nm silicon carbide doubly-clamped beam resonator. The (initial) fundamental frequency is $\omega_0/2\pi \approx 32.8$ MHz. The accreted mass of gold atoms, Δm, in the upper plot is measured by a separate quartz crystal detector. The rms frequency fluctuations of the system (*i.e.* the noise level in the lower trace) correspond to a mass sensitivity of 2.5 ag for the 2 ms averaging time employed.

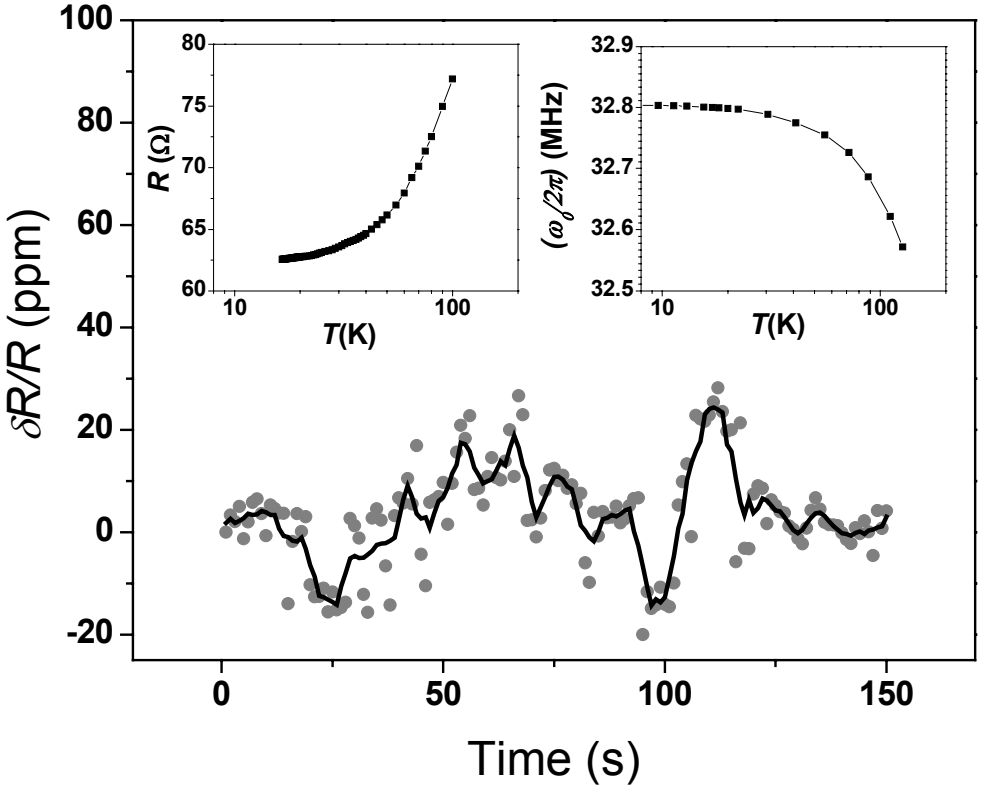

Figure A.5.3 The four-terminal resistance fluctuations, $\delta R/R$, of the metal electrode on a suspended SiC beam. $R \approx 62.5\ \Omega$ at $T \approx 17$ K. $\delta R/R$ is converted to local temperature fluctuations using measured values of temperature dependence of the electrode resistance (left inset). The local temperature fluctuations are then converted to thermally-induced frequency fluctuations using the temperature dependence of the resonator frequency (right inset). Here, $\omega_0 / 2\pi \approx 32.8$ MHz at $T \approx 17$ K.

$\omega_0/2\pi$ (MHz)	$L \times w \times t$ (μm)	M_{tot} (g)	$\left[\lvert\Re\rvert/(2\pi)\right]_{calc}$ (Hz/ag)	$\left[\lvert\Re\rvert/(2\pi)\right]_{expt}$ (Hz/ag)
11.4	26.2×0.8×0.26	36×10^{-12}	0.22	0.50
32.8	14×0.67×0.26	9.9×10^{-12}	2.2	2.6
56	12×0.65×0.26	7.1×10^{-12}	5.2	5.1
72	100×65×0.26	6.0×10^{-12}	8.2	12

Table A.5.1. Calculated and experimental values of the mass responsivity in doubly clamped beam resonators.

References

1. Roukes, M. L. Nanoelectromechanical systems face the future. *Phys. World* **14**, 25-31 (2001).

2. Lu, C. *Applications of Piezoelectric Quartz Crystal Microbalances* (Elsevier, London, 1984).

3. Narine, S. S. & Slavin, A. J. Use of the quartz crystal microbalance to measure the mass of submonolayer deposits: Measuring the stoichiometry of surface oxides. *Journal of Vacuum Science & Technology* **A 16**, 1857-1862 (1998).

4. Thompson, M. and Stone, D. C. *Surface-Launched Acoustic Wave Sensors: Chemical Sensing and Thin-Film Characterization* (John Wiley and Sons, New York, 1997).

5. Thundat, T., Wachter, E. A., Sharp, S. L. & Warmack, R. J. Detection of mercury-vapor using resonating microcantilevers. *Appl. Phys. Lett.* **66**, 1695-1697 (1995).

6. Ilic, B. et al. Mechanical resonant immunospecific biological detector. *Appl. Phys. Lett.* **77**, 450-452 (2000).

7. Ono, T., Li, X. X., Miyashita, H. & Esashi, M. Mass sensing of adsorbed molecules in sub-picogram sample with ultrathin silicon resonator. *Rev. Sci. Instrum.* **74**, 1240-1243 (2003).

8. Lavrik, N. V. & Datskos, P. G. Femtogram mass detection using photothermally actuated nanomechanical resonators. *Appl. Phys. Lett.* **82**, 2697-2699 (2003).

9. Cleland, A. N. & Roukes, M. L. Fabrication of high frequency nanometer scale mechanical resonators from bulk Si crystals. *Appl. Phys. Lett.* **69**, 2653-2655 (1996).

10. Ekinci, K. L. & Valles, J. M. Thickness dependence of the morphology of ultrathin quench condensed gold films. *Phys. Rev. B* **58**, 7347-7350 (1998).

11. We assume uniform coverage of the Au atoms. Hence, we are measuring the change in the effective resonator mass, M_{eff}. For the doubly clamped beam geometry employed, $M_{eff} = 0.735 M_{tot}$, where M_{tot} is the total resonator mass (*see* later discussion in text).

12. Ekinci, K. L., Yang, Y. T., Huang, X. M. H. & Roukes, M. L. Balanced electronic detection of displacement in nanoelectromechanical systems. *Appl. Phys. Lett.* **81**, 2253-2255 (2002).

13. Following standard practice, the mass noise floor is defined as the added mass that will generate a frequency shift resolvable above the frequency noise floor, *i.e.* with signal-to-noise ratio~1.

14. Tighe, T. S., Worlock, J. M. & Roukes, M. L. Direct thermal conductance measurements on suspended monocrystalline nanostructures. *Appl. Phys. Lett.* **70**, 2687-2689 (1997).

15. The thermalization rate between the electrons and the phonons is very short compared to any of the time scales in our experiments.

16. Robins, W.P. *Phase Noise in Signal Sources* (Peter Pelegrinus Ltd., London, 1982).

17. Ekinci, K. L., Yang, Y. T. & Roukes, M. L. Ultimate limits to inertial mass sensing based upon nanoelectromechanical systems. *J. Appl. Phys.* (in press); also available at *http://www.arxiv.org/abs/physics/0309075*

18. There is no loss of generality in this approach. Following standard analysis, the electrical noise from the transducers and subsequent stages in the readout chain can be subsumed into an "effective" voltage noise at the transducer. The VCO separately contributes to the observed frequency noise, but its measured phase noise is negligible in this work.

19. Huang, X. M. H., Zorman, C. A., Mehregany, M. & Roukes, M. L. Nanodevice motion at microwave frequencies. *Nature* **421**, 496 (2003).

APPENDIX B

NEWS COVERAGE RELATED TO THIS WORK

Caltech Press Release:

Nanodevice Breaks 1-GHz Barrier

Contact: Robert Tindol, Caltech Media Relations, (626) 395-3631

Wednesday, January 29, 2003

PASADENA, Calif.- Nanoscientists have achieved a milestone in their burgeoning field by creating a device that vibrates a billion times per second, or at one gigahertz (1 GHz). The accomplishment further increases the likelihood that tiny mechanical devices working at the quantum level can someday supplement electronic devices for new products.

Reporting in the January 30 issue of the journal *Nature,* California Institute of Technology professor of physics, applied physics, and bioengineering Michael Roukes and his colleagues from Caltech and Case Western Reserve University demonstrate that the tiny mechanism operates at microwave frequencies. The device is a prototype and not yet developed to the point that it is ready to be integrated into a commercial application; nevertheless, it demonstrates the progress being made in the quest to turn nanotechnology into a reality-that is, to make useful devices whose dimensions are less than a millionth of a meter.

This latest effort in the field of NEMS, which is an acronym for "nanoelectromechanical systems," is part of a larger, emerging effort to produce mechanical devices for sensitive force detection and high-

frequency signal processing. According to Roukes, the technology could also have implications for new and improved biological imaging and, ultimately, for observing individual molecules through an improved approach to magnetic resonance spectroscopy, as well as for a new form of mass spectrometry that may permit single molecules to be "fingerprinted" by their mass.

"When we think of microelectronics today, we think about moving charges around on chips," says Roukes. "We can do this at high rates of speed, but in this electronic age our mind-set has been somewhat tyrannized in that we typically think of electronic devices as involving only the movement of charge.

"But since 1992, we've been trying to push mechanical devices to ever-smaller dimensions, because as you make things smaller, there's less inertia in getting them to move. So the time scales for inducing mechanical response go way down."

Though a good home computer these days can have a speed of one gigahertz or more, the quest to construct a mechanical device that can operate at such speeds has required multiple breakthroughs in manufacturing technology. In the case of the Roukes group's new demonstration, the use of silicon carbide epilayers to control layer thickness to atomic dimensions and a balanced high-frequency technique for sensing motion that effectively transfers signals to macroscale circuitry have been crucial to success. Both advances were pioneered in the Roukes lab.

Grown on silicon wafers, the films used in the work are prepared in such a way that the end-products are two nearly identical beams 1.1 microns long, 120 nanometers wide and 75 nanometers thick. When

driven by a microwave-frequency electric current while exposed to a strong magnetic field, the beams mechanically vibrate at slightly more than one gigahertz.

Future work will include improving the nanodevices to better link their mechanical function to real-world applications, Roukes says. The issue of communicating information, or measurements, from the nanoworld to the everyday world we live in is by no means a trivial matter. As devices become smaller, it becomes increasingly difficult to recognize the very small displacements that occur at much shorter time-scales.

Progress with the nanoelectromechanical system working at microwave frequencies offer the potential for improving magnetic resonance imaging to the extent that individual macromolecules could be imaged. This would be especially important in furthering the understanding of the relationship between, for example, the structure and function of proteins. Also, the devices could be used in a novel form of mass spectrometry, and for sensing individual biomolecules in fluids, and perhaps for realizing solid-state manifestations of the quantum bit that could be exploited for future devices such as quantum computers.

The coauthors of the paper are Xue-Ming (Henry) Huang, a graduate student in physics at Caltech; and Chris Zorman and Mehran Mehrengany, both engineering professors at Case Western Reserve University.

APPENDIX C

MAJOR EQUIPMENT

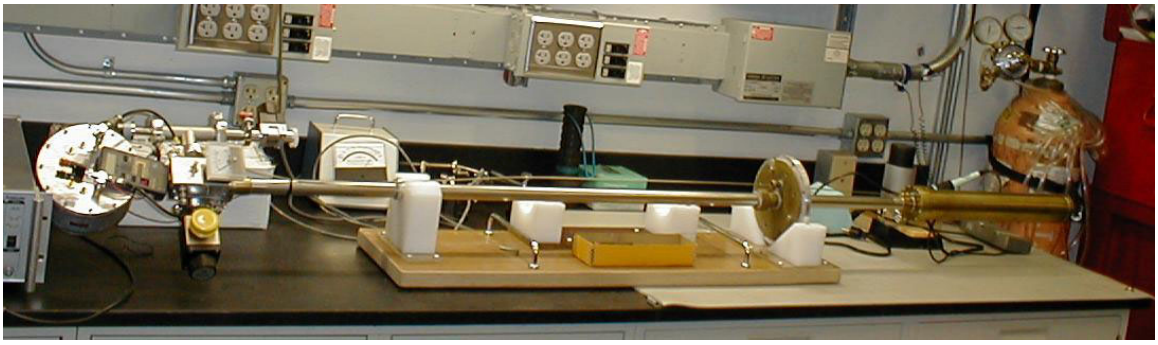

High Frequency Dipper

UT-85 stainless steel coax cable runs from room temperature stage to the cryogenic stage, to provide electrical connections for device testing. A commercial MITEQ AFS series cryogenic amplifier is mounted inside the dipper. The amplifier has a bandwidth of 0.1~2 GHz, and is thermally clamped to 4.2 K.

Sample is mounted on a homemade sample holder with three SMA microstrip launchers. Microstrip lines on microwave circuit board connects the launcher and the sample. On the sample side, a small section (~ 1 mm long) of wire-bonding wire connects the finger pads on samples to the microstrip lines.

The dipper is equipped with sample stage heater and thermometer, and is capable of heating up the sample stage to room temperature when the dipper can is immersed in liquid-helium bath.

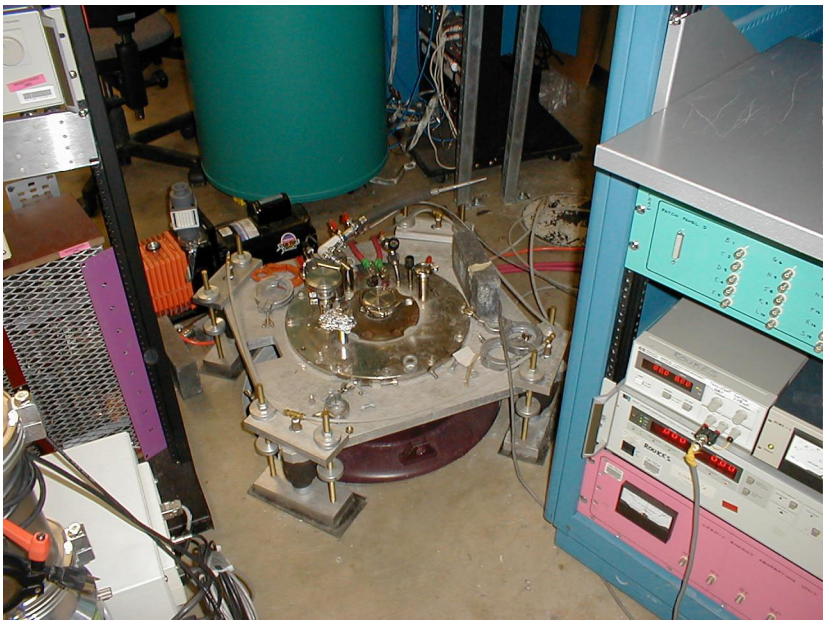

Cryostat with Superconducting Magnet Inside.

The magnet can provide **B** field up to 9T.

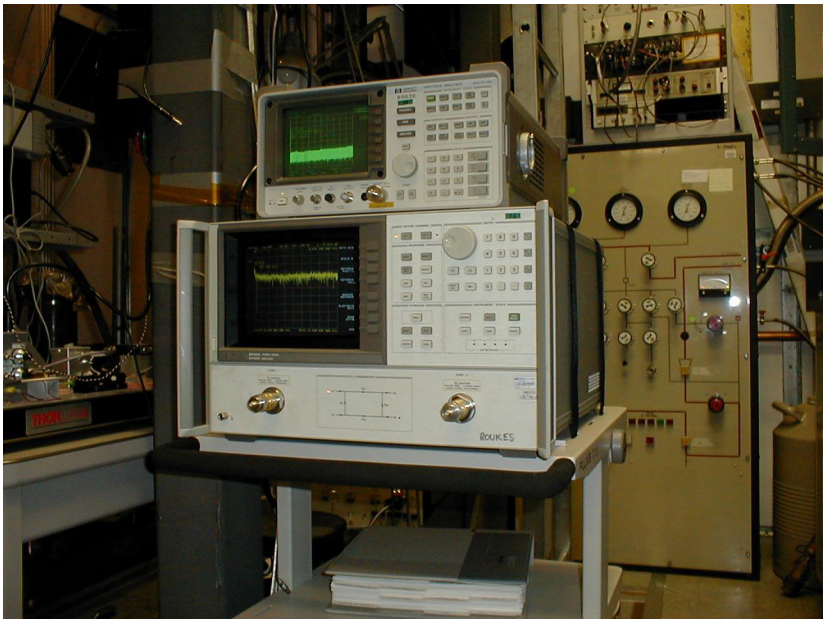

Test Equipments

Showing a microwave spectrum analyzer (HP8563B)

and a microwave network analyzer (HP8720C).

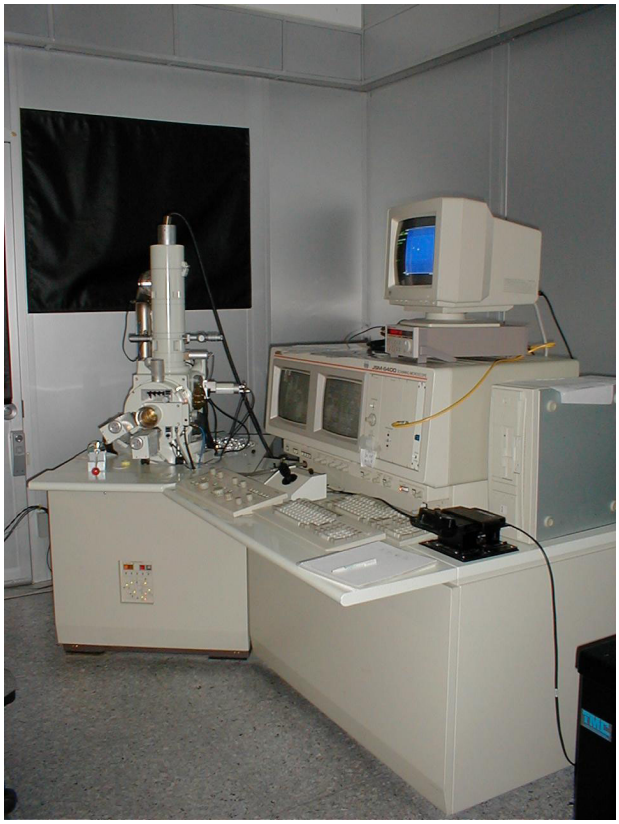

Scanning Electron Microscope (SEM)
JEOL 6400 SEM.

Electron Cyclotron Resonance (ECR) Etching Machine.

PUBLICATION LIST

JOURNAL PUBLICATIONS

1. Huang, X. M. H., Zorman, C. A., Mehregany, M. & Roukes, M. L. Nanodevice motion at microwave frequencies. *Nature* **421,** 496 (2003).

2. Husain, A., Hone, J., Postma, H. W. Ch., Huang, X. M. H., Drake, T., Barbic, M., Scherer, A. & Roukes, M. L. Nanowire-based very-high-frequency electromechanical resonator, *Appl. Phys. Lett.* **83**, 1240-1242 (2003).

3. Tang, H. X., Huang, X. M. H., Roukes, M. L., Bichler M. & Wegscheider, W. Two-dimensional electron-gas actuation and transduction for GaAs nanoelectromechanical systems. *Appl. Phys. Lett.* **81**, 3879-3881 (2002).

4. Ekinci, K. L., Yang, Y. T., Huang, X. M. H. & Roukes, M. L. Balanced electronic detection of displacement in nanoelectromechanical systems. *Appl. Phys. Lett.* **81**, 2253-2255 (2002).

5. Yang, Y. T., Ekinci, K. L., Huang, X. M. H., Schiavone, L. M., Roukes, M. L., Zorman, C. A. & Mehregany, M. Monocrystalline silicon carbide nanoelectromechanical systems. *Appl. Phys. Lett.* **78**, 162-164 (2001).

CONFERENCE PAPERS

1. Huang, X. M. H., Prakash, M. K., Zorman, C. A., Mehregany, M. & Roukes, M. L. Free-free beam silicon carbide nanomechanical resonators. in *Digest of Technical Papers, volume 1, Transducers'03, the 12th International Conference on Solid-State Sensors, Actuators and Microsystems,Boston, MA, USA, June 8-12, 2003,* (ISBN: 0-7803-7732-X), 342-343 (2003).

2. Huang, X. M. H., Zorman, C. A., Mehregany, M. & Roukes, M. L. Quality factor issues in silicon carbide nanomechanical resonators. in *Transducers'03, the 12th International Conference on Solid-State Sensors, Actuators and Microsystems, Boston, MA, USA, June 8-12, 2003,* (ISBN: 0-7803-7732-X), 722-725 (2003).

3. Huang, X. M. H., Ekinci, K. L., Yang, Y. T., Zorman, C. A., Mehregany M. & Roukes, M. L. Nanoelectromechanical silicon carbide resonators for ultra high frequency applications. *In Technical Digest, Solid-State Sensor, Actuator, and Microsystems Workshop 2002, Hilton Head, SC,* (ISBN: 0-9640024-4-2), 368-369 (2002).

SUBMITTED PAPERS

1. Ekinci, K. L., Huang, X. M. H. & Roukes, M. L. Ultrasensitive nanoelectromechanical mass detection. submitted to *Appl. Phys. Lett.* (2004).

MANUSCRIPTS IN PREPARATION

1. Huang, X. M. H., Prakash, M. K., Yurke B. & Roukes, M. L. Quantum jumps in nanomechanics: issues of principle and prototype devices. to be submitted (2004).

2. Huang, X. M. H., Hone J. & Roukes, M. L. Design of a nanotube-based megnetomechanical resonator for zeptonewton force detection. to be submitted (2004).

3. Huang, X. M. H., Schwab, K., Prakash, M. K., Hone, J., Postma, H. W. Ch., Zorman, C. A., Mehregany, M. & Roukes, M. L. Potentialities and limitations of magnetomotive transduction in studying nanotube mechanical motion. to be submitted (2004).

4. Huang, X. M. H. Feng, X. L., Prakash, M. K., Kumar, S., Zorman, C. A., Mehregany M. & Roukes, M. L. Fabrication of suspended nanostructures from bulk 6H-SiC substrates for nanomechanical resonator applications. to be submitted (2004).

5. Huang, X. M. H., Prakash, M. K., Zorman, C. A., Mehregany, M. & Roukes, M. L. Mechanical resonance measurement and quality factor optimization in silicon carbide nanoelectromechanical systems. to be submitted (2004).